Structural Studies of the Solid-Liquid Interface

Reactions at the Noble Electrode Surface

Jack William Beane

Department of Physics
University of Liverpool

This thesis is submitted in accordance with the requirements of the University of Liverpool for the degree of
Doctor in Philosophy

August 2022

For my Grandparents, Mum and Dad.

Declaration

I, Jack William Beane, declare this thesis is a presentation of my own work except where indicated in the text. It has not been previously submitted, in part or whole, to any university or institution for any degree, diploma, or other qualification.

Jack William Beane
August 2022

Acknowledgements

This research was possible due to the funding of an EPSRC studentship.

I would like to acknowledge a number of people without whom the work in these pages would not exist. Firstly, my primary supervisor Chris is to thank for introducing me to this fascinating field of research and being so willing to share his considerable experience and knowledge of surface x-ray diffraction, electrochemistry and condensed matter physics in general. The experiments in this thesis were initially devised by both Chris and my secondary supervisor Yvonne, whose help in laboratory, experimental hutch, control room and office I am extremely grateful for. As colleagues and advisors would like to sincerely thank Chris and Yvonne for their guidance through every step of my PhD. Thanks as well to my third supervisor David.

Throughout my studies we have been very lucky to be joined in our research group by some brilliant researchers and friends. I've had the pleasure of working alongside Josh, Lisa, Graeme, Len, Angeline and Bruna, who are some of the most intelligent, supportive and kind people I've ever met, and great colleagues. Thanks also to Gary and Liz, who, though our times in the group didn't overlap, still offered me some valuable advice when our paths did cross.

I have to give a special thanks to Josh, who was one of the most important resources for me in terms of carrying out the experiments in the following chapters. I don't know if I would have ever found the Shakesbeer without him! And I cannot thank Lisa enough for getting me through my first couple of years of study, with the help of too many pints, laughs and games of backgammon. Thanks to Angeline for helping me put synchrotron experiments into perspective when everything felt like it was going wrong. And an extra obrigado to Bruna, who helped me to still feel a part of the group while writing up from the other side of the Mersey during a global pandemic. Over the course of my PhD, synchrotron experiments were conducted as part of a team with Chris, Yvonne, Josh, Lisa, Angeline and Bruna, and the results in this thesis would not have been possible without the six of them.

I've worked with some excellent collaborators throughout my studies and I would like to thank Para, Francesco, Natasa, Sarah, Alicja and Adam for their help and hard work, as well

as great company, on beamtime. The experiments I've worked on were only possible thanks to the dedication and support received on beamtime from Francesco Carla, Paul Thompson, Oier Bikondoa, Dan Porter, Gareth Nisbet, Philip Mousley, Jonathan Rawle and all the other staff at XMaS, I07, I16 and ID03.

I have to also thank everyone in the SIRE for making me feel a part of a community during my PhD and helping make these years so enjoyable. There are too many to thank for the great memories of SIRE Christmas parties, Vivas and weekly trips to the AJ. Playing five-a-side on Wednesdays with SIRE FC and running Dockside and parkrun with Jack and Leanne gave me things to look forward to every week and helped me reach a peak fitness that I can only dream of reaching again post-writing up. I have to give a special mention to The Toms (Shalvey, Baines, Feathers), Olivia, Huw and Nicole who are all great scientists but more importantly, made coming into the office every day fun.

Away from Uni and research, I have to thank my great group of mates from back home who always give me a laugh and a distraction when I need it most. Thanks to Amber and Sandy for always being so encouraging and helping to make Chester home over the last few years. I want to acknowledge how lucky I am to have the most amazing family that believe in me and have always supported me unconditionally. Thanks to my grandparents, Mum, Dad and Frankie for always being there for me. Finally, there is no chance that I would have got this done without Drew. She has put up with a lot over the last few years, supporting me and giving me the confidence to, when it felt like an insurmountable task, write this thesis and to make it the best it could be.

Abstract

Structural Studies of the Solid-Liquid Interface: Reactions at the Noble Electrode Surface
by Jack William Beane,
March 2022

Surface x-ray diffraction (SXRD) has been employed in the study of the electrochemical interface for a number of electrode surface structures. The technique is employed *in situ* to obtain detail on the atomic structure of model single crystal electrode surfaces.

The potential dependence of the hexagonal reconstructions of gold surfaces (Au(001) and Au(111)) in hydroxide electrolyte solutions in the presence and absence of CO molecules were investigated by SXRD. Results indicated that the compressibility of the reconstructed surface structures depended on a build up of charge at the surface at negative electrode potentials and that, with CO, the surfaces are locked into highly compressed phases. The influence of cation species on the Au(111) surface reconstruction was also investigated, finding that the cation had an influence on the sensitivity of the surface reconstruction to the applied potential.

Phosphate adsorption on Cu(111) was also investigated *in situ* by SXRD. Results show that a mixed copper-oxygen layer is formed, and the surface exhibits a reversible, potential dependent change in roughening. Experiments also reveal the importance of surface preparation, as different preparation methods are shown to produce very different surface morphologies.

The surface structures formed during halide adsorption and Pb UPD at the Cu(001) surface were investigated by resonant SXRD. Structural characterisations of the adlayer and UPD structures on Cu(001) were carried out, before coupling surface diffraction and spectroscopic measurements to obtain detail on the charge distribution for different atoms in the surface structure. Results show that iodine exhibits similar behaviour to that previously reported for other halide ions, and for the UPD Pb structure formed on Cu(001), a potential dependent change in the charge distribution for atoms at the surface was observed between -0.34 V and -0.22 V.

Table of Contents

List of Figures xv

List of Abbreviations xxi

1 Introduction 1

2 Theoretical Principles 5
2.1 Introduction . . . 5
2.2 Electrochemistry . . . 5
2.2.1 Electrode Reactions . . . 6
2.2.2 The Solid-Liquid Interface . . . 9
2.2.3 Adsorption Phenomena . . . 12
2.2.4 Cyclic Voltammetry . . . 12
2.3 Surface X-Ray Diffraction . . . 15
2.3.1 X-Ray Diffraction . . . 15
2.3.2 Momentum Transfer, q . . . 18
2.3.3 Scattering from a Single Atom . . . 19
2.3.4 Scattering from a Unit Cell . . . 19
2.3.5 Scattering from a Crystal . . . 20
2.3.6 Reciprocal Lattice . . . 21
2.3.7 XRD from a Surface . . . 22
2.4 Crystal Structure of Single Crystal Electrodes . . . 24
2.4.1 The (111) Surface . . . 24
2.4.2 The (001) Surface . . . 27
2.5 Modelling Surface Structure . . . 29
2.5.1 Adlayer Structures . . . 31
2.6 X-ray Voltammetry . . . 34
2.7 Summary . . . 35

3 Experimental Methods 37
3.1 Introduction . . . 37
3.2 Sample Preparation and Characterisation . . . 37
3.2.1 Surface Annealing . . . 38
3.2.2 Electrochemical Etching . . . 38
3.3 Cleaning of Electrochemical Equipment . . . 39
3.4 The Electrochemical Cell . . . 40
3.4.1 Potentiostat . . . 40
3.4.2 The X-Ray Electrochemical Thin Layer Cell . . . 41
3.5 Synchrotron Facilities . . . 44
3.5.1 Synchrotron Radiation . . . 44
3.5.2 Beamline and Diffractometer . . . 46
3.5.3 Sample Alignment . . . 50
3.6 Scans and Data Extraction . . . 51
3.6.1 Rocking Scans . . . 52
3.6.2 Geometric Correction Factors . . . 52
3.6.3 Data Analysis . . . 54
3.7 Summary . . . 54

4 The Hexagonal Reconstruction of Gold 57
4.1 Introduction . . . 57
4.2 Experimental Methods . . . 62
4.3 Results and Discussion . . . 63
4.3.1 Au(001) and Au(111) Reconstruction in 0.1 M KOH . . . 63
4.3.2 The CO Effect . . . 71
4.3.3 The Cation Effect . . . 74
4.4 Conclusions . . . 81

5 Surface Stability of Cu(111) in Phosphate Electrolyte 83
5.1 Introduction . . . 83
5.2 Experimental Methods . . . 84
5.3 Results and Discussion . . . 85
5.3.1 Electrochemical Characterisation . . . 85
5.3.2 Structural Characterisation . . . 87
5.3.3 Discussion . . . 99
5.4 Conclusions . . . 102

6 Halide Ions and Lead at the Cu(001) Surface 105
6.1 Introduction 105
6.1.1 Resonant Surface X-Ray Diffraction 106
6.1.2 Halide Adsorption on Cu(001) 108
6.1.3 Underpotential Deposition of Lead on Cu(001) 109
6.2 Experimental Methods 112
6.3 Results and Discussion 113
6.3.1 Structural Characterisation of Iodine Adsorption on Cu(001) 113
6.3.2 Resonant SXRD Study of Iodine Adsorption on Cu(001) 116
6.3.3 Structural Characterisation of Pb UPD on Cu(001) 119
6.3.4 Resonant SXRD Study of Pb UPD on Cu(001) 128
6.4 Conclusions 129

7 Conclusions and Future Work 131

References 135

Appendix A Publications 149

List of Figures

2.1 (a) Schematic diagram of the Grahame model of the electrochemical double-layer, showing the electrode surface, the inner Helmholtz plane and the outer Helmholtz plane. (b) The corresponding potential drop across the interface for specifically adsorbed anions (green curve) and non-specifically adsorbed anions (black curve) is shown, where z is the distance in the direction normal to the electrode surface. The potentials inside the metal electrode, of the OHP, the IHP and inside the bulk electrolyte solution are represented by ϕ_M, ϕ_{OHP}, ϕ_{IHP} and ϕ_S. 10
2.2 Schematic of a three-electrode cell 13
2.3 Cyclic voltammogram for a reversible reaction 14
2.4 Schematic of the *fcc* crystal structure. 16
2.5 The low index planes in an *fcc* unit cell, with the (a) (001), (b) (110) and (c) (111) planes shown in yellow. 16
2.6 Diagram of Bragg's law 17
2.7 Diagram showing momentum transfer **q** during elastic scattering 18
2.8 Crystal surface schematic diagrams showing three types of surface/interface: (a) an isolated monolayer, (b) a terminated crystal and (c) a crystal-crystal interface. 22
2.9 Schematic diagrams showing the diffraction patterns resulting from three types of surface/interface: (a) a 2D layer, (b) the combination of a bulk crystal and 2D layer and (c) crystal truncation rods from a surface. 23
2.10 Diagrams showing (a) top-down and (b) side-on schematics of the (111) surface and atomic stacking in (c) *fcc* and (d) *hcp* sites. 25
2.11 Reciprocal space map of the (111) surface with directions and Bragg peak positions given in terms of the hexagonal surface unit cell vectors 26
2.12 Diagrams showing (a) top-down and (b) side-on schematics of the (001) surface and (c) ABAB stacking in *fcc* sites. 28

2.13 Schematic diagram showing the reciprocal space map for the (001) surface given in terms of the tetragonal surface unit cell vectors 28
2.14 The effect on the $(1,0,l)$ CTR profile from a Au(001) surface of altering parameters $\varepsilon = 0.06$ (red), $\theta = 0.7$ (grey) and $\sigma = 0.15$ (green) 30
2.15 Effect on the $(0,0,l)$ CTR profile from Au(001) of a commensurate Cu adlayer (green) and Cu bilayer (red). 32

3.1 Flame annealing of a gold single crystal surface with a butane flame 39
3.2 Circuit diagram of a potentiostat 41
3.3 Schematic of the x-ray electrochemical thin layer cell 42
3.4 The x-ray electrochemical cell, mounted on the I16 beamline at Diamond Light Source 43
3.5 Schematic diagram of a 3rd generation synchrotron 45
3.6 The beamline optics at I07, Diamond Light Source 46
3.7 Diagrams of a (2+2)-circle diffractometer in (a) vertical and (b) horizontal geometry operating modes. 48
3.8 The diffractometer housed in EH1 at I07, Diamond Light Source 48
3.9 The experimental setup on the I16 beamline, Diamond Light Source. 49
3.10 The experimental setup on the XMaS beamline, BM28 at the ESRF. 50

4.1 Schematics showing (a) the hexagonal reconstruction exhibited by the Au(111) surface with $(23 \times \sqrt{3})$ periodicity and (b) the ”5×20” or "hex" reconstruction exhibited by the Au(001) surface. 58
4.2 The in-plane diffraction pattern arising due to the $(\mathrm{p} \times \sqrt{3})$ reconstructed Au(111) surface. 59
4.3 The in-plane diffraction pattern arising due to the hexagonal reconstructed Au(001) surface. 60
4.4 Cyclic voltammetry for the (a) Au(111) and (b) Au(001) surfaces in 0.1 M NaOH alkaline electrolyte reproduced from a study by Rodriguez *et al.* . . 61
4.5 Fitted curves to the scattered x-ray intensity scanned along the $[110]_{cubic}$ direction measured through the reconstruction peak shown at approximately $(1.2, 1.2, 0.4)_{cubic}$, measured for the reconstructed Au(001) surface in 0.1 M KOH. 64
4.6 Fitted curves to the scattered x-ray intensity measured for the reconstructed Au(111) surface in 0.1 M KOH, measured along the [1 1 0] direction. 65

4.7 (a) Integrated intensity of the reconstruction peak (black points) and $(1,1,0.4)$ CTR peak (red points) as a function of electrode potential. (b) Potential dependence of the in-plane near neighbour spacing (lattice constant, a_{NN}) calculated for Au atoms in the Au(001) "hex" reconstructed surface. 67
4.8 (a) The integrated intensity of the reconstruction peak (black points) and the $(0,1,0.3)$ CTR peak (red points) measured at different electrode potentials for the reconstructed Au(111) surface. (b) The stripe separation, p is also shown, as well as (c) the domain size, L of the $(p \times \sqrt{3})$ reconstruction, which are calculated from the fitted data (as shown in Figure 4.6). 68
4.9 The potential dependent surface charge per atom obtained for the reconstructed (a) Au(001) and (b) Au(111) surfaces by comparing the experimental electro-compressibility to the compressibility for a 2D layer in the free electron model 70
4.10 In plane x-ray diffraction of the reconstructed (a) Au(001) surface measured along the $[110]$ direction through the reconstruction peak and (b) the reconstructed Au(111) surface measured along the $[110]$ direction through the $(0,1,0.3)$ CTR position and the reconstruction peak, with both surfaces in CO saturated 0.1 M KOH electrolyte. The potential was held at: -1.0 V (red curves), -0.5 V (green curves) 72
4.11 X-ray voltammetry measurements showing the potential dependence of the scattered x-ray intensity from the $(0,0,1.02)$ anti-Bragg position on the specular CTR as the potential is swept from -1.0 V to 0.4 V and back (sweep rate = 2 mVs^{-1}). Results are shown for the Au(001) surface in 0.1 M KOH before (green and grey points) and after (red and blue points) the electrolyte was saturated with CO. Positive and negative potential sweeps are indicated by arrows 73
4.12 Fitted curves to the scattered x-ray intensity scanned along the $[110]$ direction measured through the $(0,1,l)$ CTR (left peak) and the reconstruction peak (right peak) for the Au(111) surface in 0.1 M NaOH electrolyte solution. Scans measured while holding the potential at 0 V (grey), -0.2 V (black), -0.4 V (blue), -0.6 V (green), -0.8 V (yellow) and -1.0 V (red). Inset plot shows the curve (green line) fitted to the x-ray data (black points) for the -0.6 V measurement. 74

4.13 (a) The x-ray intensity, (b) p and (c) domain size, L as a function of potential for the Au(111) in 0.1 M LiOH system when the reconstruction is investigated along the $[\bar{1}\ 2\ 0]$ direction. The x-ray intensity shown is that of the reconstruction peak. 76
4.14 (a) The x-ray intensity, (b) p and (c) domain size, L as a function of potential for the Au(111) in 0.1 M NaOH system when the reconstruction is investigated along the $[1\ 1\ 0]$ direction. The x-ray intensity shown is that of the reconstruction peak. 77
4.15 (a) The x-ray intensity, (b) p and (c) domain size, L as a function of potential for the Au(111) in 0.1 M CsOH system when the reconstruction is investigated along the $[1\ \bar{2}\ 0]$ direction. The x-ray intensity shown is that of the reconstruction peak. 78
4.16 The potential dependence of surface charge per atom for the reconstructed Au(111) surface in (a) LiOH, (b) NaOH and (c) CsOH electrolytes. Charges calculated from the experimental electro-compressibility and comparison with the 2D compressibility in the free electron model. 80

5.1 Cyclic voltammetry measurements made with scan rate = 0.02 V s^{-1} of the Cu(111) surface in phosphate buffer solution at (a) pH = 6 and (b) pH = 8, with phosphate concentrations of 0.01 M (red curve), 0.05 M (blue curve) and 0.1 M (green curve). Charge involved in the oxidative (blue) and reductive (red) processes on the Cu(111) surface in phosphate buffer solution at (c) pH = 6 and (d) pH = 8. 86
5.2 X-ray voltammetry measurements measured at the $(0, 1, 0.5)$ non-specular anti-Bragg position (solid line) and the $(0, 0, 1.4)$ specular anti-Bragg position (dotted line) on the CTR, with sweep rate = 2 mV s^{-1}. Blue points show the integrated intensity obtained from rocking scan measurements at the $(0, 1, 0.5)$ position at select potentials. 87
5.3 The (a) full width half maximum (FWHM) and (b) integrated intensity of x-ray rocking scans measured at the $(0, 1, 0.5)$ non-specular CTR position over the course of the experiment with respect to the applied electrode potential. Blue points were measured when stepping potential from -1 V to -0.7 V, red points from -1 V to -0.5 V and green points from -0.8 V to -0.6 V. (c) Peak profiles of two example rocking scans, measured at -0.9 V and -0.6 V (blue points and red points respectively) are shown along with Lorentzian line shapes fitted to the data (grey curves). These scans are highlighted by yellow circles in (a) and (c). 89

5.4 CTR data measured at -0.8 V (blue symbols) and -0.5 V (black symbols) presented with calculated fits to the data (green and red curves respectively) for the Cu(111) surface in 0.1 M phosphate buffer solution at pH = 8. 90
5.5 Schematic diagram showing the structure changes observed at the Cu(111) surface as the potential was stepped from -1.0 V to -0.8 V to -0.5 V. 91
5.6 Model parameters used to fit the CTR data in Figure 5.4 are shown as a function of potential. (a) The coverage (θ) of the surface Cu layer (red points) and adsorbed O layer (blue points). (b) The relaxation, $-\varepsilon_{Cu}$ of the 1st Cu layer (red points) and the 2nd Cu layer (blue points). (c) The roughness of the surface as modelled through a β roughness factor. (d) The relaxation, $-\varepsilon_{O}$ of the adsorbed O layer. 92
5.7 Non-specular CTR data measured at -0.8 V (blue symbols) and -0.5 V (black symbols) presented with calculated fits to the data (green and red curves respectively) for a different Cu(111) sample preparation in 0.1 M phosphate buffer solution at pH = 8. 94
5.8 Model parameters used to fit the CTR data in Figure 5.7 are shown as a function of potential. 96
5.9 Schematic diagram showing the structure changes observed at a region of the twinned Cu(111) surface as the potential was stepped from -0.8 V to -0.5 V and back again. 97
5.10 The (a) full width half maximum (FWHM) and (b) integrated intensity of x-ray rocking scans measured at the $(0, 1, 0.5)$ non-specular CTR position with respect to applied electrode potential for the Cu(111) sample which exhibited additional peaks in the CTR data (Figure 5.7) over the course of the experiment. Blue points were measured while stepping the potential from -0.8 V to -0.5 V and red points from -0.8 V to -0.7 V. 98
5.11 Peak potentials from cyclic voltammograms as a function of the log of the scan rate for Cu(111) in phosphate buffer solution with (a) pH = 6 and (b) pH = 8. 100

6.1 The c (2×2)-Cl adlayer superstructure formed at the Cu(001) surface. . . . 108
6.2 Top-down schematics showing the (a) $c(5\sqrt{2} \times \sqrt{2})R45°$ and (b) $c(4 \times 4)$ UPD Pb structures on Cu(001) reported in the literature. 110
6.3 Fitted CTR data measured for the Cu(001) surface in iodine electrolyte . . . 114
6.4 Energy scans through the Cu-K edge measured for the RSXRD signal from Cu(001) in 0.1 M $HClO_4$ + 10 mM KI electrolyte solution at -0.5 V electrode potential. 117

6.5 Stationary x-ray rocking scans carried out on the Cu(001) surface during dissolution of the UPD-Pb layer at the (a) $(0.5, 0.5, 0.6)$ and (b) $(1, 1, 1.7)$ reciprocal lattice positions as the applied potential was stepped from -0.4 V to -0.1 V. 120
6.6 Fit results from rocking scans carried out on the Cu(001) surface during dissolution of the UPD-Pb layer at reciprocal lattice positions along the $(0.5\ 0.5\ l)$ fractional order rod. 122
6.7 Fitted CTR data of the Cu(001) surface during dissolution of the Pb UPD layer. 124
6.8 Ratio of CTR intensity profiles measured at -0.4 V to those measured at -0.48 V for the Cu(001) surface during dissolution of the Pb UPD layer. . . 125
6.9 Resonant surface x-ray diffraction measurements of the Cu(001) surface as the Pb UPD layer is removed. 128

List of Abbreviations

Acronyms / Abbreviations

AFM	Atomic force microscopy, atomic level imaging of surfaces achieved by scanning a tip over the surface and monitoring the electromagnetic force between sample and probe to determine the sample-tip distance.
anti-Bragg position	A position along the CTR in reciprocal space that is halfway between two Bragg peaks and most sensitive to the surface structure.
CTR	Crystal truncation rod, a rod of non-zero intensity due to diffraction from a terminated crystal.
CV	Cyclic voltammetry, an electrochemical technique that involves measuring the current response of an electrochemical system with respect to potential changes.
DFT	Density functional theory.
DWF	Debye-Waller factor, a factor that accounts for disorder in the bulk crystal due to thermal energy of the atoms.
fcc	Face-centred cubic, a basic cubic crystal structure where there is one atom at each vertex of the cube and an atom at the centre of each of the cube's faces.
FWHM	Full width half maximum, the full width across a symmetrical peak measured at half its maximum intensity.
hcp	Hexagonal close-packed, a common way for atoms to be arranged in metals where space between atoms in minimal.

IHP	Inner Helmholtz plane, the plane on the liquid side of the solid-liquid interface parallel to the electrode surface plane, separated from the electrode surface by a distance equal to the radius of a partially solvated ion.
OHP	Outer Helmholtz plane, the plane on the liquid side of the solid-liquid interface parallel to the electrode surface plane, separated from the electrode surface by a distance equal to the radius of a solvated ion.
PCTFE	Polychlorotrifluoroethylene, also known as Kel-F
PTFE	Polytetrafluoroethylene, also known as Teflon
pzc	Potential of zero charge, potential for a specific electrode at which the charge is neither positive nor negative.
rms	Root-mean-squared, the square-root of the arithmetic mean of the squares of a set of numbers.
RSXRD	Resonant surface x-ray diffraction
SHE	Standard hydrogen electrode, a platinum electrode in a theoretical ideal solution, used as the standard electrode whose electrode potential is defined as 0 V at any temperature.
STM	Scanning tunnelling microscopy, atomic level imaging of surfaces achieved by scanning an atomically sharp conducting tip over the surface to induce quantum tunnelling of electrons.
SXRD	Surface x-ray diffraction, a technique that involves applying x-ray diffraction to measure the atomic surface structure.
UHV	Ultra-high vacuum, low pressure conditions ($< 10^{-7}$ Pa) commonly used in surface science experiments.
UPD	Underpotential deposition, the deposition of metal ions on a substrate which occurs at negative potentials above the Nernst potential, forming a monolayer.
XAS	X-ray absorption spectroscopy
XPS	X-ray photoelectron spectroscopy

XRV	X-ray voltammetry, voltammetry measurement made while monitoring the diffracted x-ray signal

Chapter 1

Introduction

Batteries, fuel cells and supercapacitors are widely understood to be key technologies in addressing the worsening energy crises that face our species on this planet. The importance of continued development of renewable energy technologies is difficult to understate as countries strive to address their reliance on fossil fuels for energy and mitigate the impending issues related to a changing climate. Central to many renewable energy and energy storage technologies, are electrochemical reactions that occur at the interface between solid and liquid materials. The electrochemical solid-liquid interface is where important reactions occur as part of a wide range of processes, accompanied by the transfer of electric charge across the interface. Obtaining electrical energy from a battery relies on electrochemical reactions at interfaces within, and the electrochemical conversion of greenhouse gases into useful products occurs at electrochemical interfaces at a catalyst surface. Reactions at electrochemical interfaces have many other applications outside of energy technologies, for example in the fields of electroplating, materials processing and sensor technologies.

Along with the research and development of energy technologies, the study of fundamental principles behind these technologies is also important for their outlook. For example, fundamental studies of electrocatalysts, and the underlying reasons behind their desired effects, can inform the future practical applications of those electrocatalysts, which may have impact for a range of technologies and industries. The fundamental study of atomic structure at the electrochemical interface, the point at which electronic charge is transferred between liquid and solid components of cells and other electrochemical systems, has implications for a multitude of applications. Improved understanding of the processes occurring at key interfaces in technology can offer rich details that may aid their development, and the reactions at electrochemical interfaces have shown to be strongly dependent on the structure of the interface, at the atomic level.

Electrode surfaces, where electrochemical reactions take place in a cell, can be studied by a range of experimental techniques, but few can provide *in situ* detail of the atomic structure of submerged electrode surfaces in liquid electrolyte. The ability to detect changes in atomic structure requires high resolution probing on the pm ($\times$ 10^{-12} m) scale. Atomic force microscopy (AFM) and scanning tunnelling microscopy (STM) are imaging methods that can provide high resolution detail of the surface atomic layer of electrodes, however these methods are not suitable for measuring subsurface atomic layers. In order to build up a full, three-dimensional picture of an electrode surface atomic structure, it is necessary to consider multiple layers. Along with surface stress measurements, surface x-ray diffraction (SXRD) is an experimental technique that facilitates high-resolution, *in situ* probing of atomic surface structure at the electrochemical solid-liquid interface. SXRD can be used to build up a three-dimensional picture of the surface structure for single crystal metal electrodes [1, 2]. Measurements of extended specular x-ray reflectivity can also reveal data on the liquid layering in the electrolyte side of the solid-liquid interface [3].

SXRD also provides detail on reconstructed surface structure and the structure formed by adsorbed species at the surface. By utilising the principles of diffraction from a surface, spectroscopic information about specific atoms at an electrode surface may also be obtained, by carrying out resonant surface x-ray diffraction (RSXRD) experiments. This can provide detail on the charge distribution at the surface. Performing such experiments *in situ* means that researchers may investigate how changes in the structure of electrochemical interfaces are related to the reactions that occur there, and how the structure may influence the reactivity of surfaces. This has the potential of offering signifiant insights for the field of catalysis.

Disadvantages of SXRD include the necessity of high intensity radiation, or long exposure times. To resolve the surface signal from background scattering due to the bulk crystal, sufficient counting statistics are required in the x-ray measurement. The use of a high intensity x-ray source, such as a synchrotron light source, provides this, as the more photons per second in the x-ray beam, the more diffracted photons reach the detector per second. A high intensity x-ray beam also accounts for the x-ray attenuation that occurs in the liquid electrolyte during a SXRD investigation of the solid-liquid interface. This is a disadvantage due to the difficulty in acquiring access to a synchrotron facility to conduct an experiment, where beam-time is limited. The alternative to a high intensity x-ray source would be operating with very long exposure times using a lab x-ray source.

Another disadvantage of the technique is that it is currently only applicable to well-ordered single crystal samples, and is not suitable for the investigation of nano-crystals. Therefore, it is more suitable for fundamental studies of electrochemical systems and investigation of single crystal surfaces in electrochemical systems.

The following pages detail work that was carried out by applying surface x-ray diffraction techniques to study the structure changes that occur at the solid-liquid interfaces of a range of model electrochemical systems. Chapter 4 details an investigation of the hexagonal atomic reconstruction that has been reported at gold (Au) surfaces in hydroxide. An in-plane restructuring of the atoms that make up the Au surface occurs, which can be observed via surface x-ray diffraction. Gold is an important catalyst for the oxidation of carbon monoxide (CO), a greenhouse gas and toxic product of combustion engines. The Au surface in the presence of CO is also useful for the electrochemical oxidation of alcohols, resulting in sought-after organic products. The aim of this investigation was to develop the understanding of the atomic reconstruction occurring at the surface to see if this could be behind gold's suitability as a catalyst.

Chapter 5 presents a study of the (111) surface of copper (Cu) electrodes in phosphate buffered electrolyte. Investigating the stability of the surface structure aimed to develop a better understanding of the reactivity of copper electrode surfaces, which, along with copper oxide-derived surfaces, are unique as catalysts for the electrochemical conversion of carbon dioxide (CO_2) into useful organic products. This process can produce a range of products, but the reasons behind the production of specific species is not yet fully understood, so more detail on the surface structures formed in different conditions and their stabilities could prove to be of great value.

Finally, Chapter 6 shows the findings of an investigation into the changes in charge distribution and atomic structure at the (001) surface of Cu during the electrochemical processes of halide ion adsorption and the dissolution of an underpotential deposited layer of lead (Pb) atoms. The aim was to show how resonant surface x-ray diffraction may be employed to understand the charge transfer between the copper electrode and the adsorbed or deposited species, and the nature of the bonding. Halide ions have been shown to affect the reactivity of electrodes, which has implications for industry and research in the fields of galvanic deposition, etching, corrosion and electrocatalysis. Underpotential deposited Pb layers on Cu surfaces are useful in catalysis, as they can be used to suppress competing reaction channels during CO_2 electroreduction.

The studies of reactions in model systems that are detailed in this work are aimed primarily at furthering the fundamental knowledge of electrochemical systems. However, it is clear that a greater understanding of processes in these model examples of solid-liquid interfaces is relevant to better understanding the behaviours and phenomena that occur at electrochemical interfaces applied in cutting edge technologies. The electrochemical systems investigated in subsequent chapters have implications for catalysis, in the conversion of unwanted greenhouse

gases that are the product of many everyday industrial and transportation processes into useful chemical products.

The next chapter (Chapter 2) will provide information on the theoretical principles behind the work. The experimental methods by which the experiments were conducted will be described in Chapter 3. Conclusions on the work are presented in Chapter 7.

Chapter 2

Theoretical Principles

2.1 Introduction

This chapter will explore the theoretical principles that are key to understanding the research presented in the subsequent chapters of the thesis. Section 2.2 will describe the basic principles behind the electrochemical processes that were investigated as part of the experiments that were carried out. The structural changes associated with electrochemical processes were determined by an experimental technique known as surface x-ray diffraction, the theory of which is explained in Section 2.3. An overview of single crystal structure is presented in Section 2.4 to provide an understanding of the single crystal samples that were investigated and the structure changes that may occur at the sample surface. Section 2.5 provides detail on how the surface structure is modelled in order to interpret the experimental results and in Section 2.6, the combination of surface x-ray diffraction and cyclic voltammetry as a technique called x-ray voltammetry will be described.

2.2 Electrochemistry

Electrochemistry is an area of chemistry concerned with the interplay of electrical charges and chemical reactions. An electrochemical process may involve an electric charge influencing a chemical change, or a chemical reaction influencing a change in electric charge. Electrochemistry explains how batteries work, why iron rusts and is the science behind electrolysis and electroplating. It has applications in fields as wide-ranging as renewable energy (fuel cells), the food industry (quality control analysis) and in forensic sciences (breathalysers).

Electrochemical systems are made up of electrodes and electrolytes, which allow the transfer of electric charges. An electrode is a conductor (a material that allows the flow of

electric charge) that makes contact with a non-metallic part of a circuit such as an electrolyte [4]. An electrolyte is an ionic conductor, made up of cations and anions dispersed throughout a solvent. A simple example of an electrolyte is salt (NaCl) dissolved in water, where the cations and anions are Na^+ and Cl^- respectively and water is the solvent.

Heterogeneous reactions occur between the electrode and electrolyte, where reactants are in solid and liquid phases. During these electrochemical reactions, charge is transferred either to or from the electrode in a galvanic process. Charge transfer occurs by the movement of negatively charged electrons. Transfer of electrons from an electrode occurs at the cathode, with a species being reduced by the electrons in a cathodic process. Electrons are transferred to the electrode (the anode) in anodic processes, where species are oxidised by losing electrons. Reduction is the process in which a species (atom or molecule) gains an electron and oxidation is the opposite process, where a species loses an electron.

2.2.1 Galvanic Electrode Reactions

Considering a simple electrochemical system with one cathode and one anode separated by an electrolyte, the reduction and oxidation processes that occur at the cathode and anode are two half-reactions. Though occurring at different electrodes either side of the electrolyte, these half-reactions are linked, in contact due to the ionic conductive electrolyte.

The reduction and oxidation half-reactions are shown in (2.1), where R is the reductant (species to be reduced) and O is the oxidant (species to be oxidised).

$$\begin{aligned} \mathrm{R} + e^- &\rightharpoonup \mathrm{R}^- \\ \mathrm{O} &\rightharpoonup \mathrm{O}^+ + e^- \end{aligned} \tag{2.1}$$

In electrochemical reduction, heterogeneous electron transfer occurs between an electrode and the reductant in separate phases (for example solid and liquid phases respectively). In a chemical reduction reaction, homogeneous electron transfer occurs between an oxidant and reductant in the same phase. The electron transfers from oxidant to reductant in chemical reduction because the lowest unoccupied molecular orbital (LUMO) of the reductant is at a lower energy level than the electron sitting in the oxidant's highest occupied molecular orbital (HOMO). Therefore, it is thermodynamically favourable for the electron to transfer from the oxidant's HOMO to the reductant's LUMO, and hence the redox reaction occurs with the difference in energy levels driving the reaction.

Electrodes are conductors, in which valence electrons may move freely throughout the lattice of positive ions as per the free electron model [5]. In a conductor there is a continuum

of energy levels, with the Fermi level defined as the highest occupied energy level at 0 K. The Fermi level in an electrode is related to the potential of the electrode, which is controlled by an external power source, such as a potentiostat. This allows the energy of electrons in the electrode to be controlled: a negative potential applied to the electrode increases the Fermi level of the electrode and a positive potential decreases the Fermi level. At a cathode, reduction of a species occurs when the energy of the electrons in the cathode is higher than the LUMO of the reductant. Electrons are transferred due to the energy difference between the electrode Fermi level and the LUMO of the molecular species at the cathode. Similarly, when the Fermi level in the anode falls below the HOMO of the oxidant species, oxidation occurs with an electron transferred from the HOMO to the electrode.

In combination, the overall half-reactions at the two electrodes form a redox reaction:

$$\mathrm{R} + \mathrm{O} \rightleftharpoons \mathrm{R}^{-} + \mathrm{O}^{+} \tag{2.2}$$

This redox reaction represents the processes occurring in the system as a whole, which in this case forms an electrochemical cell.

The cell has a potential associated with it, E^0_{cell} which is defined as the potential difference between the cathode and anode:

$$E^0_{cell} = E^0_{cathode} - E^0_{anode} \tag{2.3}$$

where the subscript 0 denotes standard conditions for the system, with the temperature assumed to be 298 K. The individual electrode potential, $E^0_{cathode}$ or E^0_{anode} is known as the redox potential for the half-reaction associated with that electrode. The potential difference across the cell must be E^0_{cell} for the redox reactions to occur.

A reaction occurring in the cell has an associated change in Gibbs free energy, ΔG and the more negative the change ΔG is, the more favourable the reaction is. ΔG is dependent on the cell potential:

$$\Delta G^0 = -nFE^0_{cell} \tag{2.4}$$

where n is the number of electrons transferred and $F \approx 96{,}500$ C mol^{-1} is the Faraday constant. This relation means that the cell potential E^0_{cell} determines how favourable the electrochemical reaction of the cell is, with a negative potential meaning the reaction is

spontaneous (energetically favourable to occur in the current conditions). A positive cell potential means the reaction is non-spontaneous and if $E^0_{cell} = 0$ the reaction is at equilibrium.

To calculate the Gibbs free energy change in non-standard conditions, the concentrations $[O]$ and $[R]$ of oxidants and reactants respectively in the electrolyte must be considered, as well as the temperature, T:

$$\Delta G = \Delta G^0 + RT \ln \frac{[O]}{[R]} \tag{2.5}$$

where R is the gas constant (~ 8.314 J K^{-1} mol^{-1}).

Applying (2.4) gives the Nernst equation:

$$\Delta E = \Delta E^0 - \frac{RT}{nF} \cdot \ln \frac{[O]}{[R]} \tag{2.6}$$

The Nernst equation shows that the concentrations of the species that make up the electrolyte influence the cell potential. As these concentrations change during redox reactions, the cell potential decreases until the reaction reaches equilibrium, with $\Delta G = 0$. No further reactions will occur at this point until a potential is applied as the net current in the electrochemical cell is zero.

The potential of an electrode cannot be independently measured, only the potential with respect to a reference electrode can be determined, such as a standard hydrogen electrode (SHE). SHE is a platinum electrode in a theoretical ideal solution and is used as the standard where its electrode potential E^0 is 0 V at any temperature [6]. The half-reaction for SHEs is:

$$2\mathrm{H}^+ + 2e^- \rightleftharpoons \mathrm{H}_2 \tag{2.7}$$

An electrode potential can be measured with respect to the SHE by making one of the electrodes in a cell SHE. Setting the electrode potential negative (vs SHE) will cause reduction at the cathode, as the Fermi level is pushed above the LUMO of the reductants in the electrolyte, and for a positive potential an oxidation reaction at the electrode will be driven. In a three electrode setup, current flows between the working electrode and counter electrode while the applied potential difference across the cell is measured by a third electrode, the reference electrode, which could be SHE or another electrode (such as Ag/AgCl) with a well-defined and stable equilibrium potential. A three-electrode setup with Ag/AgCl reference electrode has been used throughout this thesis.

2.2.2 The Solid-Liquid Interface

For electrochemical systems with a solid working electrode and liquid electrolyte, the electrochemical processes of interest are taking place at the solid-liquid interface. When reduction or oxidation occurs at such an electrode, charge is being transferred across the interface. In a galvanic process, considering the anode working electrode, anions in the electrolyte solution are attracted to the electrode surface, where the positive charge is concentrated due to an applied potential. There is no excess charge in the bulk of the electrode, as it is a good conductor. Layers of charge are formed, with the positively charged electrode surface considered as one layer and the negatively charged ions forming a layer at the liquid side of the interface. Models of the so called double-layer have been developed over time, with the first proposed by Helmholtz in 1853 [7, 8].

The Helmholtz model assumes the solid-liquid interface can be considered as a layer of charge at the electrode surface and a layer of ions on the liquid side of the interface, like a parallel plate capacitor. The excess charge density at the electrode surface is defined as q_M and the excess charge density in the solution is q_S. In order for the system to remain electro-neutral, the charges must be balanced:

$$q_M = -q_S \tag{2.8}$$

According to the Helmholtz model, the interface has a capacitance, C_H that depends on the distance, d between the electrode surface and the layer of ions, known as the outer Helmholtz plane (OHP).

$$C_H = \frac{\varepsilon_0 \varepsilon}{d} \tag{2.9}$$

where ε_0 is the permittivity of free space (8.8542×10^{-12} J^{-1} C^2 m^{-1}), ε is the ratio of the permittivity of the electrolyte and that of free space (the dielectric constant). In the Helmholtz model d is the radius of a solvated cation. Figure 2.1 illustrates the OHP as the distance of closest approach for fully solvated ions attracted to the oppositely charged electrode surface. Capacitance in this model is independent of potential and solution concentrations, and experimental observations found this to be insufficient for explanation of their findings [9].

Another model of the double-layer was proposed by Gouy in 1910 [10] and by Chapman three years later [11] where ions exist in a diffuse double layer, experiencing not just

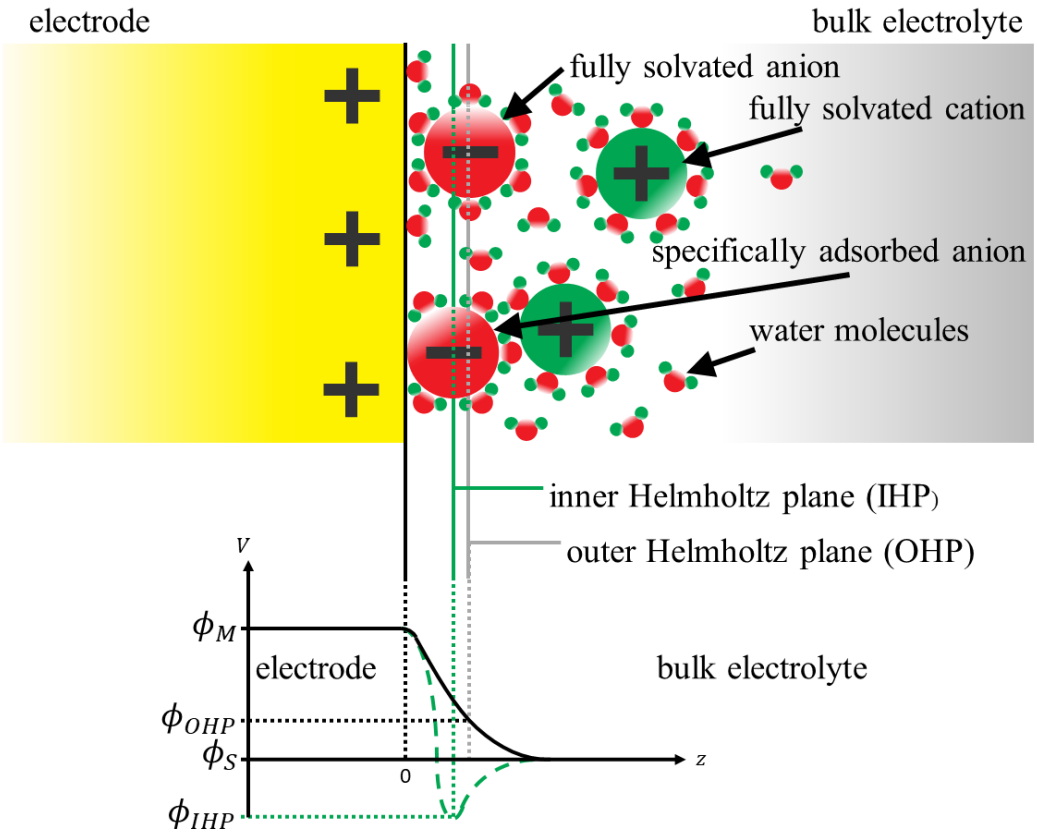

Fig. 2.1 (a) Schematic diagram of the Grahame model of the electrochemical double-layer, showing the electrode surface, the inner Helmholtz plane and the outer Helmholtz plane. (b) The corresponding potential drop across the interface for specifically adsorbed anions (green curve) and non-specifically adsorbed anions (black curve) is shown, where z is the distance in the direction normal to the electrode surface. The potentials inside the metal electrode, of the OHP, the IHP and inside the bulk electrolyte solution are represented by ϕ_M, ϕ_{OHP}, ϕ_{IHP} and ϕ_S.

interaction with the excess surface charge q_M but thermal motion within the solution. Ions are modelled as point charges dispersed by Brownian motion into the diffuse layer. Most of the excess charge in the solution q_S is concentrated close to the electrode, with the excess charge falling off further into the electrolyte. The distance to the OHP, d is replaced in the model by the average charge separation distance, which is dependent on potential and concentration.

$$C_{GC} = |z| F \left(\frac{2\varepsilon_0 \varepsilon c_b}{RT} \right)^{1/2} \cosh \left(\frac{|z| F \phi_0}{2RT} \right) \tag{2.10}$$

where z is the charge of the ions, c_b is the bulk electrolyte concentration and ϕ_0 is the potential at the surface.

The Gouy-Chapman model however was not found to be in agreement with experimental results beyond a small potential window either side of the potential of zero charge (pzc) for dilute solutions. The pzc is an electrode-specific potential at which the excess charge q_M is neither positive nor negative. The model takes ions to be point charges, with a distance of closest approach of zero, unlike the Helmholtz model, which defines the OHP as distance of closest approach. Both models were insufficient for describing experimental results [12] however both were combined by Stern to form a new model in 1924 [13].

The Stern model incorporates a layer of ions at the OHP and outside this layer, an ionic space charge forming the diffuse part of the double layer. This combination of two layers, with capacitance C_H and C_{GC} respectively models the solution side of the interface. The charge on the solution side of the interface, which balances the charge on the electrode surface as per (2.8) is spread between the compact layer and the diffuse layer. The model splits the potential drop across the interface into two components. The Stern model defines the total capacitance C_S as the result of two capacitors in series, corresponding to the compact and diffuse layers:

$$C_S = \frac{1}{C_H} + \frac{1}{C_{GC}} \tag{2.11}$$

The Stern model allows the calculation of double-layer capacitance in good agreement with experimental observations, but a further modification was made in 1947 by Grahame in his own model [14]. Grahame proposed to include in the model specifically adsorbed ions, the presence of which are possible if the ions have lost part of their solvation shell on approach to the electrode. Such specifically adsorbed ions will be closer to the electrode surface than fully solvated ions sitting in the OHP, and a closer plane housing these ions is

called the inner Helmholtz plane (IHP). The IHP is shown as part of the schematic of the double-layer in Figure 2.1.

The lower part of Figure 2.1 shows the potential drop across the electrochemical double layer in the Grahame Model. The potential drop differs for specifically adsorbed and non-specifically adsorbed (fully solvated) ions. The potential drop across the surface is assumed to be linear for non-specifically adsorbed ions, as indicated by the black line in Figure 2.1. For ions that are specifically adsorbed on the electrode surface, the potential drop is steeper, as indicated by the green dashed curve, with the potential of the IHP, ϕ_{IHP}, being lower than that in the bulk electrolyte, ϕ_S. The potentials inside the metal electrode and of the OHP are represented in the figure by ϕ_M and ϕ_{OHP} respectively.

2.2.3 Adsorption Phenomena

Electron transfer at the solid-liquid interface can influence other processes in the double layer, such as adsorption. An ion may be adsorbed at either the inner Helmholtz plane or the outer Helmholtz plane. Adsorption within the IHP occurs due to covalent (shared electron) or ionic (donated electron) bonding between the electrode substrate and adsorbate ions. This is known as chemisorption.

Adsorption within the OHP occurs due to electrostatic interactions (Van der Waals forces) between the surface and the adsorbate, without transferring an electron. This type of adsorption is called physisorption, and is a much weaker interaction than that which occurs during chemisorption. Physisorption does not involve a change in chemical bonding structure. An attractive electrostatic force will exist between a positively charged electrode surface, such as that shown in Figure 2.1 and a fully solvated anion due to the existence of an induced or permanent electric dipole in the electron orbitals of the ion. The same is true of a negatively charged surface and a fully solvated cation with an electric dipole. There exists an attractive electrostatic force between a charged electrode surface and the opposite charge on a polar ion.

2.2.4 Cyclic Voltammetry

Cyclic voltammetry (CV) is a widely employed electrochemical technique which allows the study of chemical reactions influenced by or involving electron transfer in an electrochemical cell [15]. The technique is often carried out with a three-electrode cell, where the reaction of interest occurs at the working electrode, the balancing reaction occurs at the counter electrode and the reference electrode is used to control the potential across the cell.

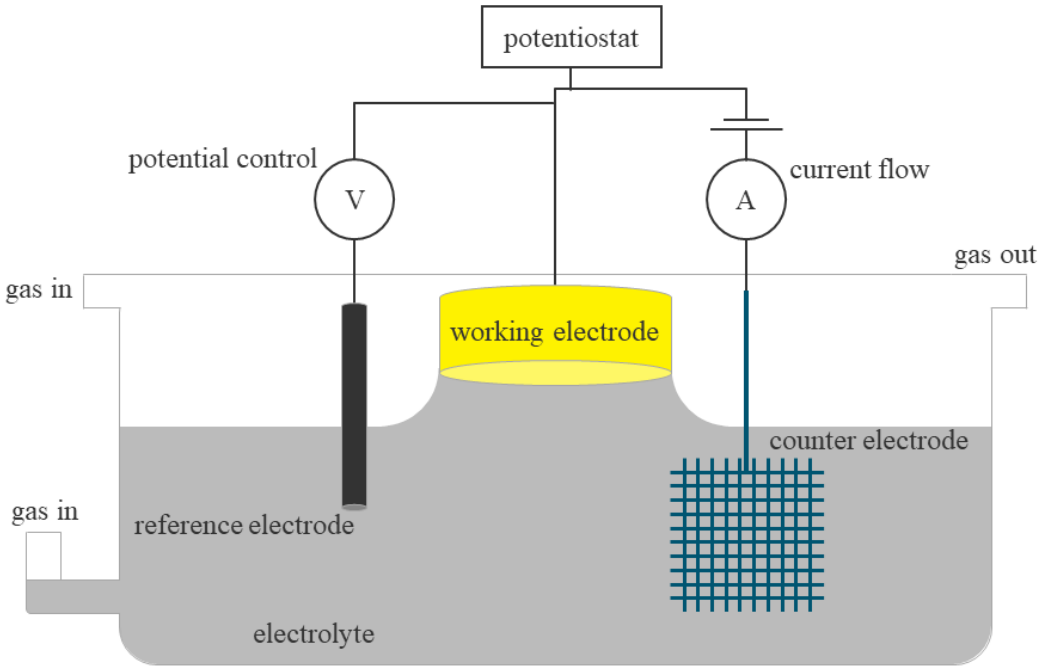

Fig. 2.2 Schematic of a three-electrode cell

Figure 2.2 shows a three-electrode setup, where in this case the working electrode is a single crystal sample surface. Different materials can be used for the working electrode in cyclic voltammetry depending on the process that is to be studied. The voltage is measured between the working electrode and the reference, however no current flows between these electrodes due to the high input impedance of the reference electrode. All current flows between the working and counter electrodes.

The counter electrode should have a large surface area, so that the kinetics of the reaction at this electrode do not limit the rate of reaction that can occur at the working electrode. Counter electrodes should be made of a sufficiently inert material (such as platinum or gold) as the purpose of this electrode is simply to complete the circuit with the reaction to be studied at the working electrode surface. The setup of a three-electrode electrochemical cell and potentiostat is further detailed in Chapter 3 (Experimental Methods), section 3.4.

In a CV measurement, the current travelling through the cell is measured as a function of the applied potential. CV measurements involve scanning the applied potential linearly while monitoring the current. A typical CV scan is measured over a potential window with a negative vertex and a positive vertex. The potential is scanned in one direction before being cycled back in the other. The plot of a CV measurement is known as a cyclic voltammogram.

An example of a simple cyclic voltammogram is shown in Figure 2.3, with potential swept linearly from a negative potential E_1 to a positive potential E_2 and then back again. During a

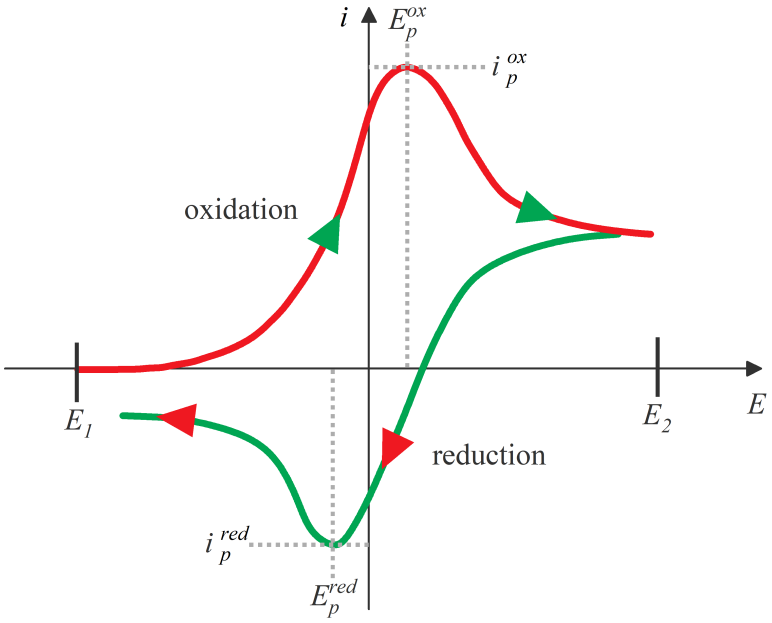

Fig. 2.3 Cyclic voltammogram for a reversible reaction

positive potential sweep, the current remains zero at first until the potential is positive enough for oxidation to occur at the working electrode surface, resulting in a measured current. The oxidant species is depleted at the electrode surface as the concentration of oxidised species increases.

The shape of a current profile and the concentrations of reductant and oxidant species at the surface depends on the potential applied and the speed at which species can move between the bulk electrolyte and the surface.

The volume of oxidised species localised at the electrode surface is known as the diffusion layer and as it grows, mass transport of the oxidant species to the electrode is slowed down. This reduces the current as the rate of reaction slows down, resulting in the current peak i_p^{ox} at E_p^{ox}.

The positive vertex of the scan E_2 is the switching potential, where the scan direction is reversed and the potential is swept in the negative direction. At this point there is an abundance of reductant species localised at the electrode surface, as a result of the oxidation during the positive sweep. As the potential becomes more negative, reduction occurs at the working electrode, and a current peak (i_p^{red}) will appear before the size of the diffusion layer becomes large enough to slow the rate of reduction (E_p^{red}). Corresponding oxidation and reduction peaks in the cyclic voltammogram profile may be separated along the potential axis, and the size of the separation depends on the time it takes for diffusion of the species within the electrolyte.

The shape of a voltammogram depends on factors such as the concentration of species in the electrolyte as well as the scan rate that the potential sweeps are conducted at.

Cyclic voltammetry is an experimental method that probes electron transfer and doesn't offer information related to the structure of the interface. To investigate the structure, CV can be combined with another technique, such as a type of microscopy or surface x-ray diffraction.

2.3 Surface X-Ray Diffraction

Surface x-ray diffraction is the principle experimental technique employed as part of the research presented in subsequent chapters. It uses the phenomena of x-ray diffraction to establish details about the atomic structure of a surface.

2.3.1 X-Ray Diffraction

Diffraction is a phenomenon that arises when a wave interacts elastically with a scatterer, such as a slit in a simple diffraction experiment, where scatterers act as secondary sources of the incident wave. The resulting wavefronts from the secondary sources interfere constructively and destructively to form a diffraction pattern.

An ideal crystal is a periodic arrangement of bases (atoms or groups of atoms) arranged in a three-dimensional lattice. Lattice vectors describe the direction and distance between lattice points and the basis of the lattice describes the atom or molecule that sits at each lattice point. The unit cell of the crystal determines a simple set of lattice vectors and bases that, if repeated, describe the entire crystal. A face-centred cubic (*fcc*) unit cell is a basic cubic crystal structure where there is one atom at each vertex of the cube and an atom at the centre of each of the cube's faces (Figure 2.4). This is the crystal structure of many metals, including copper, gold and silver and has the highest theoretical packing factor of any crystal structure, 0.74. A single crystal sample is a sample of a crystalline material, where the three-dimensional structure is repeated throughout the entire volume of the sample, as opposed to a polycrystalline sample. The electrons within periodically arranged atoms in a crystal act as scatterers in single crystal diffraction.

Different two-dimensional planes within the three-dimensional *fcc* unit cell may be defined, with the three lowest-index planes being defined by the Miller indices (0 0 1), (1 1 0) and (1 1 1) (Figure 2.5). Miller indices (h k l) define the plane that is orthogonal to the reciprocal space vector (h, k, l). A single crystal can be prepared with a surface cut along one of these planes. If radiation of a suitable wavelength, of the same order of magnitude

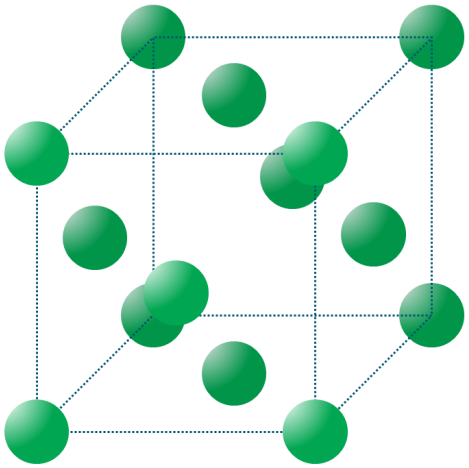

Fig. 2.4 Schematic of the *fcc* crystal structure.

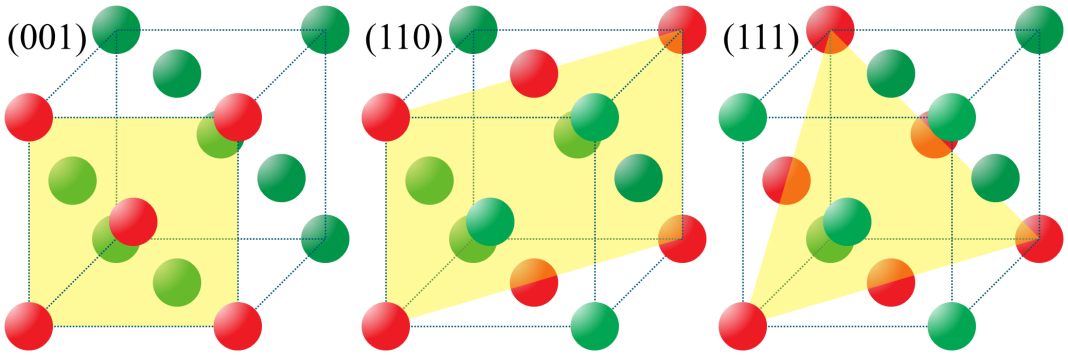

Fig. 2.5 The low index planes in an *fcc* unit cell, with the (a) (001), (b) (110) and (c) (111) planes shown in yellow.

as the inter-planar spacing of a crystal, is incident on a single crystal surface, diffraction occurs, where each atom in the structure acts as a secondary source of the incident radiation. Radiation is reflected from individual atoms due to Thompson scattering [16, 17], where the scattered amplitude A_1 from an incident wave of amplitude A_0 that scatters from an electron at a position $\mathbf{r}_e$ is given by

$$A_1 \mathrm{e}^{-\mathrm{i}\mathbf{k}_f \cdot \mathbf{r}_e} = A_0 \frac{e^2}{mc^2} \frac{1}{R_0} \mathrm{e}^{-\mathrm{i}\mathbf{k}_i \cdot \mathbf{r}_e} \tag{2.12}$$

where e and m are the electron charge and mass, R_0 is the distance to the detector and $\mathbf{k}_i$ and $\mathbf{k}_f$ are the incoming and outgoing wavevectors.

Bragg diffraction [18] is the phenomena where radiation scattered from different atoms in a crystal interferes constructively or destructively due to the periodic nature of the structure.

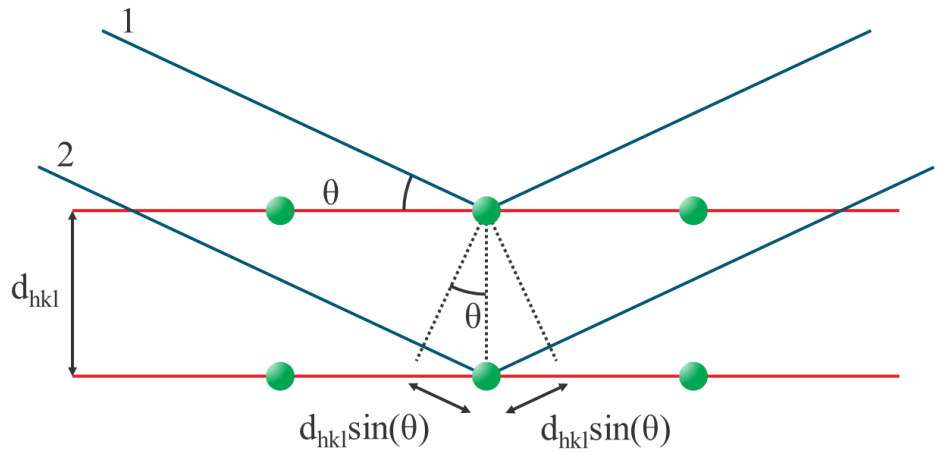

Fig. 2.6 Diagram of Bragg's law

A Bragg peak occurs due to constructive interference of the scattered radiation from different crystal planes. Planes in a crystal structure, such as an *fcc* metal, have a spacing of the same order of magnitude as the wavelength of x-rays, which is why x-ray diffraction is such an established method of investigating crystal structure, however both neutrons and electrons of similar wavelength are also used in scattering experiments. Bragg's law describes the condition for constructive interference leading to a Bragg peak measurement:

$$2d\sin\theta = n\lambda, \tag{2.13}$$

where d is the inter-planar spacing of the crystal, θ is the glancing angle the incident radiation makes with the crystal plane, n is a positive integer and λ is the wavelength of the incident radiation. This is illustrated in Figure 2.6.

In a simple single crystal x-ray diffraction experiment, Bragg peaks are detected as a sample, mounted on a goniometer, is rotated so that the angle θ corresponding to different order (n) Bragg peaks can be measured, allowing the d-spacing of the crystal to be determined.

In order to properly understand the x-ray diffraction signal from a real crystal, the contributions from every atom in the sample have to be considered. The calculation of the total scattering from the surface is built up by considering first the scattering from an individual atom, then a unit cell, the bulk crystal and a surface layer until the whole picture is realised, following explanations from the definitive publications on surface x-ray diffraction [18, 1, 19–21]. The kinematical approximation treats scattering as a single scattering event, occurring once in the sample. A structure factor is applied in order to determine the scattering intensity from the sample surface. The kinematical approximation is only valid for weak

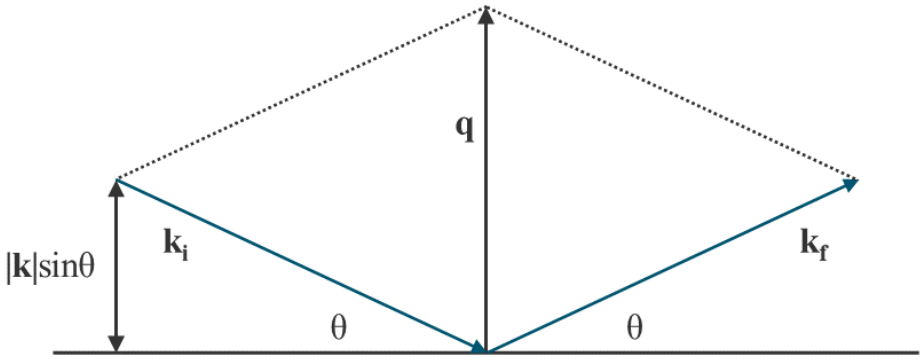

Fig. 2.7 Diagram showing momentum transfer **q** during elastic scattering

scattering from a surface such as a metal, where the sample is an imperfect material which is made up of mosaic blocks. For a sample material such as Si, the kinematical approximation cannot be used as it is insufficient for calculating the intensity due to interference from many scattering events. For such a case, the dynamical approximation is used [22], but the experiments in this work are concerned exclusively with diffraction from metal sample surfaces, so the kinematical approximation is sufficient.

2.3.2 Momentum Transfer, **q**

Momentum transfer, **q** is defined as the difference between $\mathbf{k}_i$ and $\mathbf{k}_f$, the wave vectors of incident and diffracted x-rays

$$\mathbf{q} = \mathbf{k}_f - \mathbf{k}_i \tag{2.14}$$

The scattering is elastic for x-ray diffraction so the magnitudes of wavevectors $\mathbf{k}_i$ and $\mathbf{k}_f$ are given by

$$|\mathbf{k}_i| = |\mathbf{k}_f| = |\mathbf{k}| = \frac{2\pi}{\lambda} \tag{2.15}$$

where λ is the x-ray wavelength. From this, the magnitude of **q** can be determined (as shown in Figure 2.7) so that momentum transfer can be expressed in terms of λ and θ in the Bragg law:

$$|\mathbf{q}| = 2\,|\mathbf{k}|\sin(\theta) = \frac{4\pi}{\lambda}\sin(\theta) \tag{2.16}$$

Momentum transfer is the independent variable in a surface x-ray diffraction (SXRD) experiment, and substituting (2.16) into (2.12) gives the scattering amplitude for a single electron, A_1 in terms of $\mathbf{q}$:

$$A_1 = A_0 \frac{e^2}{mc^2} \frac{1}{R_0} \mathrm{e}^{-\mathrm{i}\mathbf{q}\cdot\mathbf{r}_e} \tag{2.17}$$

2.3.3 Scattering from a Single Atom

To calculate the scattering from an atom, A_2 by summing the scattering contributions of its constituent electrons, the electron density distribution is considered, giving the integral

$$\begin{aligned} A_2 &= A_0 \frac{e^2}{mc^2} \frac{1}{R_0} \int_{-\infty}^{+\infty} \rho(\mathbf{r}') \mathrm{e}^{\mathrm{i}\mathbf{q}\cdot(\mathbf{R}_n+\mathbf{r}_j+\mathbf{r}')} \, d^3\mathbf{r}' \\ &= A_0 \frac{e^2}{mc^2} \frac{1}{R_0} f(q) \mathrm{e}^{\mathrm{i}\mathbf{q}\cdot(\mathbf{R}_n+\mathbf{r}_j)} \end{aligned} \tag{2.18}$$

where $f(q)$ is the atomic form factor

$$f(q) = \int_{-\infty}^{+\infty} \rho(\mathbf{r}') \mathrm{e}^{\mathrm{i}\mathbf{q}\cdot\mathbf{r}'} \, d^3\mathbf{r}' \tag{2.19}$$

The form factor is the Fourier transform of the electron density of an atom. The form factor is a function of the magnitude of the momentum transfer, because the atom is assumed to be spherically symmetric. Values for the form factors of atoms are available in the International Tables for Crystallography [23].

2.3.4 Scattering from a Unit Cell

When summing the scattering contribution from atoms in a unit cell, A_3, form factors $f_j(q)$ for atoms of different chemical elements must be accounted for. For a unit cell with N_c atoms

$$\begin{aligned} A_3 &= A_0 \frac{e^2}{mc^2} \frac{1}{R_0} \sum_{j=1}^{N_c} f_j(q) \mathrm{e}^{\mathrm{i}\mathbf{q}\cdot(\mathbf{R}_n+\mathbf{r}_j)} \\ &= A_0 \frac{e^2}{mc^2} \frac{1}{R_0} F(\mathbf{q}) \mathrm{e}^{\mathrm{i}\mathbf{q}\cdot\mathbf{R}_n} \end{aligned} \tag{2.20}$$

where $F(\mathbf{q})$ is the structure factor

$$F(\mathbf{q}) = \sum_{j=1}^{N_c} f_j(q) \mathrm{e}^{\mathrm{i}\mathbf{q}\cdot\mathbf{r}_j} \tag{2.21}$$

The structure factor is the sum over all atoms in the unit cell, and is a function of the direction as well as magnitude of $\mathbf{q}$, because the scattering depends on the positions of atoms in the unit cell. The structure factor is the Fourier transform of the electron density in the unit cell.

2.3.5 Scattering from a Crystal

The scattering amplitude from a whole crystal, A_4 is taken to be the sum of the scattering from the constituent unit cells. For a 3D crystal, there are N_1 unit cells along one crystal axis, $\mathbf{a}_1$, N_2 along axis $\mathbf{a}_2$ and N_3 unit cells along axis $\mathbf{a}_3$. Origin positions of the unit cells are defined by

$$\mathbf{R}_n = n_1\mathbf{a}_1 + n_2\mathbf{a}_2 + n_3\mathbf{a}_3 \tag{2.22}$$

The scattering is therefore given by

$$A_4 = A_0 \frac{e^2}{mc^2} \frac{1}{R_0} F(\mathbf{q}) \sum_{n_1=0}^{N_1-1} \sum_{n_2=0}^{N_2-1} \sum_{n_3=0}^{N_3-1} \mathrm{e}^{\mathrm{i}\mathbf{q}\cdot(n_1\mathbf{a}_1+n_2\mathbf{a}_2+n_3\mathbf{a}_3)} \tag{2.23}$$

The structure factor accounts for the type of atom, while the summation will remain the same for all crystals. Taking one of the sums from the expression in isolation

$$\begin{aligned} S_N(\mathbf{q}\cdot\mathbf{a}) &= \sum_{n=0}^{N-1} \mathrm{e}^{\mathrm{i}\mathbf{q}\cdot n\mathbf{a}} \\ &= \frac{1-\mathrm{e}^{\mathrm{i}N\mathbf{q}\cdot\mathbf{a}}}{1-\mathrm{e}^{\mathrm{i}\mathbf{q}\cdot\mathbf{a}}} \end{aligned} \tag{2.24}$$

This expression defines the scattering amplitude for a one-dimensional crystal, made up of N atoms, and this is related to the scattering intensity. The intensity is the modulus squared of the amplitude. Applying Euler's formula and multiplying by the complex conjugate gives a function known in optics as the N-slit interference function:

$$|S_N(\mathbf{q}\cdot\mathbf{a})|^2 = \frac{\sin^2(\frac{N}{2}\mathbf{q}\cdot\mathbf{a})}{\sin^2(\frac{1}{2}\mathbf{q}\cdot\mathbf{a})} \tag{2.25}$$

The scattering amplitude (2.23) can be written in terms of the slit function:

$$A_4 = A_0 \frac{e^2}{mc^2} \frac{1}{R_0} F(\mathbf{q}) S_{N_1}(\mathbf{q}\cdot\mathbf{a}_1) S_{N_2}(\mathbf{q}\cdot\mathbf{a}_2) S_{N_3}(\mathbf{q}\cdot\mathbf{a}_3) \tag{2.26}$$

When N is large, as in the case of a millimetre-scale crystal sample, a slit interference function S_N has peaks at $\mathbf{q}\cdot\mathbf{a} = 2\pi m$, where m is an integer. The function gives rise to diffracted intensity along specific directions and in 3D, this forms a reciprocal lattice.

2.3.6 Reciprocal Lattice

The scattered intensity is given by

$$I(\mathbf{q}) = I_0 \frac{e^2}{mc^2} \frac{1}{R_0} |F(\mathbf{q})|^2 |S_{N_1}(\mathbf{q}\cdot\mathbf{a}_1)|^2 |S_{N_2}(\mathbf{q}\cdot\mathbf{a}_2)|^2 |S_{N_3}(\mathbf{q}\cdot\mathbf{a}_3)|^2 \tag{2.27}$$

where I_0 is the intensity of incident x-rays. The intensity is at a maximum when the following Laue conditions are satisfied:

$$\begin{aligned} \mathbf{q}\cdot\mathbf{a}_1 &= 2\pi h \\ \mathbf{q}\cdot\mathbf{a}_2 &= 2\pi k \\ \mathbf{q}\cdot\mathbf{a}_3 &= 2\pi l \end{aligned} \tag{2.28}$$

The Laue conditions must all be met for a diffraction peak to arise, where h, k and l are the Miller indices. The conditions are met when the momentum transfer satisfies

$$\mathbf{q} = h\mathbf{b}_1 + k\mathbf{b}_2 + l\mathbf{b}_3 \tag{2.29}$$

where the reciprocal lattice vectors $\mathbf{b}_x$ are related to the real space vectors $\mathbf{a}_x$

$$\begin{aligned} \mathbf{b}_1 &= 2\pi \frac{\mathbf{a}_2 \times \mathbf{a}_3}{\mathbf{a}_1 \cdot (\mathbf{a}_2 \times \mathbf{a}_3)} \\ \mathbf{b}_2 &= 2\pi \frac{\mathbf{a}_3 \times \mathbf{a}_1}{\mathbf{a}_2 \cdot (\mathbf{a}_3 \times \mathbf{a}_1)} \\ \mathbf{b}_3 &= 2\pi \frac{\mathbf{a}_1 \times \mathbf{a}_2}{\mathbf{a}_3 \cdot (\mathbf{a}_1 \times \mathbf{a}_2)} \end{aligned} \tag{2.30}$$

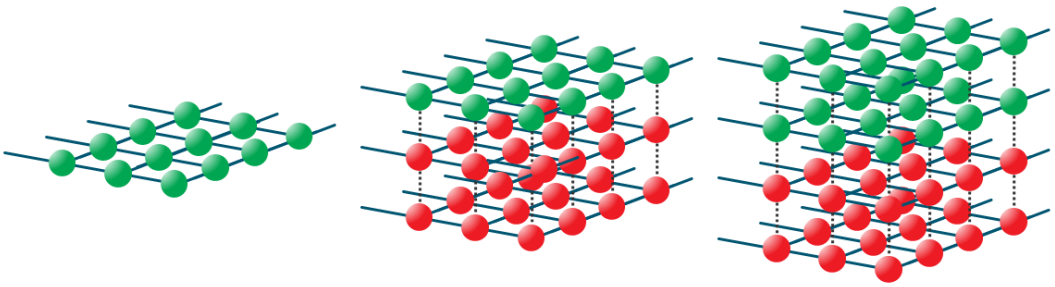

(a) (b) (c)

Fig. 2.8 Crystal surface schematic diagrams showing three types of surface/interface: (a) an isolated monolayer, (b) a terminated crystal and (c) a crystal-crystal interface.

The Miller indices form a 3D lattice of points and the reciprocal lattice vectors are orthogonal to the real space vectors that lie along the axes of the crystal. The reciprocal lattice vectors have units of inverse length. When the Laue conditions are satisfied, the 3D lattice of intensity (Bragg peaks) is formed, resulting in a diffraction pattern. The intensity is zero except for the discrete positions described by the Miller indices. The intensity at an $h\ k\ l$ reciprocal space position is given by

$$I_{hkl} = \left| A_0 \frac{e^2}{mc^2} \frac{1}{R_0} F(\mathbf{q}) N_1 N_2 N_3 \right|^2 \tag{2.31}$$

2.3.7 XRD from a Surface

So far, the scattering intensity has been calculated for an ideal crystal, where there are an infinite number of unit cells in all the three dimensions. To consider diffraction from the surface, the calculations must be adjusted for a truncated crystal. There are three types of surface that may be considered: (1) an isolated 2D monolayer (Figure 2.8a), (2) a truncated 3D crystal (Figure 2.8b), where the top layer is considered as a 2D monolayer, which can either have the same periodicity as the bulk or different, and (3) a crystal-crystal interface (Figure 2.8c) where a 3D crystal sits atop another.

To calculate the diffraction that results from these three cases, (2.26) can be applied. For a 2D monolayer, $N_3 = 1$, so the slit function $S_{N_3} = 1$ and the scattering is independent of the projection of the momentum transfer perpendicular to the surface ($\mathbf{q} \cdot \mathbf{a}_3$). This means that the diffracted intensity depends on the momentum transfer along the $\mathbf{a}_1$ and $\mathbf{a}_2$ directions only, resulting in intensity at discrete positions in the surface plane, and rods of continuous intensity orthogonal to the surface. This is illustrated in Figure 2.9a.

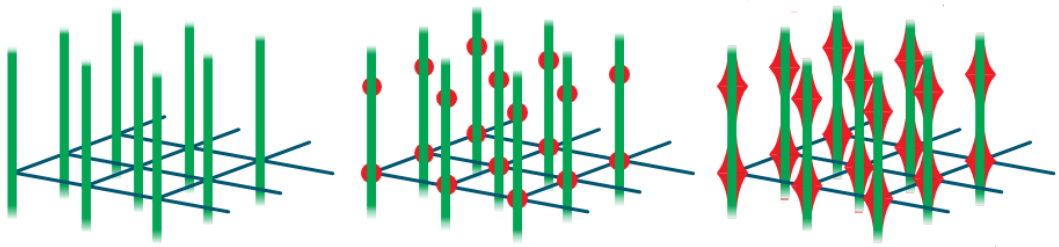

(a) (b) (c)

Fig. 2.9 Schematic diagrams showing the diffraction patterns resulting from three types of surface/interface: (a) a 2D layer, (b) the combination of a bulk crystal and 2D layer and (c) crystal truncation rods from a surface.

The scattering from a 2D layer on top of a bulk crystal is shown in Figure 2.9b, taking the form of a superposition of Bragg peaks, discrete in all three dimensions, from the bulk crystal and rods of continuous intensity from the surface layer. For a terminated crystal where the 2D surface layer has the same structure as layers of the bulk crystal, the surface rods will pass through the Bragg points. In a real surface x-ray diffraction experiment, all layers of the crystal contribute to the scattering and for large N, the numerator in expression 2.25, $\sin^2\left(\frac{N}{2}\mathbf{q}\cdot\mathbf{a}_3\right)$ varies with $\mathbf{q}$ and can be approximated to an average value of $\frac{1}{2}$. For large N, (2.25) becomes

$$\left|S'(\mathbf{q}\cdot\mathbf{a}_3)\right|^2 = \frac{1}{2\sin^2(\frac{1}{2}\mathbf{q}\cdot\mathbf{a}_3)} \tag{2.32}$$

This results in non-zero intensity at l values between the Bragg peaks, with the intensity varying along the surface normal, l. Known as crystal truncation rods (CTRs), this phenomenon is illustrated in Figure 2.9c, showing the streaks of scattering that surround the Bragg peaks along the l direction. Expression 2.32 gives an infinite value for scattering at the Bragg peaks as it is an ideal case. In reality, x-rays are absorbed by layers of the crystal so not all layers contribute equally.

CTRs are distinct from rods of scattering that arise from a 2D layer, although for a perfectly terminated crystal the two will be perfectly superimposed. If an adlayer is not registered perfectly with the substrate, or if the surface of a crystal is reconstructed, then the rods arising due to the surface layer will have a different periodicity and will not pass through the Bragg peaks.

2.4 Crystal Structure of Single Crystal Electrodes

The three low index surfaces of an *fcc* single crystal are the (111), (110) and (001) surfaces as presented in Figure 2.5. These surfaces have simple structures that are well understood and are therefore ideal for electrochemistry experiments and surface x-ray diffraction studies of electrochemical interfaces. The experiments detailed in this work were all measured on (111) or (001) surfaces of *fcc* metals.

2.4.1 The (111) Surface

The (111) surface is the most close-packed of the low index surfaces, as shown in Figure 2.5c. A schematic of the surface is shown in Figure 2.10a, with the atoms forming a hexagonal structure. There are three layers of atoms in the unit cell, and atoms sit in the *fcc* hollow sites of the layer below. This is known as ABC stacking, as shown in Figure 2.10c. It is also possible for atoms that sit on the surface to fall into the *hcp* hollow sites (Figure 2.10d), or to bridge and on-top sites, however a perfect (111) surface follows ABC stacking. The (111) unit cell is described by the unit cell vectors $\mathbf{a}_1$, $\mathbf{a}_2$ and $\mathbf{a}_3$, depicted in Figure 2.10a and 2.10b and is repeated every three layers. This results in the Bragg peaks in reciprocal space being separated by units of 3 along the l direction.

Reciprocal space vectors are defined such that $[h\ 0\ 0]_{hex}$ and $[0\ k\ 0]_{hex}$ lie in the surface plane and are separated by an angle of 60°, with l along the surface normal $[0\ 0\ l]_{hex}$ direction. The units of the miller indices are defined by

$$\mathbf{b}_1 = \mathbf{b}_2 = \frac{4\pi}{\sqrt{3}a_{NN}} \quad \text{and} \quad \mathbf{b}_3 = \frac{2\pi}{\sqrt{6}a_{NN}} \tag{2.33}$$

where a_{NN} is the nearest neighbour distance for atoms in the unit cell. The reciprocal space map of the (111) surface is presented in Figure 2.11 and shows the reciprocal lattice positions of Bragg peaks. Bragg peaks are indicated along the CTRs that arise due to the (111) surface, and they are shown to exhibit 120° symmetry.

The bulk cubic unit cell of the *fcc* crystal is related to the surface unit cell by transformation of the Miller indices:

$$\begin{aligned} h_c &= \frac{2}{3}h - \frac{2}{3}k + \frac{1}{3}l \\ k_c &= \frac{2}{3}h + \frac{4}{3}k + \frac{1}{3}l \\ l_c &= -\frac{4}{3}h - \frac{2}{3}k + \frac{1}{3}l \end{aligned} \tag{2.34}$$

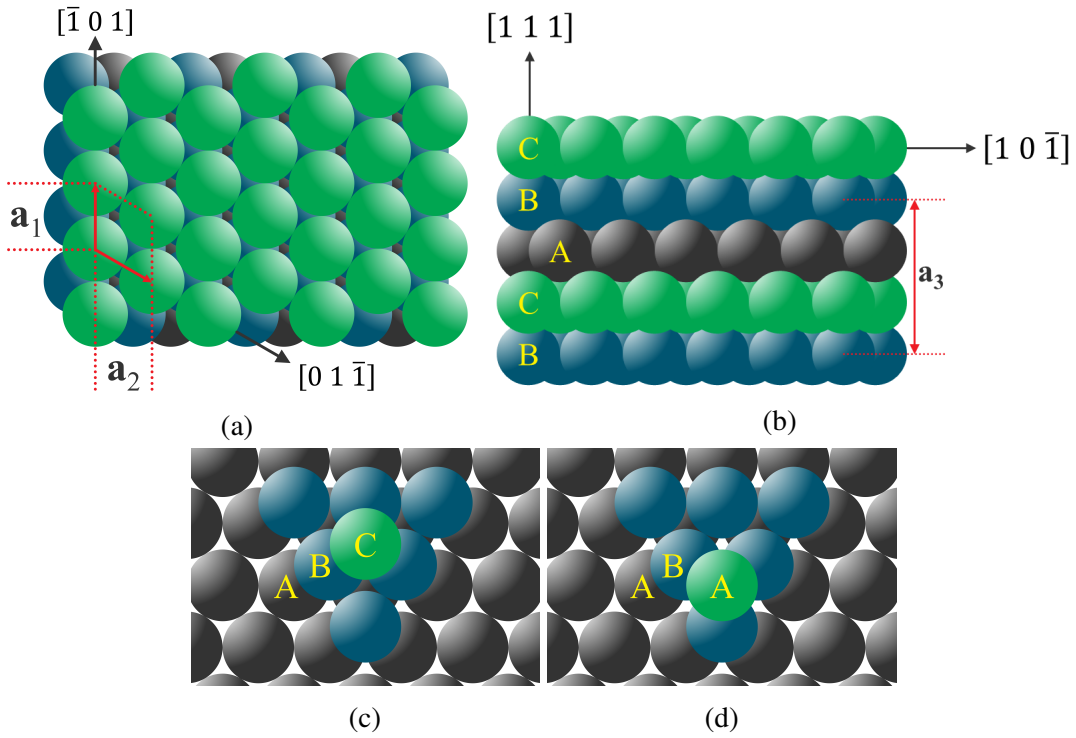

Fig. 2.10 Diagrams showing (a) top-down and (b) side-on schematics of the (111) surface and atomic stacking in (c) *fcc* and (d) *hcp* sites.

where the bulk cubic unit cell is defined by the perpendicular vectors $[h_c\ 0\ 0]_c$, $[0\ k_c\ 0]_c$ and $[0\ 0\ l_c]_c$. The Bragg peaks for an *fcc* crystal occur when the three bulk Miller indices h_c, k_c and l_c are all odd or all even, and applying the transformation (2.34) gives the positions of the Bragg peaks in terms of the surface unit cell, in h, k and l, as shown in Figure 2.11.

The intensity in the CTR can be calculated for the (111) surface by considering the structure factor, F (2.21) for the surface unit cell. The (111) unit cell has three layers in the l direction with atoms in the first layer at $(0,0,0)$, $\left(-\frac{1}{3},\frac{1}{3},\frac{1}{3}\right)$ and $\left(-\frac{2}{3},\frac{2}{3},\frac{2}{3}\right)$ relative to the unit cell vectors, resulting in a phase factor of $\mathrm{e}^{2\pi\mathrm{i}\left(-\frac{h}{3}+\frac{k}{3}+\frac{l}{3}\right)}$. We first consider the bulk contribution to the scattering, and the bulk structure factor F_{bulk}, by modelling the bulk as a semi-infinite single crystal:

$$F_{bulk} = f(q)f_{DWF}\sum_{j=0}^{-\infty}\mathrm{e}^{2\pi\mathrm{i}j\left(-\frac{h}{3}+\frac{k}{3}+\frac{l}{3}\right)} = \frac{f(q)f_{DWF}}{1-\mathrm{e}^{2\pi\mathrm{i}\left(\frac{h}{3}-\frac{k}{3}-\frac{l}{3}\right)}} \tag{2.35}$$

where $f(q)$ is the atomic form factor specific to the element making up the single crystal, f_{DWF} is the bulk Debye-Waller factor (DWF), a factor accounting for thermal vibrations in the bulk crystal due to the thermal energy of the atoms. Atoms are assumed to exhibit a rms displacement from their equilibrium position of σ. The root-mean-squared (rms)

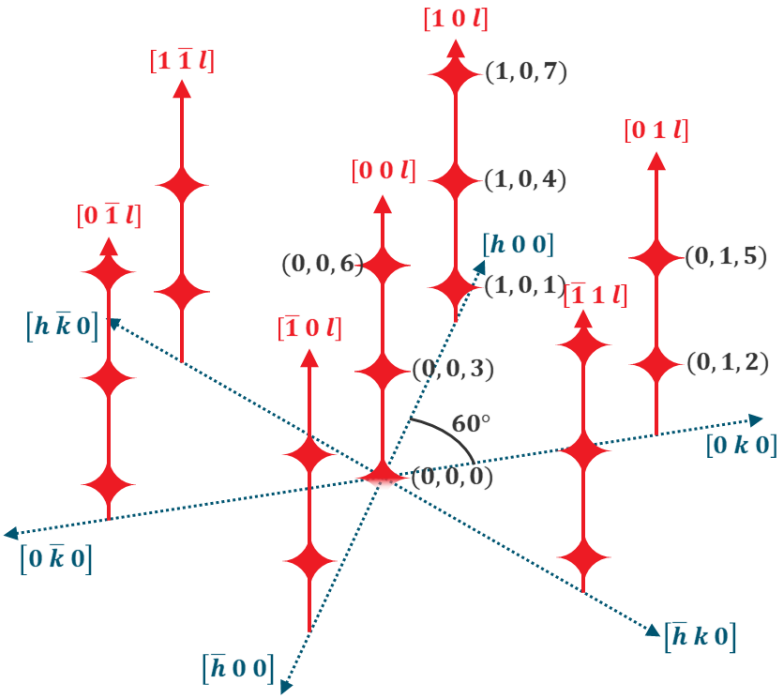

Fig. 2.11 Reciprocal space map of the (111) surface with directions and Bragg peak positions given in terms of the hexagonal surface unit cell vectors

displacement of atoms gives the Debye-Waller factor:

$$f_{DWF} = \mathrm{e}^{-\frac{1}{2}\mathbf{q}^2\langle\sigma_{\mathbf{q}}^2\rangle} \tag{2.36}$$

where $\langle\sigma_{\mathbf{q}}^2\rangle$ is the average atomic displacement:

$$\langle\sigma_{\mathbf{q}}^2\rangle = \frac{B}{8\pi^2} \tag{2.37}$$

where B is a factor with units of Å^2 tabulated in the International Tables for Crystallography [23].

The surface contribution to the CTR intensity must also be calculated when modelling a CTR, and for crystals which exhibit metallic bonding it is sufficient to model three surface layers of atoms atop a bulk semi-infinite crystal. For other materials, such as Si, more surface layers would be required to build an accurate model of the crystal surface. This is because the difference between the bonding experienced by atoms in a surface layer when a crystal is terminated and the bonding experienced by atoms in the bulk can apply to atoms multiple layers deep. The depth of layers depends on the bonding mechanism. The structure factor for

the surface layers of an *fcc* surface sample are given by

$$F_{surface} = \sum_{j=1}^{3} f(q) f_{DWF_j} \theta_j \mathrm{e}^{2\pi \mathrm{i} j\left(-\frac{h}{3}+\frac{k}{3}+l\left(\frac{1}{3}+\varepsilon_j\right)\right)} \tag{2.38}$$

where the Debye-Waller factor f_{DWF} is different for each layer, θ_j is the coverage factor of the layer ($\theta_j = 1$ for a fully occupied monolayer of atoms) and ε_j is an expansion factor, accounting for relaxation or expansion of the surface layer away from its equilibrium position. This frozen-in Debye-Waller factor models layer roughness as a static displacement of atoms, accounting for the average distances by which surface atoms are displaced. The Debye-Waller roughness factor for a layer is given by multiplying the bulk DWF by an individual component that depends on the momentum transfer along the surface normal:

$$f_{DWF_j} = \mathrm{e}^{-\frac{1}{2}\langle \mathbf{q}\sigma_{\mathbf{q}}\rangle^2} \cdot \mathrm{e}^{-\frac{1}{2}\langle \mathbf{q}_z\sigma_j\rangle^2} \tag{2.39}$$

The total scattered intensity of the CTR is given by

$$I_{CTR} = |F_{total}|^2 = \left|F_{bulk} + F_{surface}\right|^2 \tag{2.40}$$

2.4.2 The (001) Surface

The (001) surface of an *fcc* crystal is a more open structure than the close packed (111) surface. Atoms are arranged in the surface plane along two perpendicular axes forming a square structure, as shown in the top-down schematic of the surface in Figure 2.12a. Atoms are arranged in the out-of-plane direction with ABAB stacking as shown in Figure 2.12b and 2.12c so that atoms in a layer sit in the hollow sites of the layer below. The unit cell of the (001) surface is described by the vectors $\mathbf{a}_1$, $\mathbf{a}_2$ and $\mathbf{a}_3$ and is repeated in the out-of-plane direction every 2 layers, so Bragg peaks in the l direction are separated by 2. The units of the reciprocal space vectors are defined as

$$\mathbf{b}_1 = \mathbf{b}_2 = \frac{2\pi}{a_{NN}} \quad \text{and} \quad \mathbf{b}_3 = \frac{4\pi}{\sqrt{2}a_{NN}} \tag{2.41}$$

The reciprocal space map of Bragg peaks arising due to the (001) space is shown in Figure 2.13. The surface has 90° symmetry in the surface plane, and the tetragonal surface

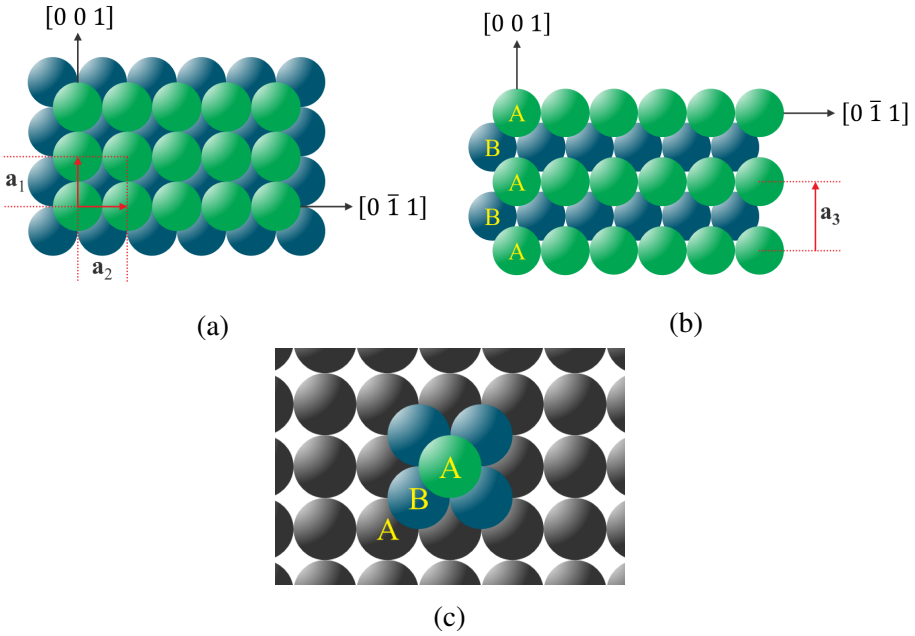

Fig. 2.12 Diagrams showing (a) top-down and (b) side-on schematics of the (001) surface and (c) ABAB stacking in *fcc* sites.

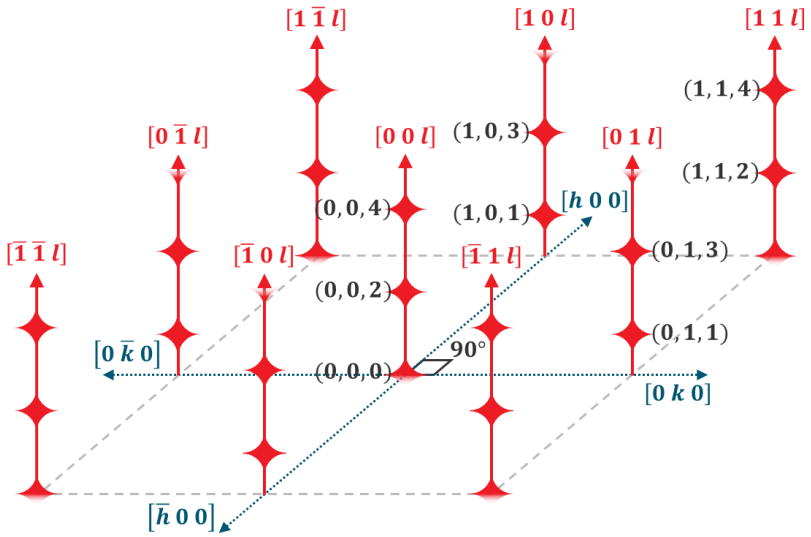

Fig. 2.13 Schematic diagram showing the reciprocal space map for the (001) surface given in terms of the tetragonal surface unit cell vectors

unit cell is related to the bulk cubic unit cell by the transformation of the Miller indices:

$$\begin{aligned} h_c &= h + k \\ k_c &= h - k \\ l_c &= l \end{aligned} \tag{2.42}$$

The (001) unit cell has atoms at $(0,0,0)$ and $\left(\frac{1}{2},\frac{1}{2},\frac{1}{2}\right)$ relative to the unit cell vectors resulting in a phase factor of $e^{2\pi i\left(\frac{h}{2}+\frac{k}{2}+\frac{l}{2}\right)}$. The intensity of the CTR is calculated by finding both the bulk component and the surface component of the structure factor. The bulk structure factor for the (001) surface will be

$$F_{bulk} = \frac{f(q) f_{DWF}}{1 - e^{2\pi i\left(\frac{h}{2}+\frac{k}{2}+\frac{l}{2}\right)}} \tag{2.43}$$

As for the (111) surface, the Debye-Waller factor is calculated by (2.36). The surface structure factor contribution for three surface layers of the (001) surface is

$$F_{surface} = \sum_{j=1}^{3} f(q) f_{DWF_j} \theta_j e^{2\pi i j\left(\frac{h}{2}+\frac{k}{2}+l\left(\frac{1}{2}+\varepsilon_j\right)\right)} \tag{2.44}$$

The intensity of the CTR I_{CTR} is calculated, as for the (111) surface (2.40), by summing the structure factors of the bulk and the surface layers and multiplying by the complex conjugate.

2.5 Modelling Surface Structure

Calculation of the structure factor for surface layers $F_{surface}$ (2.38) is dependent on the factors θ, ε and the Debye-Waller roughness factor which all have a significant effect on the intensity along the CTR, influencing the profile of the CTR.

θ is a factor accounting for the coverage or occupation of a surface layer, where $\theta = 1$ represents a fully occupied monolayer and a specific fraction of that factor indicates the fraction of surface sites that are occupied. The effect of different θ values on the CTR profile is shown in Figure 2.14. The black curve is a CTR plotted with the parameter θ set to 1 and ε set to 0, corresponding to a perfectly terminated (001) surface. The grey curve shows the effect of a partially (70%) occupied surface layer with a coverage of $\theta = 0.7$, where the intensity at points halfway between the Bragg peaks (anti-Bragg positions) is decreased. The anti-Bragg is the most sensitive point along the CTR to the surface structure, as it is the point at which contribution to the diffracted intensity from the bulk structure is at a minimum.

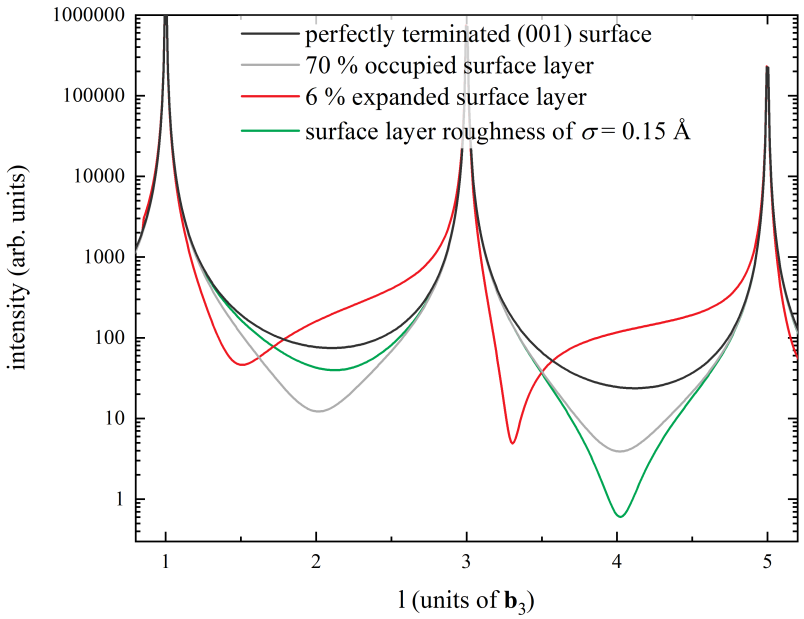

Fig. 2.14 The effect on the $(1,0,l)$ CTR profile from a Au(001) surface of altering parameters $\varepsilon = 0.06$ (red), $\theta = 0.7$ (grey) and $\sigma = 0.15$ (green)

The lower the occupation of the surface layer, θ, the lower the intensity at the anti-Bragg positions will fall. The scattering at the anti-Bragg is so weak compared with the Bragg peaks that if the intensity is too low the signal from the surface can be hard to distinguish from the background signal, so good counting statistics are important for a SXRD CTR measurement.

Changing the out-of-plane position of atoms in the model affects the shape of the CTR profile as well. The parameter ε represents the expansion factor, accounting for out-of-plane shift in the position of the surface layer in the model. A shift of $\varepsilon = 0.06$ indicates an expansion of the surface layer away from the layer below it, by a factor of 12 % of the layer spacing in this direction (2.33, 2.41), increasing the d-spacing. The expansion is 12 % because in an (001) unit cell, the layer spacing is half of the lattice constant, which ε is given in terms of. The effect of a 12 % surface expansion, as shown in Figure 2.14, is that the CTR profile becomes asymmetrical around the Bragg peaks. A negative value for ε models a relaxation of the layer, with the atoms moving closer to the layer below and reducing the d-spacing. Figure 2.14 illustrates the dramatic effect on the shape of the CTR profile that the θ and ε parameters may have, and that measuring CTR profiles can reveal a lot of detail about the surface structure of a single crystal.

The Debye-Waller roughness factor (2.36) is related to the rms surface roughness σ, which also affects the shape of a CTR profile. The effect of an rms roughness (displacement of atoms) of $\sigma = 0.15$ Å is shown in Figure 2.14, where the intensity at anti-Bragg positions

decreases, similar to the effect of reducing θ. The difference being that as l increases, the effect of σ is more dramatic and the intensity decreases by a larger amount. When modelling a CTR profile, these parameters are varied until the calculation fits the experimental data.

Another method of modelling the surface roughness, which can be useful is the β-factor [1]. Applying a β roughness factor models the surface as having a fully occupied layer of atoms, with a layer occupied by a fraction, β, of the total sites, then a layer with β^2 of the sites occupied, and so on. For an (001) surface, the β roughness model modifies the CTR intensity, I_{CTR} according to

$$I_{CTR} = \frac{(1-\beta)}{\sqrt{1+\beta^2-2\beta\cos\left(2\pi\left(-\frac{h}{2}+\frac{k}{2}+\frac{l}{2}\right)\right)}}\left|F_{total}\right|^2 \tag{2.45}$$

In order to contribute to the non-specular CTR, the scattering component must be commensurate with the metal lattice. For the specular CTR, $(0,0,l)$, where there is no in-plane momentum transfer, this condition is relaxed and the measurement probes the electron density profile along the surface normal direction. This can be sensitive to layering in the electrolyte.

The **q**-vector of the specular CTR, $(0,0,l)$, has no in-plane component. All the momentum transfer is along the surface normal direction. The specular CTR is the only rod that does not have any in-plane **q**-vector component, all non-specular CTRs do, and therefore non-specular CTRs are sensitive to the in-plane surface structure. The specular CTR is sensitive to the out-of-plane surface structure, as it depends on the out-of-plane charge distribution, meaning that information on the liquid layering in the sample can be obtained from the specular CTR.

Fractional order rods consist of scattering arising from surface structure that has a different symmetry to the bulk lattice. Unlike CTRs they do not pass through Bragg peaks, but lie elsewhere in the *h*-*k* plane. Fractional order rods can occur due to superstructure such as adsorbates on the surface or reconstruction of the surface layers.

2.5.1 Adlayer Structures

Species in the electrolyte may undergo adsorption onto the electrode surface under certain conditions. For example anions would favourably undergo adsorption at positive potentials, due to the positive charge present at the electrode surface and the negative charge of the anion species. Cations would be attracted to the surface at more negative electrode potentials. The presence of adsorbates at the surface may influence the diffracted x-ray signal from the surface, so SXRD can be a useful tool for the investigation of electrochemical adsorption and desorption processes.

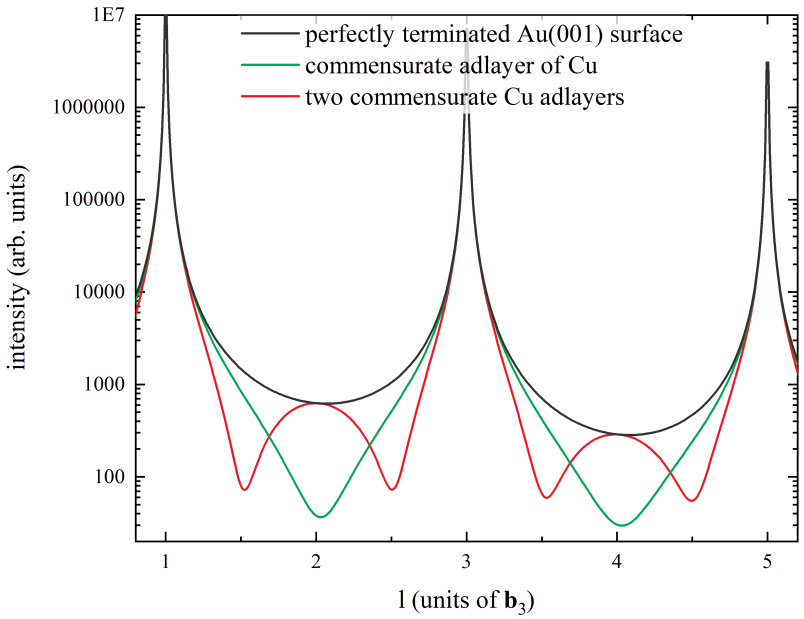

Fig. 2.15 Effect on the $(0,0,l)$ CTR profile from Au(001) of a commensurate Cu adlayer (green) and Cu bilayer (red).

If a species is being adsorbed at an electrode surface, the coverage of adsorbed species will increase. The growth of an adlayer at the surface may perpetuate by different growth modes such as layer-by-layer, island growth or layer plus island growth. The type of growth mode depends on the strength of the bonding between atoms. A stronger substrate-adsorbate bond will result in more layer-by-layer growth: if the bond strength between adsorbate atoms is stronger, islands are more likely to form. Layer-by-layer growth is when monolayers form epitaxially on the surface, as opposed to the nucleation of islands occurring during adsorption or deposition of layers.

Adsorbed species from the electrolyte, or intermediate adsorbates from reactions, have significant influence on electrochemical processes at a surface, such as phase formation during electrodeposition [24–27] and electrocatalytic reactions [28]. The surface stability may also be affected by adsorbates, causing degradation of the electrode surface, as will be demonstrated in Chapter 5.

When adsorbates form a superstructure on the electrode surface that is registered with the bulk, the adlayer is said to be commensurate. Such structures are ordered within the surface plane, therefore affecting the shape of the non-specular CTRs. If adsorbates at the surface form an incommensurate structure, the adsorption may be best modelled as a roughening of the underlying metal layers of the electrode surface. Commensurate adlayers must be included when modelling the surface, and are accounted for by adding a component F_{comm} to

the structure factor (2.40)

$$I_{CTR} = |F_{total}|^2 = \left|F_{bulk} + F_{surface} + F_{comm}\right|^2 \tag{2.46}$$

where $F_{surface}$ is the sum of the scattering contributions from all the surface layers of the electrode and F_{comm} is the sum of the scattering contributions from the commensurate adlayers. For the example of a Cu monolayer on the Au(001) surface [29], where the Cu atoms sit in the hollow sites of the Au(001) surface, the structure factor for the commensurate adlayer is given by

$$F_{comm} = f(q)_{Cu} f_{DWF_{Cu}} \theta_{Cu} \mathrm{e}^{2\pi \mathrm{i} j\left(\frac{h}{2}+\frac{k}{2}+l\left(\frac{1}{2}+\varepsilon_{Cu}\right)\right)_{Cu}} \tag{2.47}$$

where j is the number of the layer, for example for a bulk Au crystal with three Au surface layers, $j = 4$ for this Cu adlayer that sits atop the Au surface layers. The structure factor depends on the form factor specific to the atoms making up the adlayer, as well as the positions of the adatoms, which are described by the phase factor in the expression.

The effect on the shape of the $(1,0,l)$ CTR profile of a commensurate adlayer is shown in Figure 2.15, where a modelled Au(001) surface with adsorbed Cu monolayer sitting in the four-fold hollow sites produces the blue curve and the red curve is produced by modelling a bilayer (two Cu adlayers). The intensity at the anti-Bragg position decreases with a commensurate monolayer, and for a commensurate bilayer, two minima equally spaced between the anti-Bragg and Bragg peaks occur.

When adsorption occurs leading to atoms forming a structure with a different lattice to the underlying crystal, the adsorption is said to be incommensurate. This can include both structures that are ordered or disordered, and both will contribute to the specular surface x-ray diffraction signal.

Underpotential deposition (UPD) is the process where metal ions in solution are deposited on the surface of a different material to form a monolayer of metal ions. UPD occurs at negative potentials that are less negative than the Nernst potential for the metal. The Nernst (or equilibrium) potential is that at which atoms of a metal can deposit onto a substrate of the same metal. UPD occurs when a metal can be deposited onto another material more easily that itself, when the adsorbate-substrate interaction is stronger than the adsorbate-adsorbate interaction. If the potential reaches the Nernst potential, bulk deposition of the metal will occur on the surface. Bulk deposition is when multiple layer growth occurs, rather than single layer. In the case of UPD of Pb on the Cu electrode surface, a monolayer of Pb is deposited on the Cu surface.

Modelling a UPD adlayer can be achieved by including a commensurate adlayer in the calculation of the CTRs. It is necessary to understand the structure of the UPD layer so that the correct phase factor due to the atomic positions in the unit cell can be included in the calculation (2.47).

Surface reconstruction is one of two energetically favourable processes which occur to lower the surface energy and maximise co-ordination of surface atoms, the other being surface relaxation. A surface reconstructs due to the different bonding environment experienced by atoms at the surface compared with bulk atoms. Surface reconstruction is a rearrangement of surface atoms such that the in-plane atomic positions change. Atoms in a reconstructed surface layer will have an altered periodicity and symmetry from that of atoms in bulk layers. The surface can be considered to have a two-dimensional unit cell independent of the bulk unit cell [30] and can be modelled in the same way as an adlayer.

A surface reconstruction or commensurate adlayer structure is described in terms of the relationship between the periodicity of the surface unit cell and the periodicity of the bulk unit cell, by Wood's notation [31]. A surface structure with the same symmetry as the bulk crystal is described by Wood's notation of (1×1). If the unit cell of the surface is twice as large as the unit cell of the bulk along one of the primary unit cell directions then it is described by (2×1) in Wood's notation.

To model the scattered x-ray intensity from a reconstructed surface that is commensurate with the bulk, the structure factor for the reconstructed surface layer (or layers) may be calculated from the atomic positions in the reconstructed unit cell. This is similar to the case of a commensurate adlayer, where the structure factor calculation is given by (2.47).

2.6 X-Ray Voltammetry

X-ray voltammetry (XRV) is a term used to describe a potential scan of an x-ray electrochemical cell, where the dependent variable being investigated is the diffracted x-ray signal rather than the current (which is also recorded during the measurement). This may refer to a scan of the potential from one vertex to another and back again, as in cyclic voltammetry, or a scan in a single direction. In a XRV experiment, the diffraction signal at a single reciprocal space position is monitored as the applied electrode potential is scanned.

It can be illuminating to carry out XRV scans at reciprocal space positions that are sensitive to a particular structure change. For example, XRV at a position on a fractional order rod may reveal the formation and dissolution of superstructure. XRV is a useful tool, as it is a relatively fast technique that can offer insight into structure changes that may be occurring, compared with carrying out a full characterisation of the surface by SXRD.

When investigating a solid-liquid interface, XRV measurements may be carried out as the first step, to check the stability of the surface with respect to changes driven by applied electrode potential. These measurements offer insight into the changes that may be occurring at the surface, which may guide the planning of further SXRD measurements to more fully characterise the surface structure.

The advantage of x-ray voltammetry as a technique is that it can be used to correlate electrochemical reactions and processes that are observable with cyclic voltammetry with changes in the surface structure.

2.7 Summary

In this chapter the fundamental theoretical principles behind electrochemistry and surface x-ray diffraction have been explored. In section 2.2, galvanic electrode reactions were introduced along with theoretical models of the solid liquid interface. This section also discusses mechanisms of adsorption at an electrode surface and the electrochemical technique known as cyclic voltammetry (CV). Throughout this thesis, cyclic voltammetry is employed in combination with x-ray experimental techniques to investigate reactions and processes at metal electrode surfaces, driving and controlling processes at the interface and obtaining structural detail.

Section 2.3 details the theory of surface x-ray diffraction, an experimental technique by which the atomic structure of a metal electrode surface can be determined. The structure of single crystal electrodes is described in Section 2.4, introducing the (111) and (001) *fcc* surfaces that are investigated in this thesis. This section includes detail on the diffraction signal due to electrode surfaces, and Section 2.5 explores how the diffraction signal is modified due to changes in the surface atomic structure. The methods for modelling surface structure based on surface x-ray diffraction results are described for different changes in structure that occur, including adlayer structures that may form. Finally, Section 2.6 provides a description of x-ray voltammetry, a technique used to quickly assess the structural behaviour at an electrode surface with respect to changing electrode potential.

The theoretical principles introduced and explored in this chapter are applied in the experiments described in the subsequent chapters of this thesis.

Chapter 3

Experimental Methods

3.1 Introduction

In this chapter the experimental equipment and methods employed for the research presented in subsequent chapters will be discussed. The methods of preparing the sample, including the single crystal electrode, electrolyte solution and other cell components are detailed in Sections 3.2 to 3.4. The synchrotron radiation facilities at which the experiments were carried out are described in Section 3.5, where the source of x-rays as well as the instrumentation for carrying out a surface x-ray diffraction (SXRD) experiment on a synchrotron beamline is presented. Finally, the methods of performing x-ray scans for an SXRD experiment and of extracting and interpreting the data are described in Section 3.6.

3.2 Sample Preparation and Characterisation

In a single crystal diffraction experiment, it is important to ensure the use of a high quality sample, so that a clear diffraction pattern is obtainable. A high-quality single crystal sample is defined in this case as being atomically well-ordered. These experiments used single crystal samples sourced from MaTecK (MaTecK GmbH, Jülich, Germany), who supplied single crystal samples that were cut along the surface planes with a miscut angle of less than 0.3 °. To perform these fundamental experiments it is necessary to use as close to an ideal single crystal surface as possible. To maintain the sample quality the crystal must be stored securely and handled with care during use.

3.2.1 Surface Annealing

To prepare a Au(001) or Au(111) single crystal surface, the sample surface must undergo annealing. Annealing applies thermal energy to the sample surface, causing movement of the atoms, which upon cooling come to rest in their lowest energy positions. To obtain an atomically well-ordered surface with fewer dislocated atoms, the process is repeated. Multiple cycles of annealing forms a flat, well terminated and well-ordered surface. Depending on the type of surface, the required temperature and conditions for successful annealing may vary.

Gold (111) and (001) single crystal surfaces are suitable for annealing in a butane flame [32, 33]. For metals such as Pt, higher temperatures are necessary for annealing, which may be achieved with a hydrogen flame. In flame annealing, two processes occur which help to achieve a less atomically rough and more pure surface: Firstly, the flame acts to burn off impurities present at the surface by evaporation, and secondly, the flame applies thermal energy, allowing metal atoms to move more freely and be deposited at their most energetically favourable locations. For some metals, such as Ag (which is more reactive than Au), it is necessary to anneal the crystal in an ultra-high vacuum (UHV) environment to avoid oxidation of the surface. UHV annealing is carried out by induction, and coupled with sputtering, which refers to the process of bombarding the sample surface with high energy gas particles in UHV with the aim of ejecting material from the surface [34].

Flame annealing for experimental preparation during this research was carried out on a lab workbench by placing a crystal sample on a ceramic heating plate and gently heating with a butane blow torch until the surface glowed orange. A photo of Au single crystal surface undergoing flame annealing is presented in Figure 3.1, taken prior during sample preparation for an experiment that is reported in Chapter 4. Care must be taken so as not to melt the bulk single crystal while the surface is kept at this temperature for a few seconds. Then the crystal is allowed to cool slightly before the process is repeated ten times. Once the surface has been annealed, the crystal is slowly cooled before being covered with a drop of ultrapure deionised (DI) water to protect the surface before being transferred into an electrochemical environment to carry out the experiment.

DI water used during these experiments was provided via an Elga purification system with a resistivity of 18.2 MΩ·cm.

3.2.2 Electrochemical Etching

For these experiments, Cu single crystal samples were also reprepared in laboratory conditions between experiments, rather than by UHV sputtering and annealing. Cu samples were reprepared by electrochemical etching (also known as electropolishing). The surface is

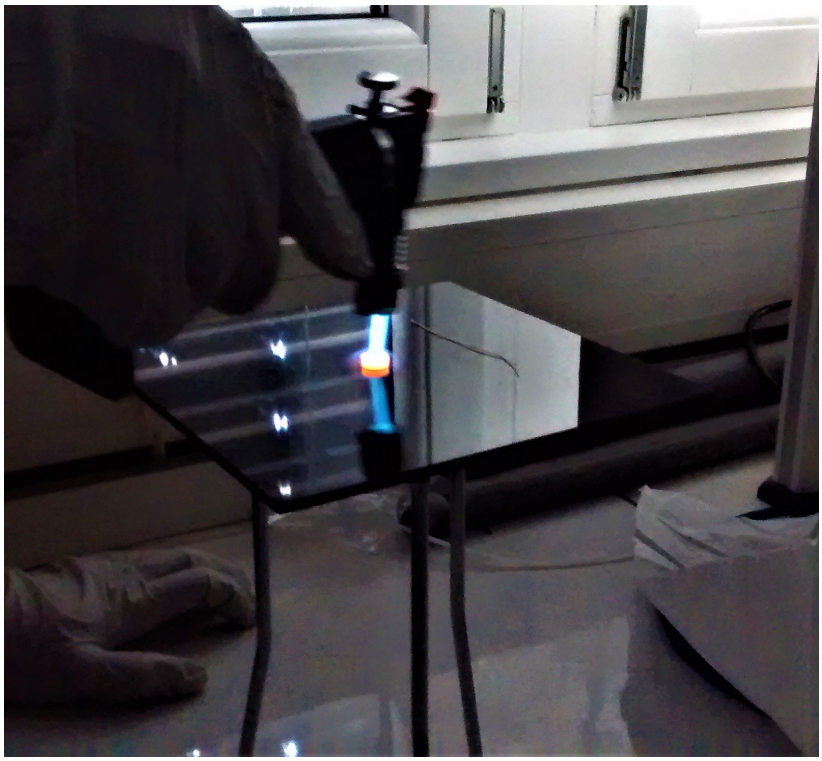

Fig. 3.1 Flame annealing of a gold single crystal surface with a butane flame

submerged in 70 % phosphoric acid (H_3PO_4). A counter electrode with a high surface area is used (a Cu mesh) to apply 2V to the surface for 10 s using a power supply. The process repeated as required until a well-ordered surface is attained.

During the electropolishing process, Cu atoms are stripped from the surface, monolayer by monolayer. This achieves an atomically smooth and well-ordered surface by removing the rougher surface layers of atoms. The surface layers may also be oxidised prior to electropolishing, as Cu is a reactive surface and oxidises easily in ambient conditions, and electrochemical etching removes layers of oxide. The importance of the particular procedure that is followed during Cu surface preparation is discussed in Chapter 5, as it was found that different methods of transferring the sample into the electrochemical environment resulted in a difference in the quality of the sample surface.

3.3 Cleaning of Electrochemical Equipment

When studying a specific electrochemical system it is important to eliminate any contamination from the environment, to ensure that effects and changes that are observed are due to the interactions and processes we intended to study. Contamination must be eliminated

from every component of the system, the electrolyte solution, the electrodes and the vessel in which the cell is held. In order to eliminate contamination as effectively as possible, the equipment is cleaned thoroughly before every experiment.

The x-ray electrochemical cell used for these SXRD experiments was designed such that every component could be thoroughly cleaned prior to each assembly. Every component that would be in contact with the electrolyte solution, and all glassware and equipment used in making the electrolyte solution, was chosen due to being acid-resistant, so that it could be cleaned using concentrated acid.

A mix of sulfuric and nitric acids is used for acid cleaning, as this is suitable for breaking down metal particles, traces of which may be left over in the system from previous electrochemistry experiments.

Typically, glassware is soaked in concentrated acid for up to 24 hours before being thoroughly rinsed with DI water. Glassware is boiled in DI water on a heating plate and rinsed. This process is repeated until the equipment is clean. Equipment that is not heat-resistant is rinsed repeatedly in DI water, as well as being cleaned by sonication in an ultrasonic bath, after being soaked in acid to ensure any contaminants are washed away.

3.4 The Electrochemical Cell

A three-electrode electrochemical cell consists of a working electrode, counter electrode and reference electrode separated by the conducting electrolyte in solution. The electrochemical experiment is controlled via a potentiostat. For an in-situ surface x-ray diffraction experiment that investigates the electrode surface during electrochemical processes, a purpose-built cell that facilitates x-ray measurements is employed.

3.4.1 Potentiostat

A potentiostat is an electronic device that, in a three electrode setup, is used to apply a potential between two electrodes: the working electrode and the counter electrodes. This causes a current to flow through a conducting media (the electrolyte) and the voltage drop at the working electrode is measured with respect to a third electrode, known as the reference electrode [35]. A circuit diagram of a potentiostat is shown in Figure 3.2. A potentiostat is used to conduct electrochemical experiments and allows the measurement of cyclic voltammograms, where the current that flowing is plotted as a function of potential between the working and reference electrodes. The potential difference between the working and reference electrodes is monitored by the potentiostat while the potential is applied through

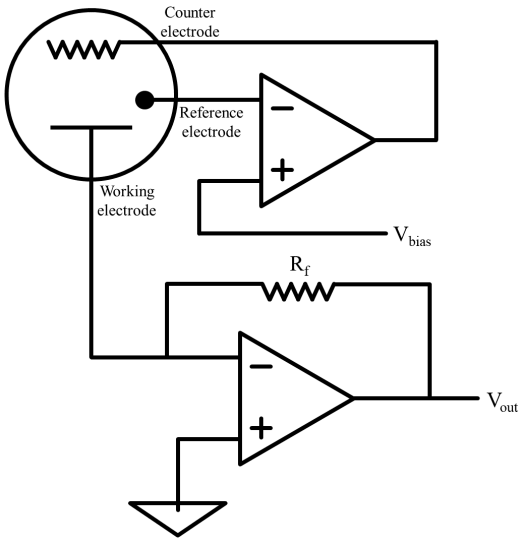

Fig. 3.2 Circuit diagram of a potentiostat

the counter electrode to drive a current that is measured across an in-series resistor. The flow of electrons across the solid-liquid interface is directly measured by such a measurement of current in the electrochemical cell.

These experiments were carried out with a Princeton Applied Research Versastat II, Versastat 4 or an Ivium Technologies CompactStat, depending on the synchrotron beamline that the experiment was carried out at. The potentiostat is connected to a control system and user interface. Using a potentiostat to run voltammetry and control the potential on a synchrotron beamline allows us to make potential dependent x-ray diffraction measurements of an electrochemical sample.

3.4.2 The X-Ray Electrochemical Thin Layer Cell

The electrochemical cell used in a surface x-ray diffraction experiment needs to facilitate the incidence of x-rays on the investigated surface as well as the detection of outgoing x-rays. The configuration used in these experiments was that of a 'thin-layer' cell, where the distance the x-rays travel through liquid is minimised, to minimise attenuation. The design is that of an open circular cell vessel, with the single crystal working electrode at the centre, its surface facing upwards, and a reservoir of electrolyte solution around the outside. A schematic of the cell is shown in Figure 3.3. A thin layer of electrolyte solution sits on the electrode surface, and a polycrystalline wire counter electrode curls around the inside edge of the cell vessel. A Ag/AgCl reference electrode, also sits at the inside edge of the cell vessel, which is filled, like a bowl, with electrolyte solution. A hydrophilic polypropylene film, transparent to x-rays, is

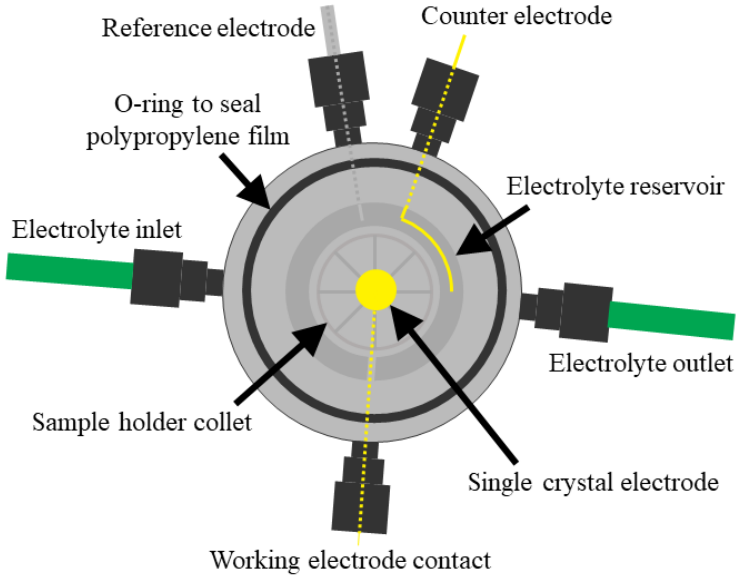

Fig. 3.3 Schematic of the x-ray electrochemical thin layer cell

held in place over the open vessel to seal the cell and reducing the pressure of electrolyte solution in the cell pulls the film down leaving only a thin layer of electrolyte solution on the working electrode surface. The polypropylene films are manufactured by Chemplex (SpectroMembrane® Thin-Film Sample Support Window Frames - Chemplex Industries Inc., Palm City, Florida, USA) and are hydrophobic as standard but become hydrophilic after being boiled in water.

On either side of the cell sit an inlet and outlet, drilled into the PCTFE cell vessel, to which PTFE tubing is connected to allow the flow of electrolyte solution into and out of the cell reservoir. The reference and counter electrodes pass through two other holes drilled into the cell, so that connections can be made from the electrode wires to the potentiostat. The single crystal working electrode is connected to the potentiostat by a polycrystalline wire, coiled to form a good connection to the bottom side of the crystal as it sits on top in the centre of the cell. This back-contact wire passes through a PCTFE channel in the cell, so as not to be in contact with the electrolyte solution, and out through a fifth hole drilled into the cell. The cell is surrounded by a Kapton film hood, which is transparent to x-rays, held by an aluminium frame. This hood is filled by an over-pressure of inert gas such as nitrogen or argon.

A photo of the x-ray cell, mounted during an x-ray diffraction experiment, is shown in Figure 3.4. The cell can be seen through the orange-coloured Kapton film window in the hood, which is transparent to the incident and outgoing x-rays. The black o-ring that holds the polypropylene film in place is most clearly visible through the hood, with a Cu(001)

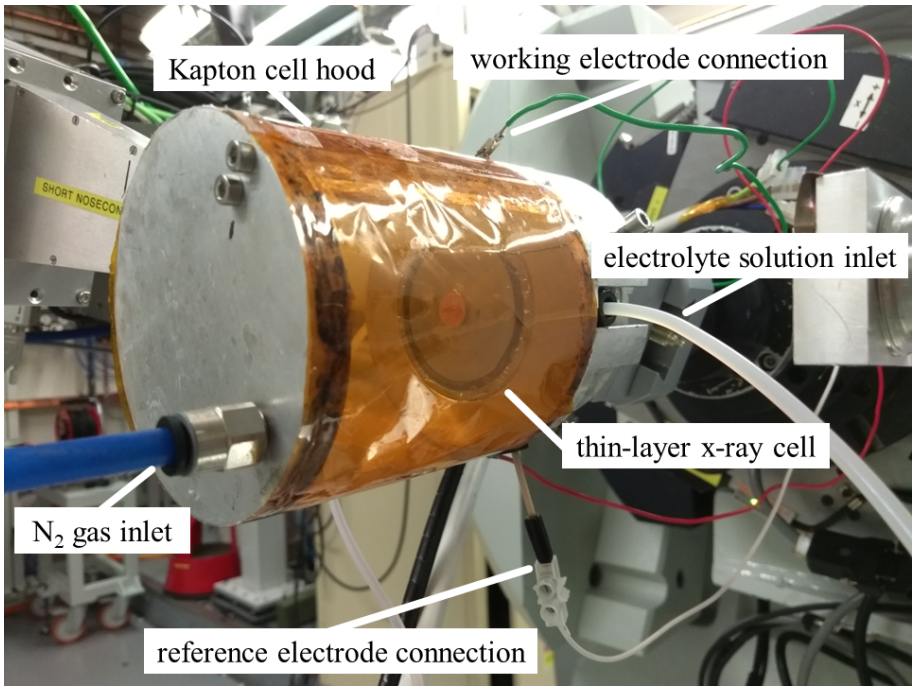

Fig. 3.4 The x-ray electrochemical cell, mounted on the I16 beamline at Diamond Light Source

single crystal more difficult to make out, held in the centre of the cell vessel by a sample holder collet. Connections to the cell can be seen around the baseplate of the cell, along with clear plastic tubing to facilitate the flow of electrolyte solution. The inlet for blue tubing visible on the roof of the hood allows the intake of N_2 gas.

The flow of electrolyte solution into and out of the cell is controlled with a syringe connected to the cell outlet, allowing fresh electrolyte solution to be pulled through the system into the cell from a reservoir flask. Electrolyte solution is purged in the reservoir flask with inert gas before transfer to the cell. The syringe can be used to adjust the amount of electrolyte solution in the cell, deflating the polypropylene film to form a thin layer for x-ray measurements or inflating the film, so that electrolyte solution forms a bulk liquid on the single crustal surface, which is useful for electrochemical conditioning of the surface between x-ray measurements as the cell acts more like a standard electrochemical cell.

Electrolyte solutions were prepared using the wet chemistry laboratories available at the synchrotron facilities where the experiments were carried out. Ultrapure DI water was used along with chemical reagents sourced from Merck (previously Sigma Aldrich - Merck KGaA, Darmstadt, Germany) and Fisher (Fisher Scientific UK Ltd., Loughborough, UK). Different electrolyte solutions, specific to the experiment, were prepared using precise lab scales and volumetric flasks to measure the reagents.

3.5 Synchrotron Facilities

A single crystal surface x-ray diffraction experiment requires the ability to resolve the surface diffracted signal from the diffuse bulk scattering background. As the surface contribution to the scattering is ~ 10^{-5} of the bulk crystal contribution, this resolution requires sufficient counting statistics. The x-rays probing the surface also have to pass through the liquid electrolyte layer, which attenuates the intensity of the beam. This means that a high intensity x-ray source is required for SXRD experiments to be efficiently conducted, such as a synchrotron radiation source.

3.5.1 Synchrotron Radiation

Synchrotron radiation was originally discovered as an unwanted by-product of particle acceleration, arising due to the conservation of momentum when charged particles travel in a curved path at relativistic speeds [36, 37]. When electrons or positrons travel in a beam around a cyclic particle accelerator, the particles experience acceleration perpendicular to their direction of travel. To satisfy the conservation of momentum, photons are emitted as a relativistic particle changes direction.

The energy of the emitted photons is dependent on the amount of kinetic energy lost by the relativistic particles as they turn within the cyclic accelerator. Within a synchrotron (a type of cyclic particle accelerator), electrons or positrons circle in a closed loop, directed by magnetic fields. Synchrotrons are commonly used today as sources of photons within the x-ray band of the energy spectrum, as x-rays are sought-after for experimental research in a wide range of scientific disciplines. A synchrotron light source is a synchrotron that has been set up with the aim of providing useful synchrotron radiation.

The cyclic particle accelerator within which the particle beam continuously circles is known as a storage ring, designed to store particles at a constant energy. The energy lost by the beam through synchrotron radiation is topped up by the use of radio-frequency cavities. The high energy beam is directed into bending magnets and insertion devices (undulators and wigglers) which induce the changes in direction that produce synchrotron radiation via strong magnetic fields. Insertion devices bend the particle beam into sinusoidal or helical paths, with the aim of maximising the number of photons produced. A large number of charged particles circle in the storage ring, to produce high intensity beams of synchrotron radiation (x-rays) at each insertion device and bending magnet.

Modern third-generation synchrotron light sources were designed with the aim of producing brilliant x-rays, and contain many insertion devices. Brilliance is a common quantity used

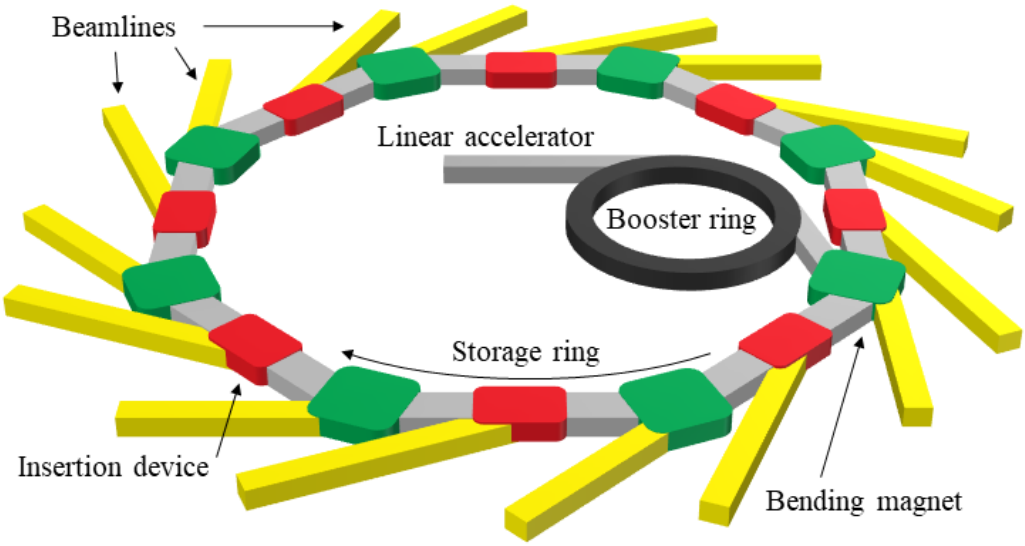

Fig. 3.5 Schematic diagram of a 3rd generation synchrotron

to compare different synchrotron x-ray sources. It is a function of the intensity of photons produced, the angular divergence of the photons, the cross-sectional area of the beam and the number of photons that have a wavelength within 0.1 % of the central wavelength of the source. A synchrotron with a higher brilliance produces more photons of a given wavelength and direction at a particular position per second. A modern third-generation synchrotron light source has a brilliance of more than 10^{18} photons·s^{-1}·mm^{-2}·mrad^{-2}/0.1%BW, where 0.1%BW denotes a bandwidth $10^{-3}w$ centred around the frequency w.

Surface x-ray diffraction experiments were carried out as part of the research described in subsequent chapters at synchrotron light source facilities in the UK and France. Diamond Light Source (DLS) is the UK's national synchrotron facility, with 3 GeV electron beam and is located in Harwell, Oxfordshire. Diamond has 32 beamlines that specialise in different scientific disciplines and techniques, situated around the 562 m-circumference storage ring. Experiments were also carried out at the European Synchrotron Radiation Facility (ESRF) in Grenoble, France, a third generation light source with a circumference of 844 m run in collaboration by 22 countries. The ESRF boasted 44 beamlines prior to 2020, when it was shut down in preparation for its upgrade to the current ESRF-EBS (Extremely Brilliant Source). The electron beams of both the ESRF and current ESRF-EBS have an energy of 6 GeV.

A schematic diagram showing a third generation synchrotron light source, based on Diamond, is shown in Figure 3.5. The storage ring is made up of linear accelerators (linacs, shown in grey) and bending magnets (shown in green), in which the electron beam circles,

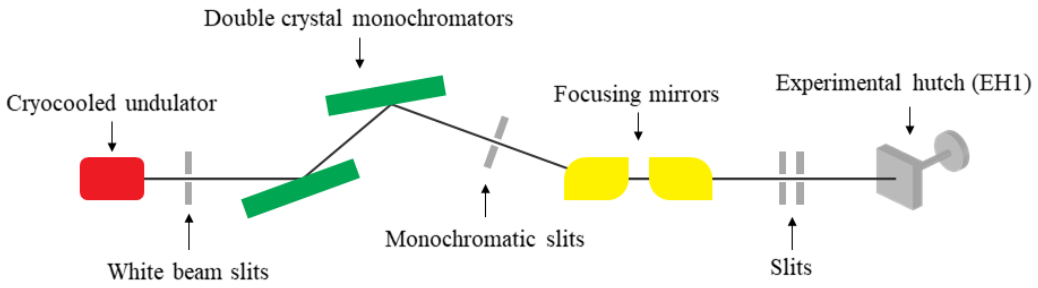

Fig. 3.6 The beamline optics at I07, Diamond Light Source

emitting synchrotron radiation along the beamlines (yellow paths). Beamlines are situated at bending magnets and insertion devices (shown in red). The electrons that circulate in the storage ring are injected into the linear accelerator in the centre of the storage ring by an electron gun. In Diamond, this linac receives electrons with an energy of 90 keV and accelerates the particles up to 100 MeV. A smaller cyclic accelerator, the booster ring (158 m in circumference, shown in black) accelerates electrons from 100 MeV up to the 3 GeV energy of the storage ring beam.

A bending magnet is used to change the direction of the particle beam in the storage ring. Rather than being circular, a storage ring is typically made up of straight, linear accelerators arranged in a ring, with bending magnets situated in between each one. Bending magnets use strong magnetic fields to curve the beam around each corner. The XMaS beamline at the ESRF (used to carry out surface x-ray diffraction experiments described in subsequent chapters) is located at a bending magnet. The change in direction of the electron beam at this point produces the beamline's x-ray source.

Experiments were also carried out using the I07 and I16 beamlines at Diamond Light Source, which are situated at insertion devices rather than bending magnets. Insertion devices are located within the linear accelerator sections of the storage ring, where undulators or wigglers are added to produce photons. At a bending magnet or insertion device, a fan of synchrotron radiation is funnelled into a beamline. Modern synchrotrons have a number of beamlines around the outside of the storage ring, and these are where the synchrotron radiation is put to use for a wide range of applications, including surface x-ray diffraction (SXRD).

3.5.2 Beamline and Diffractometer

When a fan of synchrotron radiation is produced at a beamline, the white beam, so called as it contains light of a range of wavelengths, is passed through a series of optics to prepare the x-ray beam for experimental use. Figure 3.6 shows a diagram of the I07 beamline optics

at Diamond. I07[38], where the data in Chapter 5 and 4 were measured, is located on a straight section of the Diamond storage ring, where the insertion device is an undulator. Slits, collimators, monochromators and focusing mirrors are housed in I07's optics hutch, where the optics may be altered to suit the experiment and the needs of the users. Different beamlines cater to different users, offering their own range of techniques and sample stages.

In the optics hutch, the white beam passes through slits before reaching a double crystal monochromator, which uses Si(111) crystals to control the energy of the outgoing beam, allowing the desired x-ray wavelength to be selected. The resultant beam of x-rays passes through another set of slits before being focused in the vertical and horizontal directions by two bimorph mirrors. This allows the beam size to be adjusted. Therefore, the x-ray beam can be tailored to a variety of experiments, in terms of the 2D beam size and the x-ray energy. After entering the first experimental hutch (EH1, I07 has two), the beam can be conditioned by a series of slits and attenuators, as well as beam-position monitors and an ADC ion-chamber, which allows the incident beam intensity to be monitored and offers the ability to normalise intensity measurements. The use of fast shutters means that the sample is only exposed to the beam when a measurement is being made. For some electrochemical systems, continuous beam exposure can reduce the lifetime of the sample, with free radicals formed in the electrolyte solution causing the polypropylene film to split, which requires re-preparation of the sample.

To carry out a SXRD experiment, one needs a source of incident x-rays, a detector for outgoing diffracted x-rays and a method of controlling the angles of incident and outgoing x-rays relative to the sample surface. The x-ray source at I07 has been discussed, and the majority of data presented in this work was acquired using a Pilatus 100K 2D detector [39] (DECTRIS Ltd., Baden-Daettwil, Switzerland). To control the incident and outgoing angles of x-rays relative to the surface, the experiment is conducted with a diffractometer. EH1 at I07 houses a Huber (2+3)-circle diffractometer [40], which allows the SXRD experiment to be carried out in horizontal or vertical geometry. The diffractometer is operated in (2+2)-circle mode, by defining the experimental geometry with two sample angles and two detector angles. A diagram showing a (2+2)-circle diffractometer set up in vertical geometry mode is presented in Figure 3.7a, with the experimental angles indicated. In vertical mode, the angle of incidence for the sample surface is α and the azimuth is ω. In horizontal mode the angle of incidence is χ and the azimuth is θ, as shown in Figure 3.7b. The detector may move independently of the sample by movement of the detector arm through two detector angles, δ and γ, which move the arm vertically and horizontally respectively. Detector slits are located between the sample and the detector, which are used to reduce the signal-to-noise ratio of the detected signal. The centre of rotation for the diffractometer is the centre of the

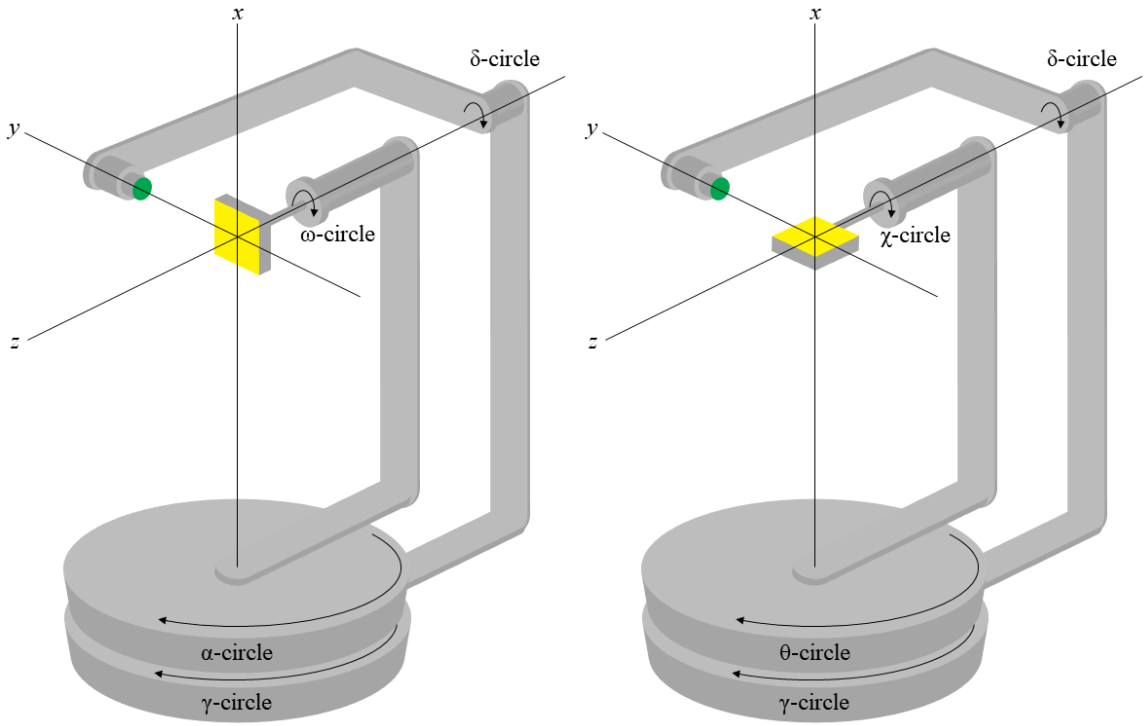

(a) (b)

Fig. 3.7 Diagrams of a (2+2)-circle diffractometer in (a) vertical and (b) horizontal geometry operating modes. The sample surface is represented by the yellow square while the green circle represents the detector

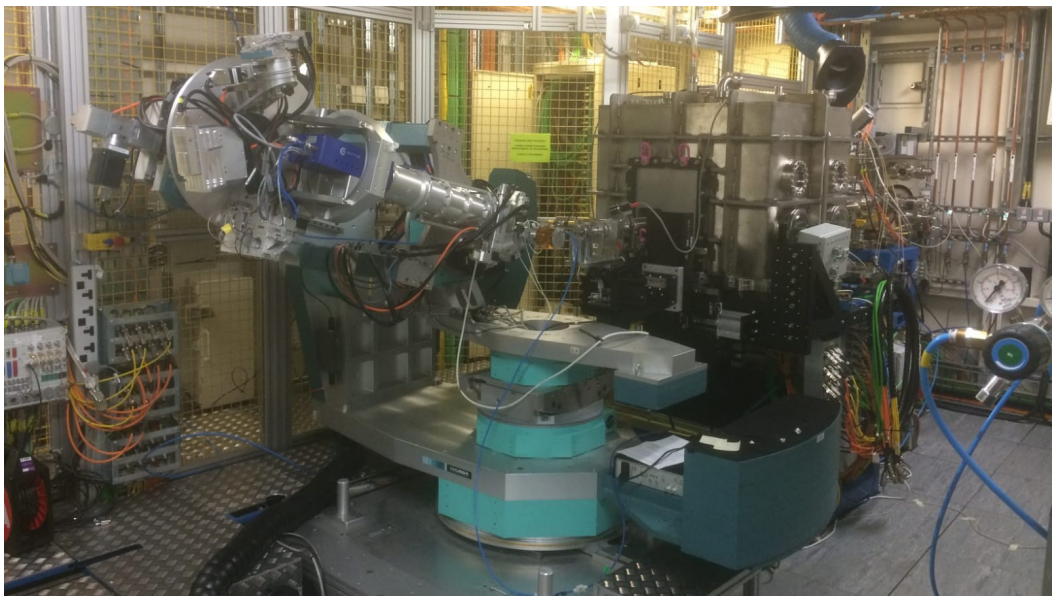

Fig. 3.8 The diffractometer housed in EH1 at I07, Diamond Light Source

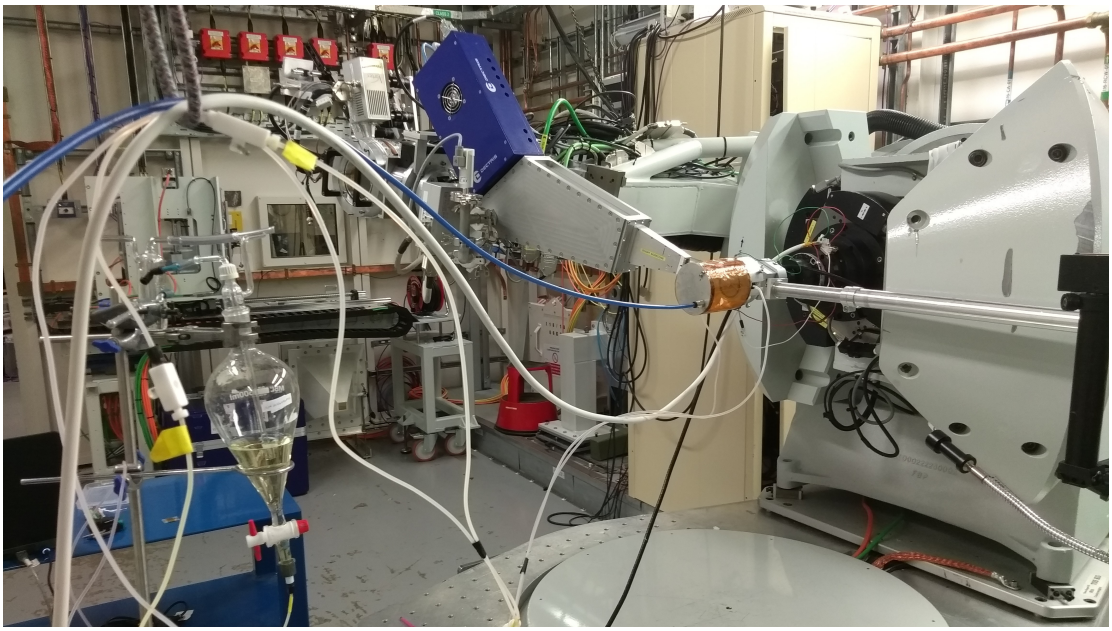

Fig. 3.9 The experimental setup on the I16 beamline, Diamond Light Source.

sample surface, which, at I07, sits on a hexapod, allowing the sample's position to be altered translationally. A photo of the diffractometer in EH1 at I07 is shown in Figure 3.8, where the diffractometer is being operated in vertical geometry mode.

Measurements were also made at the I16 beamline at Diamond Light Source (Chapter 6) and the XMaS beamline, BM28 at the ESRF (Chapter 6) where the setup of the beamline is slightly different to I07, but the principle is the same. I16 [41] is an insertion device beamline, situated at an undulator, and a key difference in the beamline optics from I07 is the diamond phase retarder [42] which allows the polarisation of the x-rays to be controlled. This is useful for resonant surface x-ray diffraction measurements, as measurements with different polarisation can be made without having to switch between vertical and horizontal scattering geometries with the diffractometer. The experimental hutch at I16 houses a six-circle kappa diffractometer, which feature more diffractometer angles than that shown in Figure 3.7. This, and the Huber diffractometer on the XMaS beamline [43], which was also operated in six-circle mode, are set up to allow control of the same two sample and two detector angles that were employed in experiments at I07.

An image of the experimental hutch interior at I16 is shown in Figure 3.9, with the x-ray cell sample visible mounted on the diffractometer to the centre-right of the picture, operating in vertical geometry. The incident x-ray beam enters through the pipe seen on the right-hand side of the photo, and the blue housing of the 2D detector is clear towards the top, in the centre of the image. A reservoir containing electrolyte can be seen to the left of the image,

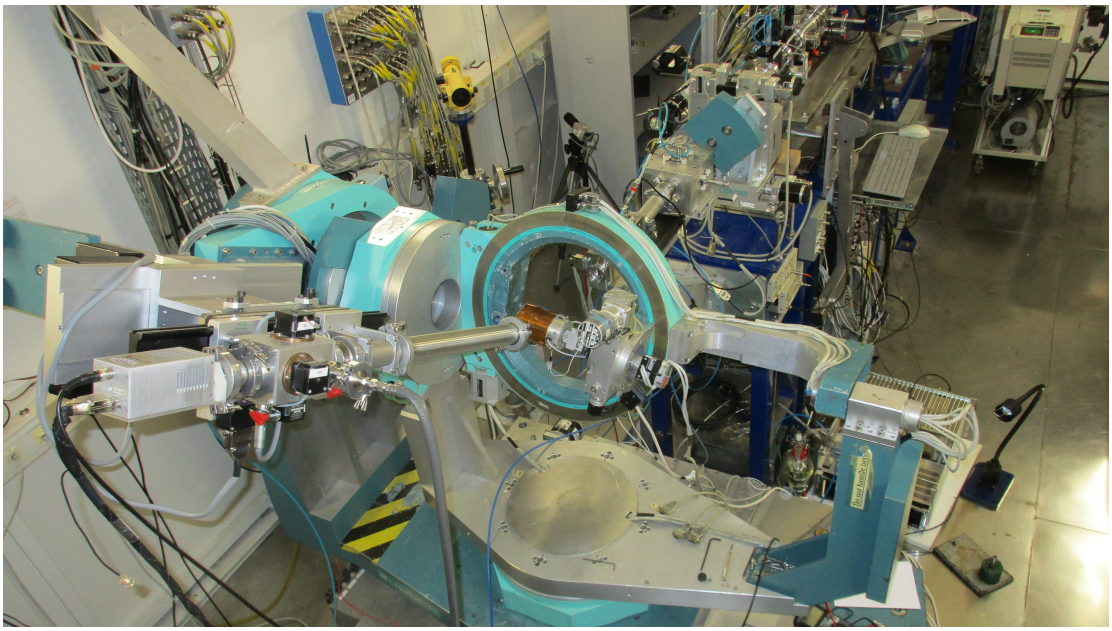

Fig. 3.10 The experimental setup on the XMaS beamline, BM28 at the ESRF.

with clear electrolyte tubing and a blue tube carrying N_2 gas leading from the left of the picture to the x-ray cell.

Data measured at XMaS was not acquired with a 2D detector, such as the Pilatus 100K used at I07 and I16, but by a point detector with a multichannel analyser, which offers energy resolution of the detected x-rays. A photo of the experimental setup at XMaS is shown in Figure 3.10. The point detector is visible in the foreground, to the left, the x-ray electrochemical cell is in the centre, mounted on the diffractometer. The incident beam can be seen entering from the top of the field of view. The sample is mounted in vertical geometry in this photo, which was taken during an experiment reported in Chapter 6.

3.5.3 Sample Alignment

To measure diffraction from a sample surface with a diffractometer it is important to align the single crystal surface with the instrument. The cell is mounted on the diffractometer as all angles are set to zero with the surface as flat as possible, but due to the precision of the measurement, the alignment has to be checked with x-rays. The hexapod moves the sample in the x, y and z directions translationally, as well as allowing rotation around these axes. The sample is adjusted so that it is at the correct height to cut the beam intensity in half when diffractometer angles are zero. By moving the sample up in z to block the beam, and moving along the x and y axes, the sample is precisely centred on the diffractometer. The sample can also be rotated to check how flat the surface is. Once the positioning of the sample is

as centred and flat as possible, a specular Bragg reflection $((0,0,l)$ is found by moving the sample and detector.

The diffractometer is controlled by a computer system which, using a UB matrix calculation, allows the experiment to be conducted in reciprocal space in terms of *hkl* co-ordinates [44]. There are two components to the UB matrix, the unit cell of the crystal and the positions of two Bragg reflections in terms of the detector geometry. By defining two reciprocal space positions in terms of the positions of diffractometer angle motors, the motor positions for any other position in reciprocal space may be calculated. The specular reflection is used to find two sharper Bragg reflections, that will allow the alignment to be set precisely enough for the measurement of surface x-ray diffraction.

3.6 Scans and Data Extraction

The user interface for beamline measurements is GDA or SPEC (for Diamond Light Source and the ESRF respectively) and it is through this system that diffractometer movements and detector counts are controlled. A scan may be carried out by either specifying a start and end point for motors as well as scan rate and exposure time or by specifying a scan size (distance for the motors to move) and running a centred scan either side of the current position. As well as scanning diffractometer motors, potentiostat scans may be run via the control system, where the potential is set or scanned in the same way as a motor and the current may be measured.

With a 2D detector, an image is recorded for each detector count and pixel regions within the image may be defined to represent the peak signal and the surrounding pixels which record background signal. To extract data, these images are processed using a MATLAB program [45], where background signal may be subtracted from the peak signal in order to calculate the signal intensity. Background correction and standard instrumental corrections are applied to the dataset so that an intensity distribution may be modelled [46, 47]. The data may also be normalised using measurements from an ion chamber in the beamline optics, used as monitor to account for changes in the incident x-ray flux. Errors on the individual data points may be determined by a combination of the statistical error and an estimated 10 % systematic error. This statistical error is based on the Poisson distribution counting statistics associated with the detection of x-rays and the 10 % error is typical for measuring symmetry equivalent positions, from previous SXRD experiments [48, 49]. The error is based on the ratio of sample size to beam size, which is typically around 10 to 50 % (for a 0.5 mm diameter beam and 10 mm diameter sample) and is applicable except for in the case of very small incident angle, α (or χ in horizontal geometry).

3.6.1 Rocking Scans

A synchrotron beamline experiment allows the user to input a set of reciprocal space co-ordinates, such as an anti-Bragg position on a CTR, and measure the diffracted intensity from that position. A useful method of measuring this intensity is a rocking scan, which involves recording the intensity with the detector stationary while the sample is rocked through the azimuthal angle. The resulting profile gives important information about the surface. A more well-defined peak at the anti-Bragg position indicates a better quality surface, in terms of the termination of the single crystal and roughness. When a new sample has been prepared and the first measurement of the surface is made after alignment of the sample, this rocking scan at an anti-Bragg position indicates whether the sample preparation was successful and if the surface is smooth (well-ordered and atomically flat) enough for the SXRD experiment to go ahead or whether the sample must be re-prepared.

The peak area and peak width of rocking scans can be compared to give an idea of changes occurring at the surface. Rocking scans are measured regularly during the experiment, for example when carrying out x-ray voltammetry (XRV) scans, a rocking scan is recorded before and after the scan. This allows the stability of the surface to be monitored, and changes in the surface structure can be tracked throughout the experiment.

Rocking scans are also carried out to measure profiles of CTRs or fractional order rods, by recording rocking scans at l-positions at intervals along the rod. The peaks may be fitted to give intensity values for each position so that the CTR profile can be constructed.

3.6.2 Geometric Correction Factors

The measured intensity in a SXRD experiment depends on a number of factors that have to be taken into account when modelling the data. This is done by calculating the necessary correction factors by which the intensity must be multiplied. These correction factors are dependent on the diffractometer angles and geometry of the experiment. The factors will differ for different diffractometer geometries, therefore the calculations for (2+3) circle [40] and six-circle [50] geometries must be applied depending on the geometry used for the experiment. For measurements at I16, the correction factors are those for a six-circle diffractometer, as the kappa diffractometer was employed in six-c, fixed-α mode.

For rocking scans, the Lorentz factor must be calculated to account for the factor that the scan is measured with angular dependence rather than dependence on a reciprocal space dimension and therefore the intensity is integrated over an angle. For a rocking scan measured

in (2+3) circle geometry the Lorentz factor is given by

$$L = \frac{1}{\sin\delta \cdot \cos\gamma} \tag{3.1}$$

and in the six-circle case:

$$L = \frac{1}{\sin\delta \cdot cos\alpha \cdot cos\gamma} \tag{3.2}$$

The detected intensity also depends on the polarisation of the beam. The vertical polarisation of synchrotron x-rays is assumed to be negligible and the horizontal component of the polarisation is given by the detector angles:

$$P = 1 - \sin^2\delta \cdot \cos^2\gamma \tag{3.3}$$

Corrections must also be made for the detector interception with the diffraction rod. If the plane of the detector is perpendicular to the rod, then the shape of the interception the detector makes will be circular, but if the detector makes another angle with the rod the shape of interception will be an elliptical. The rod interception correction factor is given by

$$R = \cos\gamma \tag{3.4}$$

Another correction factor to be applied is the active area correction, which accounts for the overlap in the areas of the sample that are illuminated by the beam and seen by the detector. This active area is that which contributes to the measured intensity, and it depends on the detector angle δ

$$A = \frac{1}{\sin\delta} \tag{3.5}$$

The low angle area correction is also applied, which, for the six-circle geometry, depends on the sine of the incident angle and the area of the beam footprint compared to the sample surface area, b

$$a = b \cdot \sin\alpha \tag{3.6}$$

The correction factors are applied so that the corrected integrated intensity $I_{corrected}$ for a rocking scan is calculated from the measured intensity $I_{measured}$ by

$$I_{corrected} = \frac{I_{measured}}{LRPA \cdot a} \tag{3.7}$$

3.6.3 Data Analysis

The method of analysis varied between experiments, and specific information is provided in each of the following chapters. In general, for experiments at I16 and I07, 2D detector image data was obtained for the x-ray diffraction experiments, which was processed via MATLAB programming [45]. Extracting CTR data using MATLAB image processing allowed the data to be inspected and modelled. For RSXRD the data extracted with MATLAB was loaded directly into OriginPro for further analysis [51]. All graphs presented in this work were plotted using OriginPro.

When modelling CTR data, the CTR profiles are extracted and compared with a calculation of CTR intensities. The calculation of CTR data is based on the theory outline in Chapter 2. The model of x-ray diffraction is obtained using a Python (Python Software Foundation, Beaverton, OR, USA) program and the integrated lmfit least-square fitting routine, which can be used to obtain best fit parameters for the model, such as expansion (relaxation), atomic layer coverages, Debye-Waller roughness factors or β roughness factors. The fitting is carried out by minimising a χ^2 value given by

$$\chi^2 = \sum \frac{(M-T)^2}{\sigma^2} \tag{3.8}$$

where M represents measured values, T represents theoretical values and σ represents the variance of the data. Taking into account the number of degrees of freedom gives the reduced χ^2 which is quoted for results in the following chapters.

3.7 Summary

In this chapter, the experimental techniques and methods employed in this thesis have been described. Section 3.2 details the preparation procedure for the single crystal electrode samples and Section 3.3 describes the method followed to ensure that the equipment for carrying out electrochemical studies was clean and free from contamination. The electrochemical cell used to perform in-situ surface x-ray diffraction measurements of the electrode surface in electrolyte solution was introduced in Section 3.4. The x-ray experiments were carried out

using synchrotron radiation, of which an explanation is given in Section 3.5 along with details of the facilities used. Experiments were performed at a number of synchrotron beamlines, and a description of each is provided along with information on the procedures followed at each. Finally, a description of the data collection, extraction and general analysis methods is offered in Section 3.6. Along with specific detail given in the following chapters, this chapter has provided a description of the experimental techniques and methods used to obtain the results of this thesis.

Chapter 4

The Hexagonal Reconstruction of Gold

4.1 Introduction

Au is considered an important metal in catalysis for CO (carbon monoxide) oxidation, which is a process most commonly employed for decreasing vehicle emissions of the toxic CO produced in combustion [52]. Catalysis is the process of increasing the rate of a chemical reaction by the introduction of a catalyst, a substance which is not consumed during the reaction. In the context of electrochemical CO oxidation in the presence of Au, the rate of the CO oxidation half-reaction is increased due to the presence of the heterogeneous catalyst, Au. Au has been studied as a catalyst in the form of Au nanoparticles [53, 54], where a high activity was achieved for the oxidation process. High activities for Au as a catalyst for CO oxidation have been reported in alkaline aqueous solutions [55] and electrochemical studies have shown gold electrodes to exhibit the highest activity for CO oxidation in comparison with other electrode materials such as Pt [56–60]. Studies have shown that CO, irreversibly adsorbed on the Au surface in aqueous alkaline electrolyte can promote the electro-oxidation of alcohols, which is an important process for the obtaining a range of organic products. The onset potential for the oxidation of methanol is lowered in comparison to the clean Au surface. This enhancement of electrocatalytic activity is only observed on Au surfaces that reconstruct into hexagonal structures, Au(111) and Au(001) [61–65].

The low index surfaces of gold (Au) single crystals exhibit surface reconstruction [66], a change in the surface structure such that the surface atomic layer has a different symmetry to that of the bulk crystal (Section 2.5.1). The reconstructions of the Au(111) and Au(001) surfaces are both hexagonal, where the surface density is increased by 4 % and 20 % respectively. Au(110) undergoes a missing row reconstruction which is not hexagonal, and unlike Au(111) and Au(001), exhibits no enhanced catalytic activity [2, 67, 68]. For the Au(111) surface, the surface atomic layer is compressed along the $[1\ 0\ 0]$ direction forming a structure

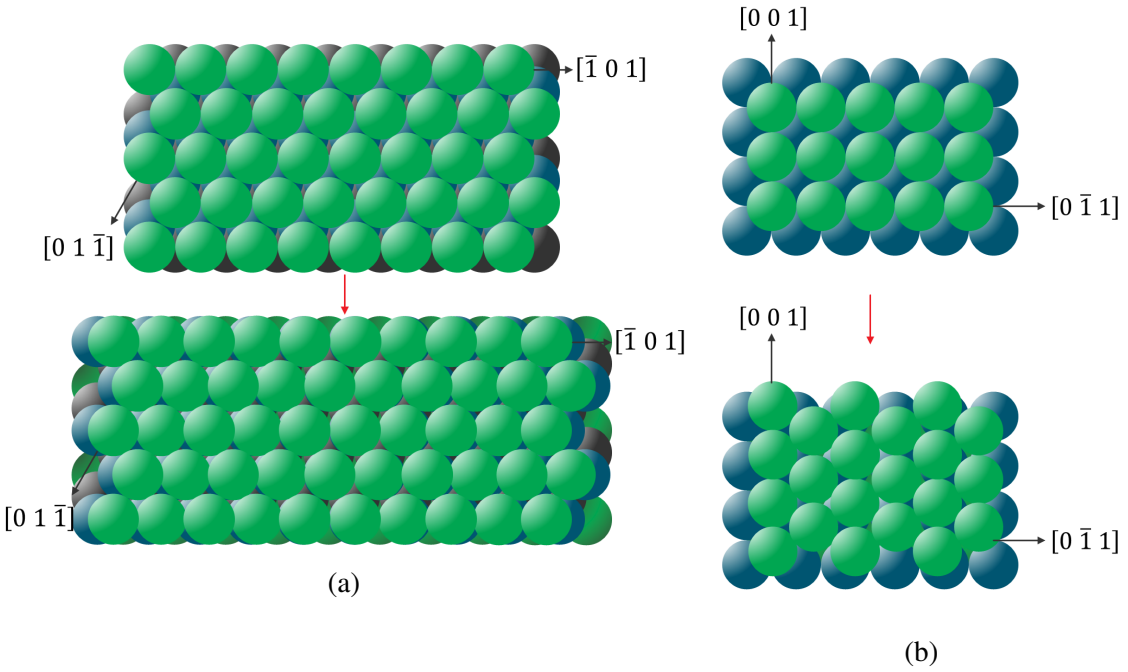

Fig. 4.1 Schematics showing (a) the hexagonal reconstruction exhibited by the Au(111) surface with $(23 \times \sqrt{3})$ periodicity and (b) the ”5×20” or "hex" reconstruction exhibited by the Au(001) surface.

with $(23 \times \sqrt{3})$ periodicity [67, 69]. This is referred to as the ’herringbone’ reconstruction. The hexagonal reconstruction of the Au(001) surface atomic layer is incommensurate with the bulk however it is often referred to as the "5×20" or "hex" reconstruction and involves a buckling and distortion of the surface layer [70, 71]. The "hex" Au(001) reconstruction is closely aligned to the $[1\ 1\ 0]_c$ bulk direction.

Schematic representations of the reconstructed low index gold surfaces are shown in 4.1 with comparison to the unreconstructed surfaces. UHV, STM and theoretical studies have previously detailed the hexagonal gold reconstructions [72–75]. The reconstructions that occur in UHV survive transfer into electrochemical conditions, and the atomic structure of the Au surface in an electrochemical environment can be controlled by an applied potential [76, 71, 30], allowing the selection of a particular surface symmetry during an experiment.

The behaviour of the Au surfaces under electrochemical conditions have been found to be different to those observed under UHV conditions. Under electrochemical conditions, co-adsorbed solvent and adsorbed species are present on the surface, resulting in the formation of an adsorbed layer of water, adsorption of hydrogen, reversible/irreversible formation of oxygenated species and the adsorption of anions from supporting electrolyte. As anion

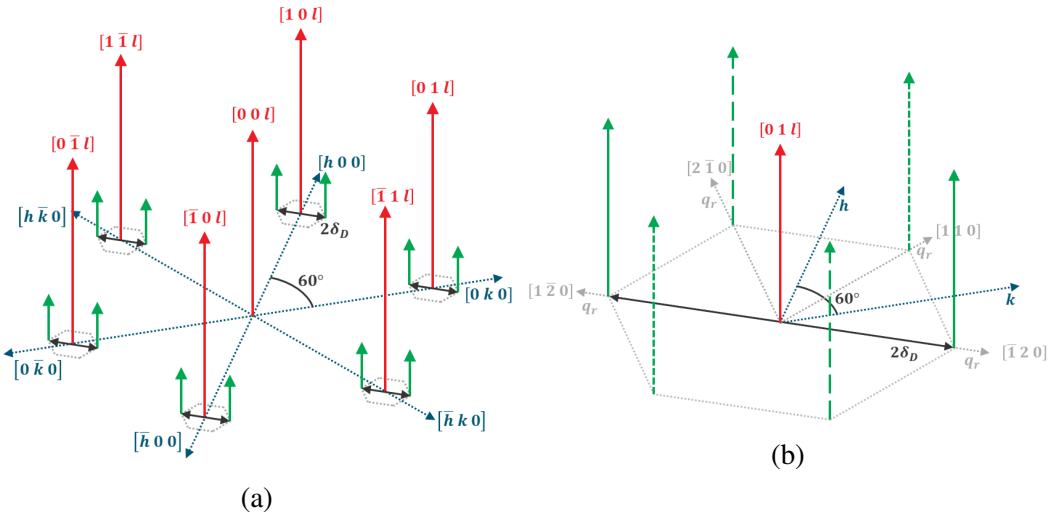

Fig. 4.2 The in-plane diffraction pattern arising due to the $(\mathrm{p} \times \sqrt{3})$ reconstructed Au(111) surface. Red arrows represent CTR scattering intensity, green arrows show scattering intensity due to the $(\mathrm{p} \times \sqrt{3})$ reconstruction. (a) The diffraction pattern for a Au(111) surface where reconstruction forms in one domain (b) A closer look at the diffraction pattern around the $(0, 1, l)$ CTR for a reconstructed Au(111) surface with 3 rotated domains (full arrows, short-dashed arrows and long-dashed arrows respectively).

adsorption occurs at the surface due to potential changes, changes in the surface electron density are induced.

The Au(111) reconstruction, described by $(\mathrm{p} \times \sqrt{3})$, where $\mathrm{p} = 23$, corresponds to a diffraction pattern made up of the CTR peaks due to the bulk Au(111) and additional rods occurring in a hexagonal arrangement around each CTR peak [77, 78]. The six additional rods that arise around each CTR due to the reconstructed surface are separated from the CTR by a distance δ_D related to p by $\delta_D = \frac{1}{2\mathrm{p}}$ within the h-k plane. Six rods appear due to the three rotational domains the reconstruction may occur within on the Au(111) surface. If the reconstruction formed in only one rotational domain the reconstruction would give rise to only two additional rods per CTR. A schematic representation of the diffraction pattern arising due to the $(\mathrm{p} \times \sqrt{3})$ reconstructed Au(111) surface is given in Figure 4.2.

When the hexagonal reconstruction of the Au(001) surface forms, the structure gives rise to a diffraction pattern, illustrated in Figure 4.3, consisting of the square lattice of CTRs due to the (001) bulk as well as additional rods of scattering intensity due to the incommensurate "hex" reconstructed surface layer [79]. The primary rods arising due to the "hex" structure form a hexagonal arrangement closely aligned to the $[1\ 1\ 0]_c$ direction and are shown as green arrows in Figure 4.3. The separation δ along the $[1\ 1\ 0]_{cubic}$ direction between the $[1\ 0\ L]_{hex}$ "hex" reconstruction rod and the $[1\ 1\ L]_{cubic}$ CTR is also marked in the schematic.

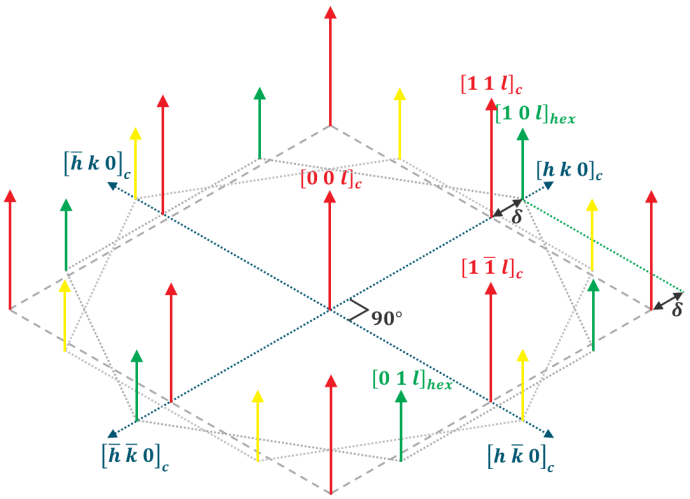

Fig. 4.3 The in-plane diffraction pattern arising due to the hexagonal reconstructed Au(001) surface. Red arrows represent scattering intensity (CTRs) due to the bulk, green arrows show scattering intensity due to one rotational domain of the "hex" reconstruction, with the other rotational domain represented by yellow arrows. CTRs are labelled with respect to the bulk reciprocal lattice directions (shown in blue) with the $[1\ 0\ l]_{hex}$reconstruction peaks labelled by their hexagonal reciprocal lattice positions.

$\delta \approx 0.2$ represents the incommensurability of the reconstruction and is related to the in-plane lattice constant of the reconstructed surface layer. The "hex" reconstruction can exist in two 90° rotational domains, illustrated in Figure 4.3 by the arrangement of green rods and the arrangement of yellow rods. The green and yellow peaks are the primary diffraction points that arise due to the reconstruction. In UHV and in acidic electrolyte, the reconstruction peaks are split, due to rotated domains, so split-peaks are observed as opposed to the single peaks observed in alkaline electrolyte, which has been found to catalyse the formation of uniform domains on Au(001) [80, 81].

It is clear that the hexagonal Au surface reconstructions hold significance for future understanding the role of Au catalysts. In this chapter, the link between applied potential and the reconstruction of the Au(111) and Au(001) surfaces in aqueous alkaline electrolytes is investigated. Alkaline solutions have a high pH allowing the reconstruction process to be observed at more negative potentials. Cyclic voltammetry for the Au(111) and Au(001) surfaces in 0.1 NaOH alkaline electrolyte, reported by Rodriguez *et al.* [64], is reproduced in Figure 4.4 (red curves) with the Au(111) exhibiting the $(\mathrm{p} \times \sqrt{3})$ reconstruction at negative potentials. The oxidation (reduction) peaks positive of 1 V (vs. RHE) are due to OH^- adsorption (desorption). The green and blue CV curves were measured with CO-saturated electrolyte, and it can be seen that on both surfaces, when the potential is not cycled to

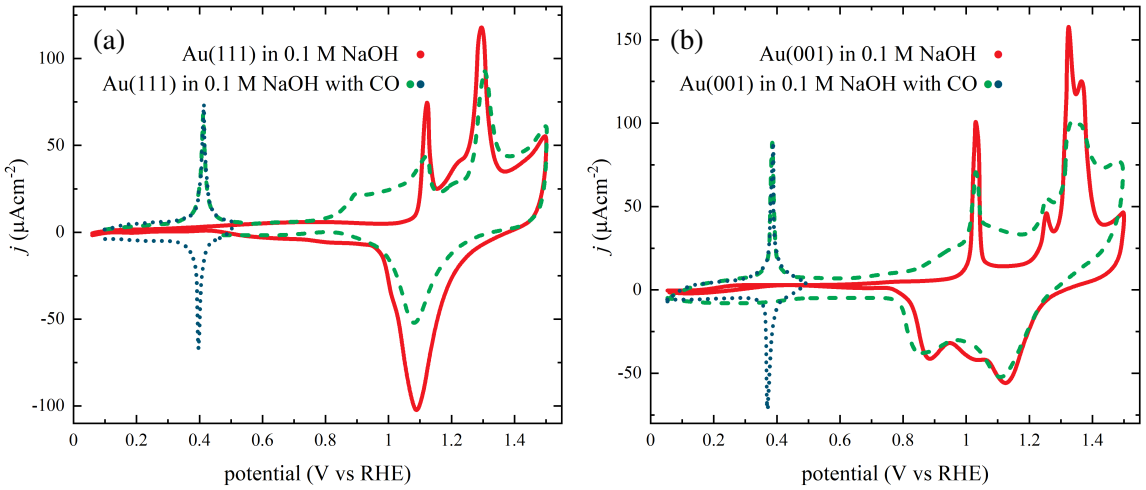

Fig. 4.4 Cyclic voltammetry for the (a) Au(111) and (b) Au(001) surfaces in 0.1 M NaOH alkaline electrolyte reproduced from a study by Rodriguez *et al.* [64]. Red curves show the CV for the gold surface in N_2-purged alkaline electrolyte and green and blue curves show the CV in CO-saturated electrolyte. Scan rate = 50 mVs^{-1}

positive enough potentials to oxidise the CO (blue curve), a peak is observed at negative potentials (close to -0.4 V vs. RHE) due to OH^- adsorption in the CO.

The Au(111) reconstruction has been observed to occur in different in alkaline electrolyte solutions (e.g. 0.1 M NaOH and 0.1 M KOH) [64, 82] and for platinum electrode surfaces in alkaline electrolytes, the effect of the cation (e.g. Na^+, K^+) has been investigated. Different cations have been shown to have an effect on the activities for the oxygen reduction, hydrogen oxidation and methanol oxidation reactions on Pt(111) surfaces [83, 84]. The hydration energies of cations follow the trend that the energy for $Li^+ > Na^+ > K^+ > Cs^+$ and it has been suggested that this trend is related to the excess of surface charge density at the Pt(111) surface in alkaline electrolytes. This indicates that different cations can influence the activities for reactions at catalyst surfaces, which raises the possibility of being able to control catalytic activity by adjusting the dissolved concentrations of cations in alkaline solutions. If a similar effect occurs for the Au(111) surface, there could be a significant influence on the potential dependence of the Au(111) reconstruction, which could be determined by SXRD to obtain detail about the cation effect on the activity of the Au(111) surface.

In this chapter, the formation and lifting of the reconstructed Au surface in 0.1 M KOH will be tracked by surface x-ray diffraction, monitoring the in-plane scattering intensity with respect to the electrode potential, to determine the potential dependence. The effect on the reconstruction of different alkaline solutions will also be investigated, by comparing samples

with 0.1 M LiOH, 0.1 M NaOH, 0.1 M KOH and 0.1 M CsOH electrolytes. The effect on the Au reconstruction of adsorbed CO on the surface will also investigated by saturating the 0.1 M KOH electrolyte with CO.

4.2 Experimental Methods

Au(111) and Au(001) single crystals (miscut < 0.1 °) were prepared by sputtering and annealing in an UHV environment until LEED analysis showed a sharp diffraction pattern. The sample was removed from UHV and prepared by annealing in a butane flame before being allowed to cool in air prior to each x-ray measurement. The crystal surface was then protected by a drop of ultrapure water and transferred to an electrochemical cell designed to facilitate surface x-ray diffraction measurements, being contacted at open circuit potential in electrolyte. Electrolyte solutions used throughout the experiment were purged with N_2 to maintain a minimal level of O_2 in the system. The Au(111) surface was investigated in 0.1 M LiOH, 0.1 M NaOH, 0.1 M KOH and 0.1 M CsOH electrolytes, to study the effect of different cations. The Au(001) surface was studied in 0.1 M KOH. Electrolyte solutions were prepared using LiOH, NaOH, KOH, and CsOH solid reagents from Sigma Aldrich (now Merck KGaA, Darmstadt, Germany).

The experimental procedure was similar to that previously established by Lucas, Marković and co-workers [48, 49]. Prior to each experiment, the potential was cycled over the range -1 V to -0.1 V (at a scan rate of 50 mVs^{-1}) for around 30-60 minutes and then held at -1 V. This process was found by Wang *et al.* to increase the correlation length by 10-30 % by repeatedly forming, lifting and re-forming the surface reconstruction, serving to condition or "groom" the surface, so that reproducible results are attainable [76]. SXRD measurements were made of the Au(111) and Au(001) surfaces in electrolyte solutions at the I07 beamline at Diamond Light Source, Oxfordshire, UK [38] and at BM28, the XMaS beamline at the ESRF, Grenoble, France [43]. The close packed Au(111) surface, as described in 2.4.1, has a hexagonal unit cell which is defined such that the surface normal is along the $[0\ 0\ l]_{hex}$ direction and the $[h\ 0\ 0]_{hex}$ and $[0\ k\ 0]_{hex}$ directions are within the surface plane and subtend 60 °. The units of h, k and l are defined by

$$\mathbf{b}_1 = \mathbf{b}_2 = \frac{4\pi}{\sqrt{3}a_{NN}} \quad \text{and} \quad \mathbf{b}_3 = \frac{2\pi}{\sqrt{6}a_{NN}} \tag{2.33}$$

where the nearest neighbour distance for gold $a_{NN} = 2.884$ Å. The Au(001) surface (2.4.2) was indexed to the bulk *fcc* unit cell. The surface was protected from O_2 by purging the chamber containing the x-ray cell with N_2. A Ag/AgCl reference electrode was used in the

x-ray electrochemical thin layer cell, and it is against this reference that all potentials are quoted.

For a more detailed description of the experimental methods followed, please refer to Chapter 3.

4.3 Results and Discussion

Surface x-ray diffraction was employed in the study of the Au(001) and Au(111) surface reconstruction processes in alkaline electrolyte to determine the potential dependence of structure changes that each surface undergoes. The results are presented and discussed in Section 4.3.1. Further experiments were carried out in alkaline electrolyte saturated with carbon monoxide, to determine the influence on the reconstruction processes of adsorbed CO at the surface. Results of the investigation into the effect of CO on the gold reconstruction are reported in Section 4.3.2. Finally, Section 4.3.3 presents the findings of an investigation into the influence of the cation in the electrolyte solution on the reconstruction of the Au(111) surface. Data obtained for the Au(111) surface in 0.1 M LiOH, 0.1 M NaOH and 0.1 M CsOH are compared with that presented in Section 4.3.1 for 0.1 M KOH electrolyte.

4.3.1 Au(001) and Au(111) Reconstruction in 0.1 M KOH

The reconstructions of the Au(001) and Au(111) surfaces were investigated in 0.1 M KOH electrolyte solution in a surface x-ray diffraction (SXRD) experiment. The Au(001) reconstruction was investigated by observing the diffracted x-ray intensity at surface-sensitive reciprocal space positions. An in-plane scan along the $[1\ 1\ 0]_{cubic}$ direction can be performed through the $(1,1,l)$ CTR and rod that arises due to the reconstructed Au(001) surface, labelled as $[1\ 0\ l]_{hex}$ in Figure 4.3. The reconstruction peak occurs at the $(1+\delta, 1+\delta)$ in-plane position, and so observing the diffracted intensity while scanning along h and k through this position allows the intensity profile of the reconstruction peak to be measured. Such scans are performed while holding the potential at a range of potentials, so that the potential dependence of the reconstruction may be investigated.

Figure 4.5 shows the scattered intensity measured along the $[1\ 1\ 0]_{cubic}$ direction through the reconstruction peak, which occurs at negative electrode potentials. The peak is shown for measurements made while holding the potential at -1.0 V, -0.5 V and -0.2 V, indicated respectively by the red, green and blue curves through the data points. The curves shown in Figure 4.5 are Gaussian line-shapes fitted to the data with a linear background. At more positive potentials, the peak is not observed due to the lifting of the reconstruction.

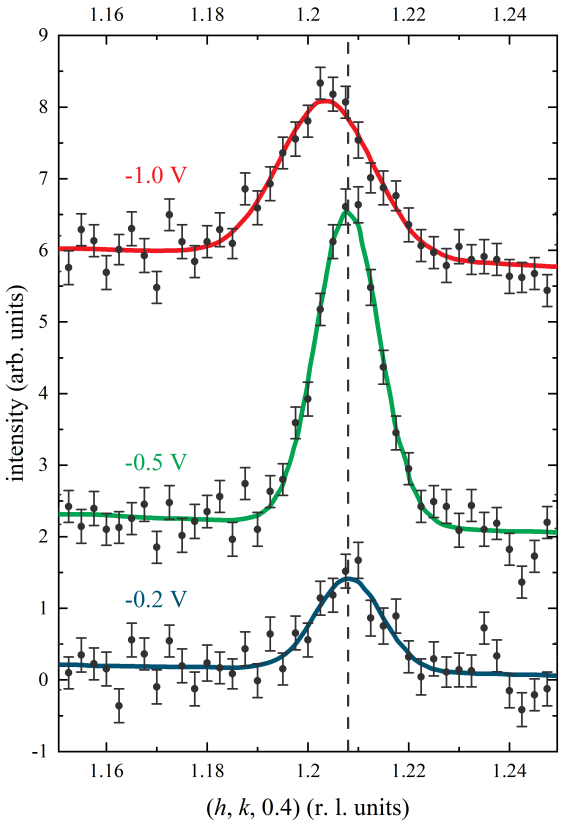

Fig. 4.5 Fitted curves to the scattered x-ray intensity scanned along the $[110]_{cubic}$ direction measured through the reconstruction peak shown at approximately $(1.2, 1.2, 0.4)_{cubic}$, measured for the reconstructed Au(001) surface in 0.1 M KOH. The data was fitted with a Gaussian line-shape (solid curves). Scans were measured while holding the electrode potential at -1.0 V (red curve), -0.5 V (green curve) and -0.2 V (blue curve). The peak position at -0.5 V is indicated by the dashed black line.

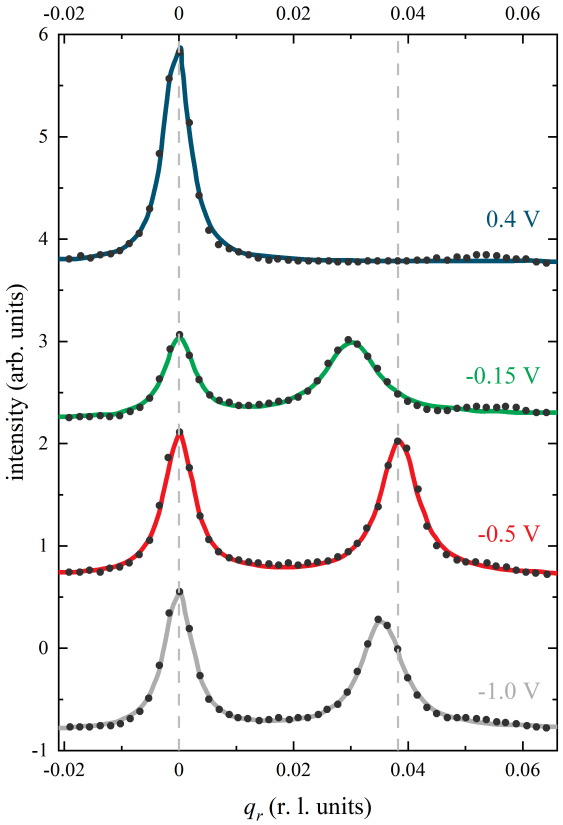

Fig. 4.6 Fitted curves to the scattered x-ray intensity measured for the reconstructed Au(111) surface in 0.1 M KOH. The data, measured along the [1 1 0] direction, was fitted with a double Lorentzian line-shape (solid curves) for the $(0,1,0.3)$ CTR (left, at $q_r = 0$) and reconstruction peak (right, at $q_r = \delta_D$). Scans were measured while holding the electrode potential at -1.0 V (grey curve), -0.5 V (red curve), -0.15 V (green curve) and 0.4 V (blue curve). The peak position at -0.5 V is indicated by the dashed grey line.

Rocking scans were performed through the diffraction peak and found no evidence that the reconstructed layer was rotated with respect to the underlying Au lattice, as expected from previous Au(001) experiments in alkaline electrolyte [70].

To investigate the Au(111) surface, in-plane scans of the scattered intensity were performed along a direction q_r such that the scan passes through the reciprocal lattice position of the CTR and a reconstruction peak. An example of such a scan direction q_r is indicated by the grey arrow in the schematic of the reconstructed Au(111) surface (Figure 4.2b), where the vector passes along the $[\bar{1}\ 2\ 0]$ direction through the $(0,1,l)$ CTR position (red arrow) and the reconstruction peak (green arrow), which would appear at the $(0-\delta_D, 1+2\delta_D, l)$ position.

The Au(111) surface reconstruction in 0.1 M KOH was investigated during a series of experiments, using multiple single crystal samples. The ordering of the $(\mathrm{p}\times\sqrt{3})$ reconstruc-

tion and the precise value of the stripe separation, p, that represents the surface symmetry after prolonged potential cycling (surface conditioning) was found to vary between 22 and 23 depending on the individual crystal sample, however in each case the behaviour and processes observed were consistent. The stripe separation for a given sample is dependent on the quality of the crystal, with some exhibiting a p of up to 26.

Figure 4.6 shows data measured along the $[1\ 1\ 0]$ q_r direction, through the $(0, 1, 0.3)$ CTR and the reconstruction peak. The scattered x-ray intensity profile along this scan direction was recorded while holding the electrode potential at a number of potentials across the potential window at which the reconstruction is expected based on the literature (Figure 4.4). Two peaks are clearly visible at negative electrode potentials, with the CTR peak observed at q_r = 0 and a second peak arising at $q_r \approx 0.038$ due to the $(\mathrm{p} \times \sqrt{3})$ reconstruction. In these units, the stripe separation p is given by $\mathrm{p} = \frac{\sqrt{3}}{2q_r}$ where q_r is the reconstruction peak separation from the CTR position (q_r = 0).

Investigations of Au(001) and Au(111) and their hexagonal surface reconstructions showed that both the intensity and the position of the reconstruction peaks arising in the negative potential region were dependent on the applied electrode potential and exhibited changes across the potential region. The measurements presented in Figure 4.5 and 4.6 were made while stepping the potential positively from -1.0 V, as the Au(001) and Au(111) surface reconstructions were lifted. Analysis of the *hk* scans was carried out by taking into account the linear background and fitting Lorentzian line shapes to the peaks arising due to the CTR and the reconstruction rod using the program Fityk [85]. Line shapes fitted to the x-ray data are shown in Figure 4.5 and 4.6. The reconstruction peak positions obtained through fitting curves to the scans allow calculation of structural properties of the surface at stages during the reconstruction process. The integrated intensities of the reconstruction peaks, the in-plane Au near-neighbour spacing ($\mathrm{a_{NN}}$) and the coherent domain size, L can be obtained [76] and are plotted as a function of electrode potential in Figure 4.7 for the Au(001) "hex" reconstruction. Figure 4.8 shows the integrated intensity, stripe separation p and coherent domain size, L determined from fitting the reconstruction and CTR peaks for the Au(111) reconstruction. Figure 4.7 and 4.8 also show the potential dependence of the CTR integrated intensities. It is clear that as the reconstruction peak intensity begins to decrease as the applied potential is stepped positive of -0.3 V for Au(001) and +0.2 V for Au(111). As the reconstruction begins to be lifted on both surfaces, the CTR intensity begins to rise. This shows the structural rearrangement of Au atoms into the unreconstructed Au surface structures at positive potentials, with increasing contribution to the CTR scattering intensity. At the positive ends of these potential scales, the scattering is larger at the measured positions for the (1×1) termination of the crystal surfaces than for the reconstructed surfaces.

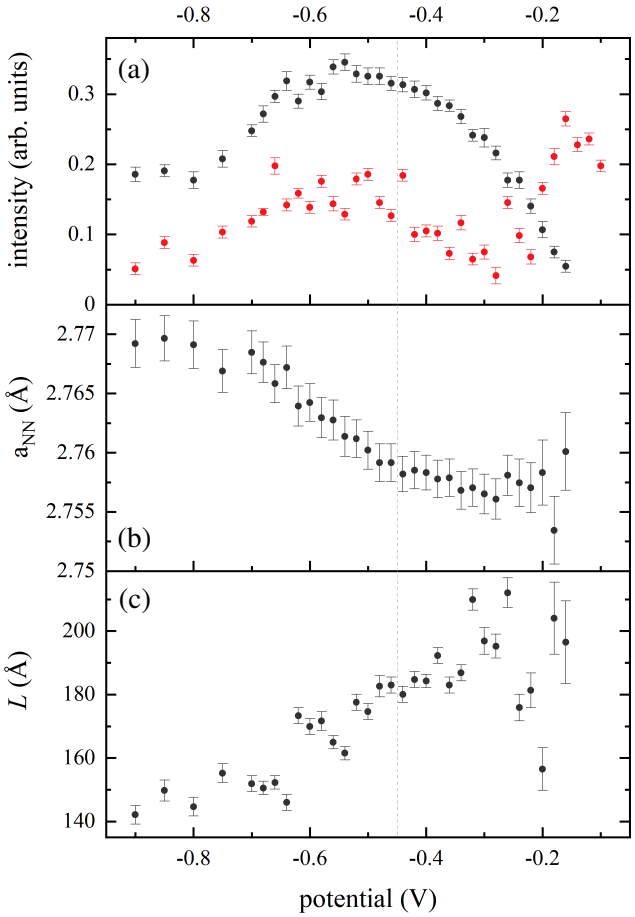

Fig. 4.7 (a) Integrated intensity of the reconstruction peak (black points) and $(1,1,0.4)$ CTR peak (red points) as a function of electrode potential. (b) Potential dependence of the in-plane near neighbour spacing (lattice constant, a_{NN}) calculated for Au atoms in the Au(001) "hex" reconstructed surface. a_{NN} is determined from fits to the data, as shown in Figure 4.5. (c) Potential dependence of the domain size, L of the "hex" reconstructed Au(001) surface, also determined from fitted data.

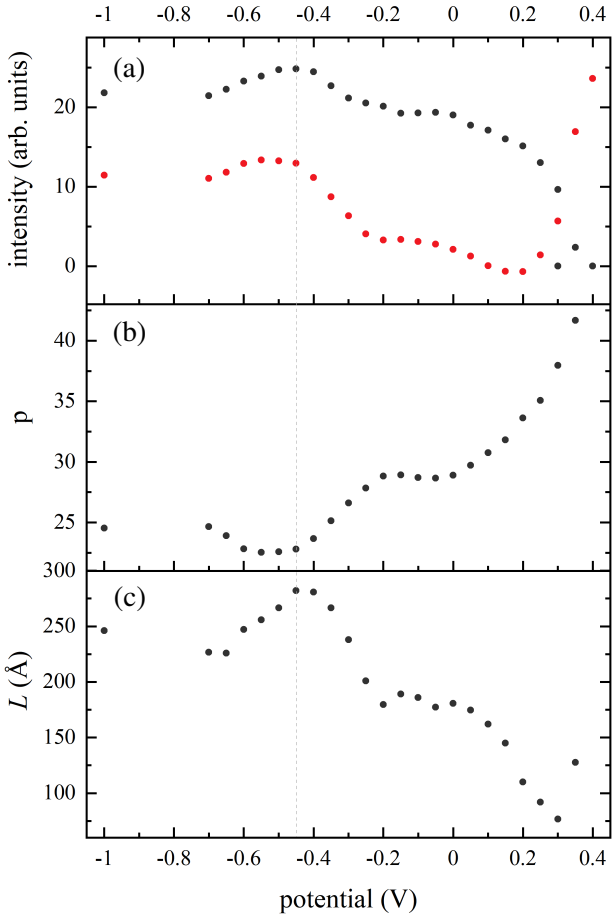

Fig. 4.8 (a) The integrated intensity of the reconstruction peak (black points) and the $(0,1,0.3)$ CTR peak (red points) measured at different electrode potentials for the reconstructed Au(111) surface. (b) The stripe separation, p is also shown, as well as (c) the domain size, L of the $(\mathrm{p}\times\sqrt{3})$ reconstruction, which are calculated from the fitted data (as shown in Figure 4.6).

Figure 4.7 and 4.8 show that there is a notable potential dependent change in behaviour of the surface reconstructions across the potential regions in which they are stably present. Data from the rotated domains showed the same behaviour for both the Au(111) and Au(001) surfaces. In the case of Au(001), symmetry equivalent reflections also gave the same results, indicating that the change in Au near-neighbour spacing is isotropic across the surface. For Au(111), measurements were consistent across four single crystal samples, with similar potential dependent results to those shown in Figure 4.8 for the compression of the reconstructed surface layer, although the exact value for p measured at -1.0 V after cycling did vary with different samples (p values varied between 23.5 and 26).

Previous electrochemical studies of the Au alkaline environment [86, 82] have identified that at potentials negative of -0.45 V there is no specific adsorption, whereas during a positive potential sweep, -0.45 V is the point at which the onset of hydroxide (OH^-) adsorption occurs. This points also corresponds to an observed a minimum in the differential capacitance [87]. At potentials between -1.0 V and -0.45 V, for both the Au(111) and Au(001) surface reconstructions, the reconstruction peak increases during a positive potential sweep. Figure 4.7 and 4.8 also indicate that as the reconstruction peak increases with this potential change, the in-plane correlation length L also increases and the near neighbour spacing a_{NN} (and proportional stripe separation p for the Au(111) surface) decreases. These changes describe a compression of the atoms in reconstructed surface structure as the potential is swept positive up to -0.45 V from -1.0 V. The increased in-plane Au-Au spacing at negative potentials is understood to be due to the increased charge at the surface. There is no specific adsorption at this potential, so excess surface charge influences the Au-Au interaction within the surface layer.

The 2D isothermal compressibility of the reconstructed Au monolayer κ_{2D} is described by

$$\kappa_{2D} = \frac{1}{N_{ion}e}\left(\frac{dA}{dE}\right) \tag{4.1}$$

where $\frac{dA}{dE}$ is the change in area A per adsorbate atom [88], which may be determined from the potential dependence of p. Assuming a 2D free electron gas model, the 2D isothermal compressibility κ_{2D} and electro-compressibility κ_T can be compared to determine the surface charge of Au atoms eN_{ion}, when κ_T is described [5, 89] by

$$\kappa_T = \frac{m_e A^2}{\pi\hbar(Z - N_{ion})^2} \tag{4.2}$$

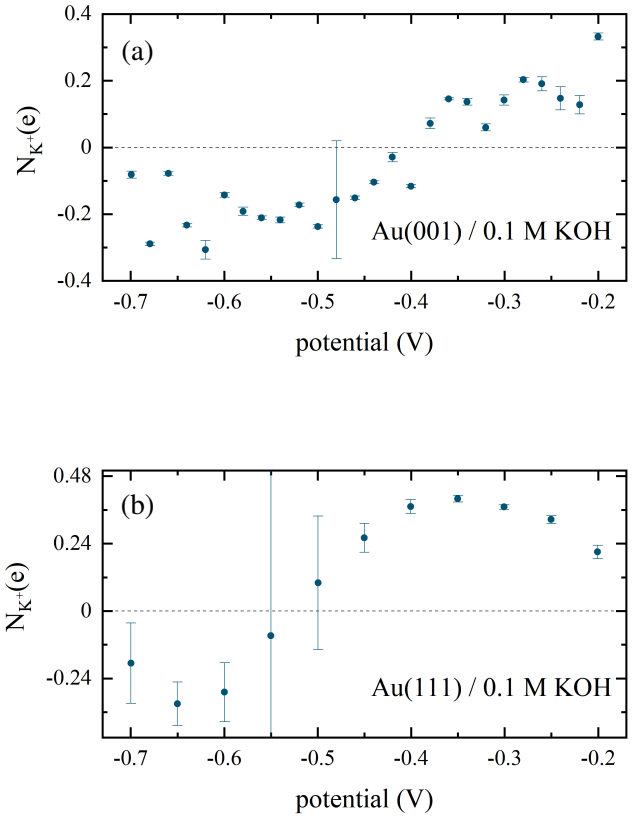

Fig. 4.9 The potential dependent surface charge per atom obtained for the reconstructed (a) Au(001) and (b) Au(111) surfaces by comparing the experimental electro-compressibility to the compressibility for a 2D layer in the free electron model

where $(Z - N_{ion})$ is the number of electrons contributing to the free electron gas, m_e is the electron mass and $\hbar$ is the reduced Planck constant.

The charge of the surface Au atoms eN_{ion} may be determined by assuming the electro-compressibility is given by a 2D isothermal compressibility and setting $\kappa_{2D} = \kappa_T$. Figure 4.9 shows the surface charge plotted as a function of potential for the reconstructed Au(001) and Au(111) surfaces, shown in 4.9a and 4.9b respectively. The values of electro-compressibility obtained were of the order 1 Å^2/eV, which are of the same order as those found during previous studies of electrochemically deposited metallic monolayers [90–92]. This model is based on the free electron model and neglects any influences of 5d electrons however it shows that the observed potential dependent behaviour of the electro-compressibility can be explained by the changing charge of the surface atoms. The point at which the sign of

the charge changes in Figure 4.9 corresponds to the potential at which the in-plane near neighbour spacing a_{NN} reaches a minimum.

During a positive potential sweep in KOH electrolyte, -0.45 V is the potential marking the onset of hydroxide adsorption on the gold surfaces, which leads to the lifting of the reconstruction of the Au(001) and Au(111) surfaces. During the lifting of the Au(111) surface reconstruction, a stable intermediate phase is formed, between potentials of -0.2 V and 0 V, before the reconstruction is completely lifted. Similar intermediate phases have been reported in STM studies of Au(111) in acidic electrolyte [93]. On Au(001), the reconstruction immediately begins to lift as potential increases beyond -0.45 V, and the process is not accompanied by a further change in the in-plane compression. In the case of Au(001) surface, it appears that the adsorption of hydroxide species drives the lifting of the reconstruction.

4.3.2 The CO Effect

The promoting effect of CO adsorbed on Au(111) and Au(001) on the electro-oxidation of alcohols has been previously reported [61–65] and an experiment was carried out with the aim of determining possible links between the structural changes detailed in Section 4.3.1 and the electrocatalytic behaviour. While holding the potential at the negative limit, the N_2 purged 0.1 M KOH electrolyte in the electrochemical cell was replaced by 0.1 M KOH solution that had been saturated with CO. The Au(111) and Au(001) surfaces were investigated by carrying out SXRD measurements similar to those reported in Section 4.3.1 and represented by Figures 4.5 and 4.6.

Figure 4.10 shows SXRD results for the reconstructed Au(001) and Au(111) (4.10a and 4.10b respectively) surfaces in CO saturated 0.1 M KOH, representing the potential dependence of the hexagonal gold reconstructions in the presence of CO. At -1.0 V, both the Au(001) and Au(111) surfaces are found to be reconstructed, as evidenced by the intense reconstruction peak at $h = k \approx 1.2$ in Figure 4.10a and $q_r \approx 0.04$ in Figure 4.10b. The in-plane lattice constant for both surfaces is close to the maximum surface compression ($a_{NN} \approx 2.76$ Å) and the correlation length L shows no significant change from that observed in N_2 purged electrolyte. In CO saturated electrolyte, stepping the electrode potential from -1.0 V to -0.2 V revealed no change in the position of the reconstruction peak, and negligible change in the integrated intensity of the reconstruction peak on either surface. This indicates that the presence of CO inhibits any change in the surface compression of either hexagonal reconstruction over this potential range, with the data measured at -0.5 V presented in Figure 4.10a and Figure 4.10b. Adsorbed CO suppresses the potential induced changes in the Au near neighbour lattice spacing on the Au(001) and Au(111) surfaces. This could be

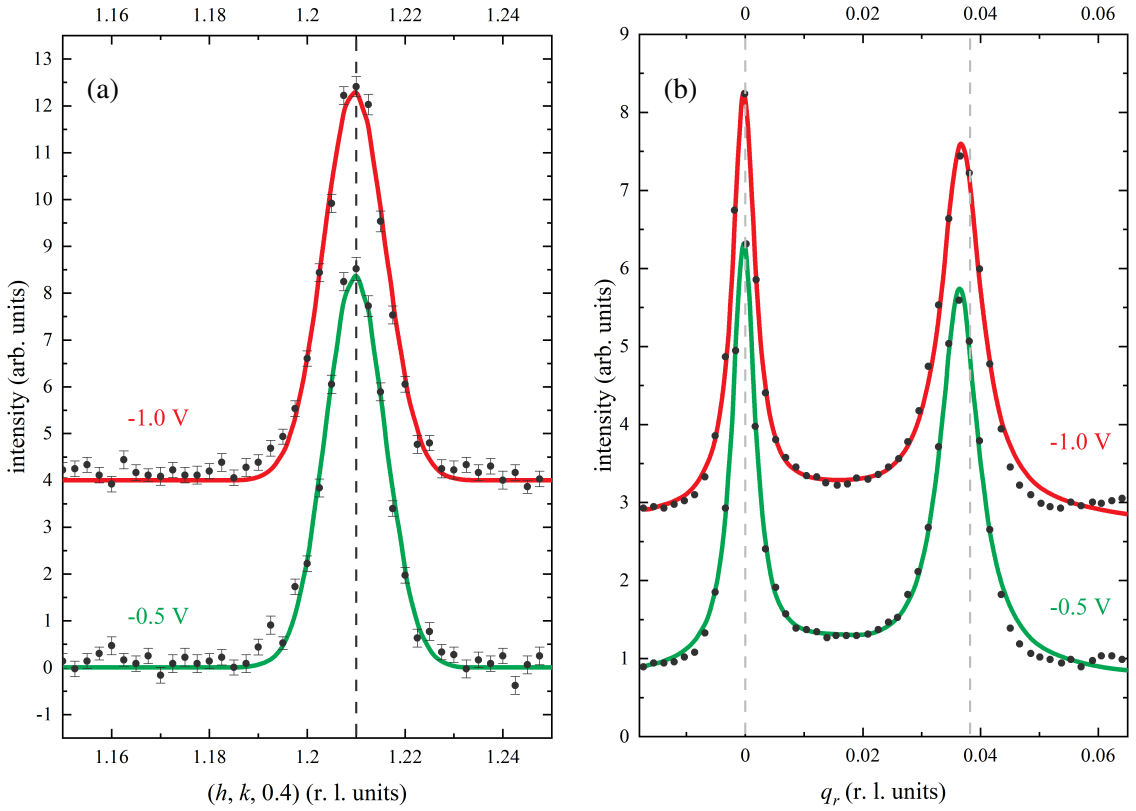

Fig. 4.10 In plane x-ray diffraction of the reconstructed (a) Au(001) surface measured along the [110] direction through the reconstruction peak and (b) the reconstructed Au(111) surface measured along the [110] direction through the $(0, 1, 0.3)$ CTR position and the reconstruction peak, with both surfaces in CO saturated 0.1 M KOH electrolyte. The potential was held at: -1.0 V (red curves), -0.5 V (green curves)

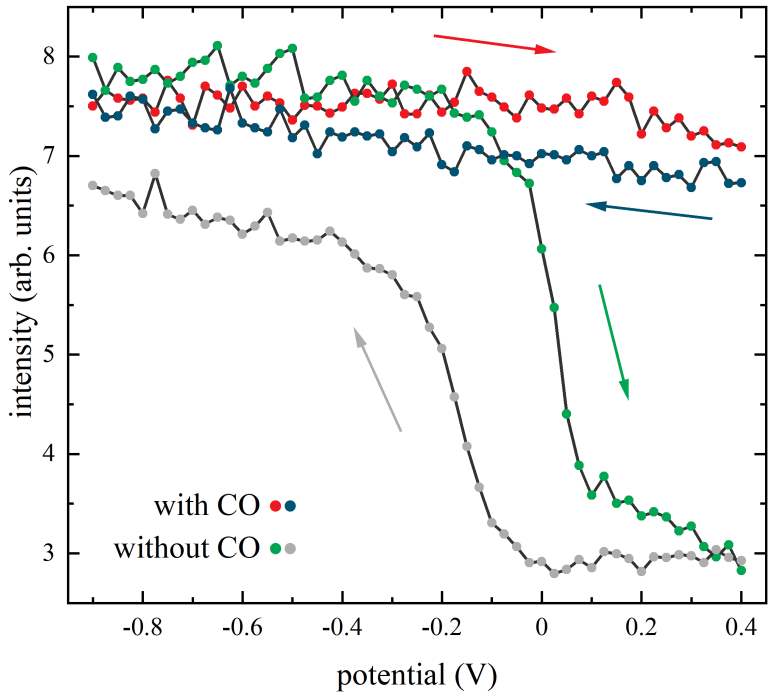

Fig. 4.11 X-ray voltammetry measurements showing the potential dependence of the scattered x-ray intensity from the $(0,0,1.02)$ anti-Bragg position on the specular CTR as the potential is swept from -1.0 V to 0.4 V and back (sweep rate = 2 mVs^{-1}). Results are shown for the Au(001) surface in 0.1 M KOH before (green and grey points) and after (red and blue points) the electrolyte was saturated with CO. Positive and negative potential sweeps are indicated by arrows

explained by a modification of the electron density by the presence of and bonding to CO molecules. The adsorbed CO molecules may accommodate changes in the surface charge, rather than the Au atoms, meaning that the Au atoms do not undergo the same structural rearrangement. In such case the CO molecules act as tuneable dipoles, which could explain the enhanced catalytic activity reported for Au surfaces with adsorbed CO, with reactions at the interface taking place in the outer layer of the electrochemical double layer (the OHP, Section 2.2.2). This is consistent with the model of CO-promoted OH^- adsorption being the mechanism by which hexagonal Au surfaces exhibit enhanced electro-oxidation of alcohols.

Previous studies have shown that adsorbed CO on the Au(001) surface stabilises the reconstructed phase over a wider potential range in comparison to the absence of CO [82]. Figure 4.11 shows x-ray voltammetry measurements at the $(0,0,1.02)$ anti-Bragg position on the specular CTR as a function of the electrode potential. The figure compares the x-ray voltammetry measurements made of the Au(001) surface in 0.1 M KOH electrolyte before (green and grey points) and after (red and blue points) saturating the electrolyte with CO. The

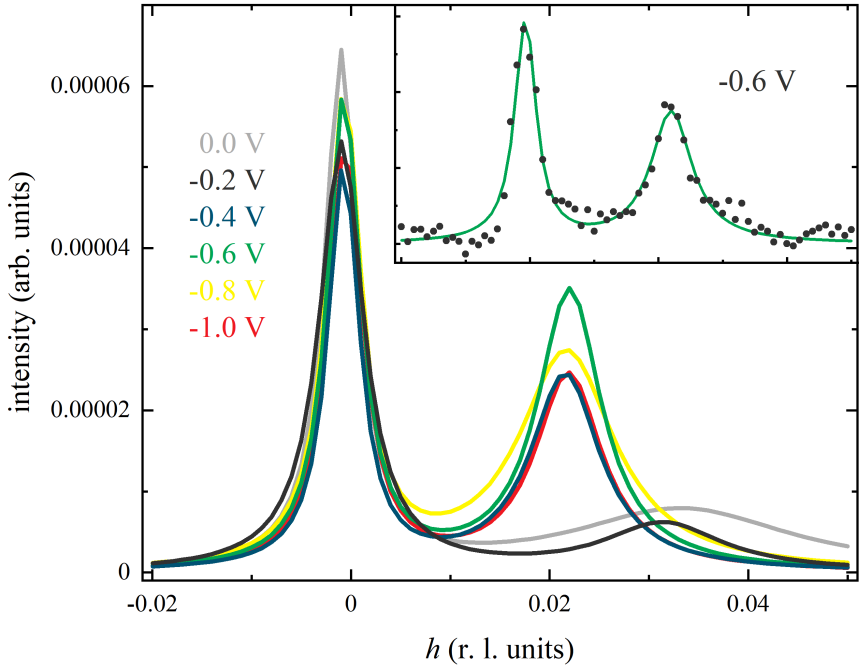

Fig. 4.12 Fitted curves to the scattered x-ray intensity scanned along the $[110]$ direction measured through the $(0,1,l)$ CTR (left peak) and the reconstruction peak (right peak) for the Au(111) surface in 0.1 M NaOH electrolyte solution. Scans measured while holding the potential at 0 V (grey), -0.2 V (black), -0.4 V (blue), -0.6 V (green), -0.8 V (yellow) and -1.0 V (red). Inset plot shows the curve (green line) fitted to the x-ray data (black points) for the -0.6 V measurement.

$(0,0,1.02)$ anti-Bragg position on the specular CTR is sensitive to the atomic density of the Au surface layer and therefore the black points in the figure show the change in intensity as the reconstruction is lifted and reformed at $\approx$ -0.1 V. The red points in the graph indicate that in the presence of CO, the Au(001) reconstruction is preserved during the positive potential sweep beyond -0.1 V and right up to positive potentials at which the onset of oxide formation occurs. The results are therefore consistent with the previous reports of CO stabilising the reconstructed phase [82].

4.3.3 The Cation Effect

The potential dependence of the Au(111) surface reconstruction and the compressibility of the hexagonal reconstruction was also investigated in other alkaline electrolyte solutions. A surface x-ray diffraction (SXRD) experiment was carried out to determine the effect of

different cations on the potential dependent behaviour of the reconstructed Au(111) surface, by carrying out similar experiments in 0.1 M NaOH, 0.1 M LiOH and 0.1 M CsOH electrolyte solutions to that detailed in Section 4.3.1. The scattered intensity from the surface along an in-plane direction q_r through the CTR position and the reconstruction rod position was measured by SXRD. The directions q_r along which in-plane intensity scans were measured are illustrated in Figure 4.2b along with the scattering rods detected. The intensity was scanned along the [1 1 0], $[\bar{1}\ 2\ 0]$, $[1\ \bar{2}\ 0]$ and $[2\ \bar{1}\ 0]$ directions through the $(0,1,0.5)$ and $(0,1,0.7)$ positions on the $(0,1,l)$ CTR and the $(1,\bar{1},0.7)$ position on the $(1,\bar{1},l)$ CTR. The schematic also shows the positions of the additional rods of scattering due to the reconstructed surface, illustrating how scans along these directions (grey arrows) detect both the CTR (red arrow) and the reconstruction peak (green arrow).

From these in-plane scans (*hk* scans), the dependence of the reconstruction peak intensity and position can be compared as a function of potential for different cations (Na, Li, Cs). A suitable potential window within which the lifting of the reconstruction could be observed was chosen, from -1 V to -0.1 V, and *hk* scans were performed at 0.05 V or 0.1 V intervals over the potential window. Line shapes fitted to the x-ray intensity measured during the *hk* scans of the Au(111) surface in 0.1 M NaOH electrolyte are presented in Figure 4.12.

Along the [1 1 0] direction, the position of the reconstruction rod relative to the CTR is determined by fitting the peaks and obtaining the peak centre positions. The separation is described by δ_D, given in Miller units (2.33). For scans along another in-plane direction q_r, it is necessary to convert the units. δ_D is related to the unit cell dimension p by

$$\mathrm{p} = \frac{1}{2\delta_D} \tag{4.3}$$

The width of the reconstruction peak is also related to the domain size of the reconstructed surface, L, which is calculated by

$$L = \frac{\sqrt{2\ln 2}}{4\pi\sigma_\delta} \tag{4.4}$$

where σ_δ is the half width half maximum of the reconstruction peak.

A plot of the intensity, p value and the domain size L as a function of potential is shown for the Au(111) surface in 0.1 M NaOH measured along the [1 1 0] direction (Figure 4.14). The same is plotted for the Au(111) / 0.1 M CsOH system, measured along the $[1\ \bar{2}\ 0]$ direction (Figure 4.15). The third electrochemical system investigated was Au(111) in LiOH and the results are shown in Figure 4.13 for the reconstruction measured along the $[\bar{1}\ 2\ 0]$ direction.

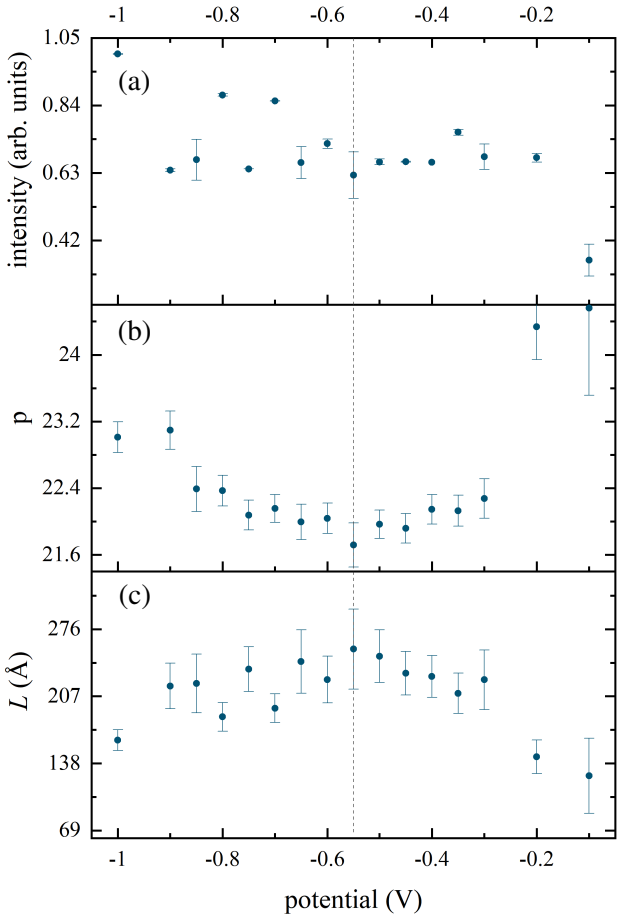

Fig. 4.13 (a) The x-ray intensity, (b) p and (c) domain size, L as a function of potential for the Au(111) in 0.1 M LiOH system when the reconstruction is investigated along the $\left[\bar{1}\ 2\ 0\right]$ direction. The x-ray intensity shown is that of the reconstruction peak.

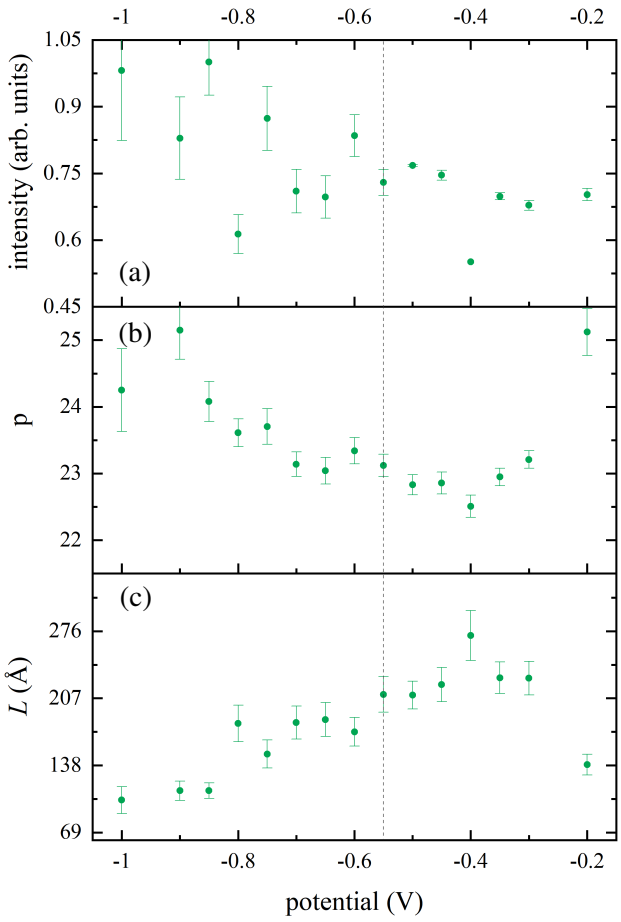

Fig. 4.14 (a) The x-ray intensity, (b) p and (c) domain size, L as a function of potential for the Au(111) in 0.1 M NaOH system when the reconstruction is investigated along the [1 1 0] direction. The x-ray intensity shown is that of the reconstruction peak.

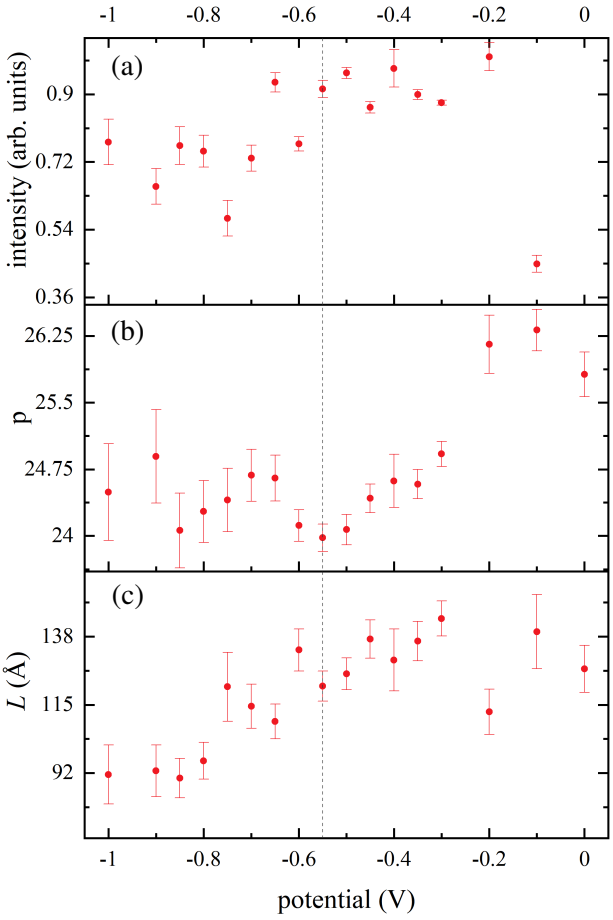

Fig. 4.15 (a) The x-ray intensity, (b) p and (c) domain size, L as a function of potential for the Au(111) in 0.1 M CsOH system when the reconstruction is investigated along the $\left[1\ \bar{2}\ 0\right]$ direction. The x-ray intensity shown is that of the reconstruction peak.

The Gibbs free energy of hydration for cations of Group 1 elements Li^+, Na^+, K^+ and Cs^+ are -475 kJ mol^{-1}, -365 kJ mol^{-1}, -295 kJ mol^{-1} and -250 kJ mol^{-1} respectively [94], where the energy to dehydrate an ion is largest for ions with a lower atomic number. The number of H_2O molecules in the hydration shell is given as 5.2, 3.5, 2.6 and 2.1 [94] respectively for Li^+, Na^+, K^+ and Cs^+. Therefore, as Li^+ requires more energy for dehydration, it is more likely that Li^+ ions are adsorbed at an electrode surface in a fully solvated state (rather than a partially solvated state) than K^+ and Cs^+ ions. Cs^+ ions are more likely to be adsorbed in partially solvated states than K^+ and Li^+ ions [95]. According to the double layer model described in Section 2.2.2, ions in a partially solvated state are situated in the inner Helmholtz plane (IHP), with fully solvated ions in the outer Helmholtz plane (OHP).

This offers an explanation for the shape of the potential dependence of the p value as presented in Figures 4.13 to 4.15, where Figures 4.13 and 4.14 show that the potential dependence is similar for the LiOH and NaOH electrolytes. For 0.1 M CsOH electrolyte (Figure 4.15), the potential dependence of p features a sharp minimum at -0.55 V, whereas for LiOH and NaOH, the decrease in p with increasing potential is more gradual. Cs^+ ions have fewer H_2O molecules in the hydration shell than Li^+ and Na^+ therefore the reconstruction is more sensitive to small changes in the applied potential.

The trend in the gradient of the potential dependence of p, where p changes with a sharper gradient for ions with fewer H_2O molecules in their hydration shell, is also in agreement with the results for Au(111) in 0.1 M KOH electrolyte, in Figure 4.8. Comparing the results to determine the effects of K^+, Li^+, Na^+ and Cs^+ ions, we can see that K^+ ions have a similar effect on the Au(111) reconstruction. The stripe separation p of the reconstruction in KOH electrolyte has a clear potential dependence comparable to that observed in the other alkaline electrolytes. With changing potential, the stripe separation drops to a minimum at -0.55 V, with the gradient of that drop being similar to that in Figure 4.15 (CsOH) and sharper than those shown in Figures 4.13 and 4.14 (LiOH and NaOH).

The compressibility of the reconstructed surface depends on the change in area per adsorbate atom, A with potential $\frac{dA}{dE}$, which can be determined from the potential dependence of p. Assuming a 2D free electron gas model, the 2D isothermal compressibility κ_{2D} and electro-compressibility κ_T can be compared to determine the surface charge of Au atoms eN_{ion}, the potential dependence of which is shown in Figure 4.16.

This is consistent with the data for 0.1 M KOH electrolyte (Figure 4.9). Comparison between the studies shows that as well as with K^+ cations, with Li^+, Na^+ and Cs^+ cations the change in electro-compressibility is also driven by the change in charge of surface atoms.

Figure 4.16 shows the potential dependence of the charge of the surface Au atoms and the charge changes sign at -0.55 V, where the nearest neighbour distance is at a minimum.

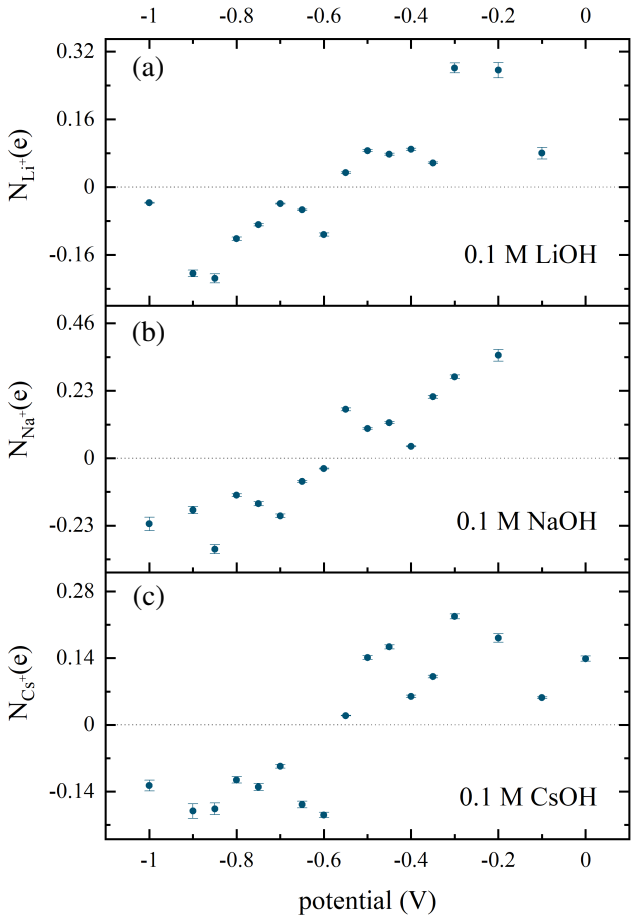

Fig. 4.16 The potential dependence of surface charge per atom for the reconstructed Au(111) surface in (a) LiOH, (b) NaOH and (c) CsOH electrolytes. Charges calculated from the experimental electro-compressibility and comparison with the 2D compressibility in the free electron model.

For electrolyte with Cs^+ cations there is a sharper change with potential whereas the change is more gradual for Li^+ and Na^+. This suggests that the charge of surface atoms is more sensitive to the applied potential when ions with fewer H_2O in their hydration shell and this drives the reconstruction process. This is also evident in the data presented in Figure 4.9 for KOH electrolyte. K^+ ions have more H_2O ions in their solvation shell (2.6) than Cs^+ (2.1) but fewer than Li^+ (3.5) and Na^+ (5.2) [94].

4.4 Conclusions

We have seen that the hexagonal reconstructions that occur on the Au(001) and Au(111) electrode surfaces in alkaline electrolyte exhibit a potential dependent compressibility. The origin of the compressibility is considered to be an effect of the build up of charge at the surface at potentials negative of -0.5 V, where the compression is highest at -0.5 V. Describing the system using the free electron model indicates that at -0.5 V, the charge on the surface Au atoms reaches a minimum, leading to the tight compression of the atoms. This potential also corresponds to the onset of hydroxide (OH^-) adsorption, which leads to a reduction of the surface compression on the Au(111) surface, and a lifting of the surface reconstruction on Au(001). In CO-saturated electrolyte, CO molecules are adsorbed onto the Au surface at -1.0 V. The potential dependent surface compressibility is suppressed in this case, with both Au(001) and Au(111) surfaces locked into the highly compressed phases that are observed in CO-free electrolyte at -0.5 V. The results suggest that the adsorbed CO molecules accommodate the excess surface charge that is induced by the applied electrode potential, with this mechanism leading to the enhanced electrocatalytic reactivity observed for Au(001) and Au(111) with adsorbed CO. The adsorbed CO also leads to the reconstructed surfaces being stable over a larger potential range. These characteristics both indicate that the presence of CO at Au(001) and Au(111) surfaces is preferable for the preparation of catalyst surfaces for industrial and research applications.

It was also determined, by considering the effect of alkaline electrolyte solutions with different cations, that the number of H_2O molecules in the solvation shell of the cation influences the degree of potential dependent compressibility exhibited by the Au(111) surface reconstruction. When ions in the electrolyte have fewer H_2O molecules in the solvation shell, the compressibility of the Au(111) surface reconstruction was more sensitive to changes in the applied potential, and the compression process of Au atoms was observed over a shorter potential range.

Chapter 5

Surface Stability of Cu(111) in Phosphate Electrolyte

5.1 Introduction

Carbon dioxide pollution as a by-product of the combustion of fossil fuels is well documented as one of the most significant challenges humanity faces today, continuing to dominate headlines as an increasingly urgent crisis. CO_2 is largely an unwanted result of many industrial processes, and a key area of interest within electrochemistry is its conversion into useful products. Large scale, energy efficient conversion of CO_2 into more desirable chemicals could be vital in reducing greenhouse gases amid the ongoing climate crisis as well as having a positive economic impact in terms of creating jobs in a new industry.

Copper surfaces and copper oxide-derived surfaces are important metal catalysts as they uniquely offer the electrochemical conversion of CO_2 into methane, ethylene, formic acid, methanol, ethanol and other useful products [96–98]. The parameters and conditions that influence the efficiencies of these processes, and the selectivity (the ability to choose a desired product from those that may be produced) are not fully understood. Parameters such as the surface area, particle size, surface structure, surface roughness and electrolyte composition have been suggested to control the selectivity and reactivity for CO_2 conversion into useful products [99–104].

In the case of copper oxide catalysts, the level of oxygen content and oxidation state has been found to affect the electrocatalytic activity and selectivity. Oxide-derived Cu catalysts have shown high-selectivity towards the formation of C_2 products (such as ethylene) [105, 98, 106, 107]. The selectivity exhibited by such catalysts has been attributed to changes in the surface structure, such as defects and roughness, which lead to the formation of active sites during the pretreatment of Cu-oxide catalysts.

More recent studies have proposed that as well as structural properties, the presence of Cu^+ ions and subsurface oxygen atoms may affect the product selectivity [103, 108, 109]. Mistry *et al.* used operando XAFS to demonstrate the presence of Cu^+ species and subsurface oxygen during the carbon dioxide reduction reaction [103]. Another report, by Le Duff *et al.* implemented a pulse sequence between reduction potentials, where the CO_2 reduction reaction (CO2RR) takes place (< -0.5 V) and a potential in the region between -0.2 V and -0.35 V (quoted vs. RHE) where the co-adsorption of OH and other anions takes place [105, 110]. They concluded that the positive potential of the pulse had a significant effect on the catalytic activity and selectivity of the copper single crystal electrode for the CO2RR. This was associated with the adsorbed species (OH or anions) at the surface, which prevent any irreversible damage or changes to the Cu electrode surface structure [105].

In this chapter, a structural characterisation of the Cu(111) electrode by surface x-ray diffraction (SXRD) will be presented at potentials positive of the CO2RR, with the aim of determining the composition and structure of the electrochemical interface. In order to understand the stability and reactivity of the Cu(111) electrode, the surface morphology must be controlled during preparation of the sample, because, depending on the preparation method, two different surface morphologies may be obtained. One surface is macroscopically rough but is completely stable during potential cycling that drives the adsorption/desorption of anions and associated reversible rearrangement of the surface structure. The other surface exhibits x-ray scattering features that suggest the presence of twinned copper nano-islands at the surface, and the potential dependent changes in surface structure are found to occur irreversibly, indicating an unstable surface. In-situ structural characterisation of the surface is unique in providing detail on the stability of the surface structure. Correlating this with information on the reactivity is key to understanding the relationships between stability and reactivity, which is important for studies of more active metal electrodes [30, 2].

5.2 Experimental Methods

The Cu(111) single crystal working electrode surface (miscut < 0.1 °) was prepared by electropolishing for 10 s in 70 % orthophosphoric acid at 2 V against a high surface area copper mesh. The crystal was then rinsed in ultrapure water before being submerged in the buffered phosphate electrolyte solution and transferred to an electrochemical cell designed to facilitate surface x-ray diffraction measurements, where the sample was immediately contacted at -0.8 V. The x-ray cell (described in Chapter 3.4) employed a copper wire counter electrode and a Ag/AgCl reference electrode, which all potentials are quoted relative to. Electrolyte solutions used throughout the experiment were purged with N_2 to maintain a

minimal level of O_2 in the system. The Cu(111) surface was investigated by surface x-ray diffraction in 0.1 M phosphate buffered electrolyte solution at pH = 8, prepared using 98+ % HK_2PO_4 reagents from Fisher Scientific (Fisher Scientific UK Ltd., Loughborough, UK) and KH_2PO_4 from Sigma Aldrich (now Merck KGaA, Darmstadt, Germany).

The experimental procedure for the structural characterisation of the Cu(111) surface was similar to that followed in Chapter 4 and established by Lucas, Marković and co-workers [48, 49]. SXRD measurements were made at the I07 beamline at Diamond Light Source, Oxfordshire, UK [38]. The close packed Cu(111) surface, as described in 2.4.1, has a hexagonal unit cell which is defined such that the surface normal is along the $[0\ 0\ l]_{hex}$ direction and the $[h\ 0\ 0]_{hex}$ and $[0\ k\ 0]_{hex}$ directions are within the surface plane and subtend 60 °. The units of h, k and l are defined by

$$\mathbf{b}_1 = \mathbf{b}_2 = \frac{4\pi}{\sqrt{3}a_{NN}} \quad \text{and} \quad \mathbf{b}_3 = \frac{2\pi}{\sqrt{6}a_{NN}} \tag{2.33}$$

where the nearest neighbour distance for copper is $a_{NN} = 2.556$ Å.

5.3 Results and Discussion

The Cu(111) surface was characterised in phosphate buffered electrolyte by electrochemical methods prior to surface x-ray diffraction (SXRD) studies which aimed to characterise the surface atomic structure.

5.3.1 Electrochemical Characterisation

Cyclic voltammetry experiments were carried out on the Cu(111) surface in phosphate buffered electrolyte solutions of different concentration and pH. Samples with solution concentrations of 0.01 M, 0.05 M and 0.1 M were investigated, with both pH = 6 and pH = 8. The cyclic voltammograms are presented in Figure 5.1a for the pH = 6 sample and Figure 5.1b for pH = 8. An anodic peak, a_2 with a shoulder a_1 is visible in all samples, however a_2 is much more defined at the lower pH. In Figure 5.1a and 5.1b, the green curve represents measurements made of Cu(111) in 0.1 M phosphate buffer solution, with the blue curve showing 0.05 M concentration and the red curve 0.01 M. At pH = 6, the anodic peak a_2 can be seen to shift further negative with increasing phosphate concentration.

The total charge associated with the electrochemical processes is plotted in Figure 5.1c and 5.1d, showing the charge in pH = 6 and pH = 8 solution respectively. The charges in the anodic and cathodic scans were found to be equal, and between 52 and 60 μC cm^{-2} for

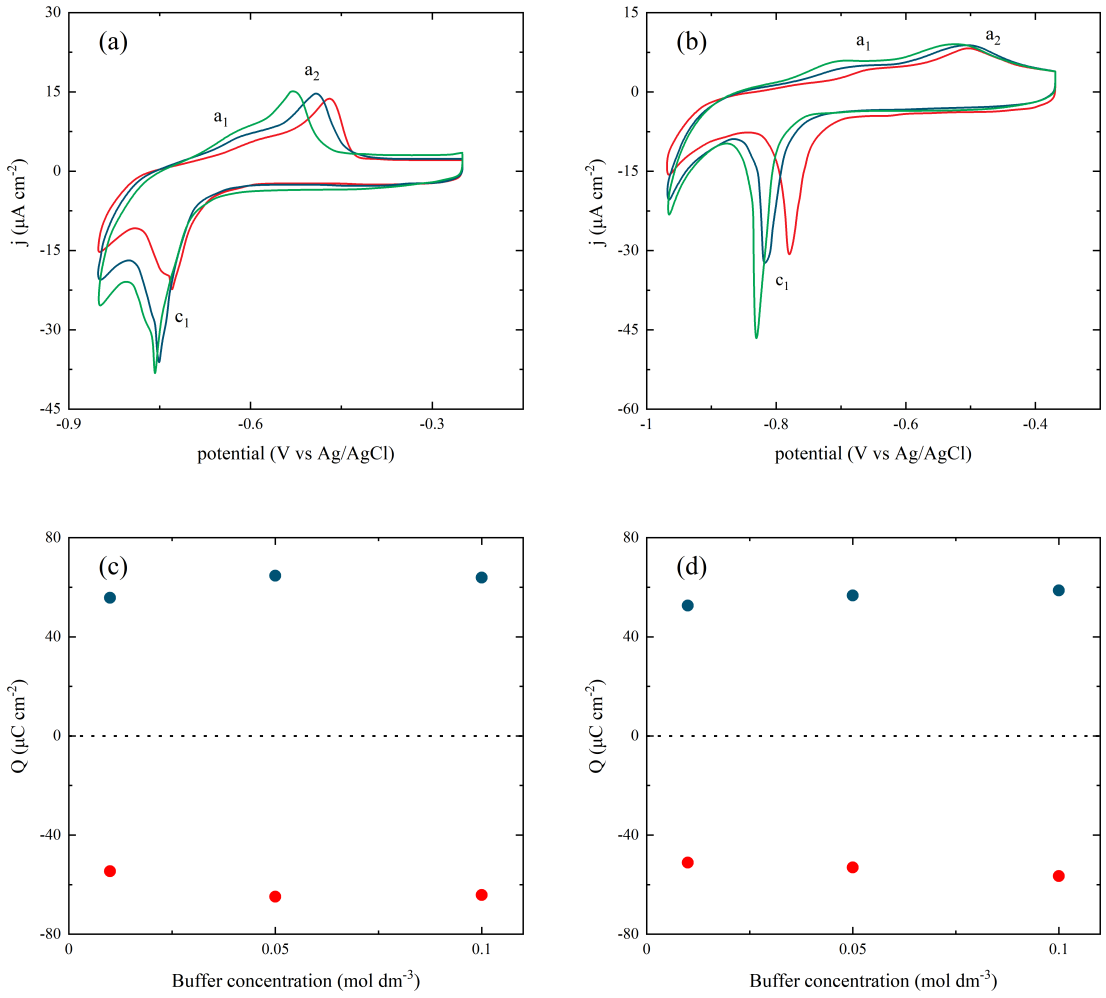

Fig. 5.1 Cyclic voltammetry measurements made with scan rate = 0.02 V s^{-1} of the Cu(111) surface in phosphate buffer solution at (a) pH = 6 and (b) pH = 8, with phosphate concentrations of 0.01 M (red curve), 0.05 M (blue curve) and 0.1 M (green curve). Charge involved in the oxidative (blue) and reductive (red) processes on the Cu(111) surface in phosphate buffer solution at (c) pH = 6 and (d) pH = 8.

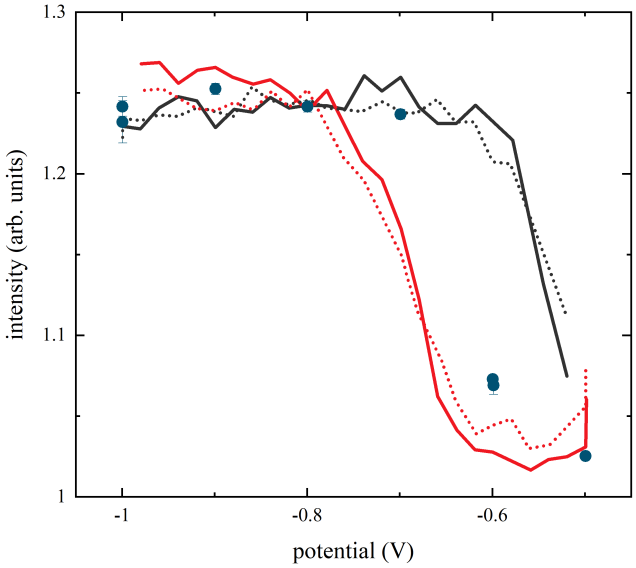

Fig. 5.2 X-ray voltammetry measurements measured at the $(0, 1, 0.5)$ non-specular anti-Bragg position (solid line) and the $(0, 0, 1.4)$ specular anti-Bragg position (dotted line) on the CTR, with sweep rate = 2 mV s^{-1}. Blue points show the integrated intensity obtained from rocking scan measurements at the $(0, 1, 0.5)$ position at select potentials.

the 3 solution concentrations (0.01 M, 0.05 M and 0.1 M). This charge corresponds to ~ 0.2 electrons per surface atom and was found to be independent of concentration or pH of the electrolyte solution.

5.3.2 Structural Characterisation

In-situ surface x-ray diffraction measurements of the Cu(111) surface in 0.1 M phosphate buffer solution at pH = 8 were carried out while changing the applied electrode potential. The potential dependence of x-ray diffraction from specular and non-specular Bragg positions over the range -1 V to -0.5 V was measured, with representative results for the $(0, 0, 1.4)$ specular and $(0, 1, 0.5)$ non-specular anti-Bragg positions shown in the x-ray voltammetry plot in Figure 5.2 (solid and dotted lines respectively). The XRV data at both positions show, during a scan from -1 V to -0.5 V, a stable intensity at negative potentials up to -0.6 V, before the intensity decreases significantly. The negative scan, back to -1 V from -0.5 V, shows at both positions a stable intensity between -0.5 V and -0.6 V, before the intensity increases between -0.6 V and -0.8 V. The intensity recovers back to the same level measured prior to the positive potential scan, indicating that the structural change associated with this potential dependent change in intensity is a reversible process. The separation in potential between

the observed decrease and increase in intensity is described as a hysteresis between the two changes in structure. This hysteresis is indicative of significant surface restructuring.

The specular anti-Bragg position is sensitive to changes in electron density normal to the surface, with the non-specular $(0,1,0.5)$ anti-Bragg position sensitive to changes in the in-plane Cu surface structure or adsorption into well-defined Cu(111) surface sites. The fact that both positions exhibit a potential dependent change indicates that the process involves a significant change in structure at the interface, likely a change in Cu surface structure. The blue points in Figure 5.2 show the integrated intensities of rocking scans measured at the $(0,1,0.5)$ position while stepping the electrode potential incrementally from -1 V to -0.5 V and holding at each potential. The same potential dependence of the intensity is observed, however the integrated intensities fall halfway inside the hysteresis loop, which is as expected as these static measurements allow time for the mass transport to occur during the restructuring of the surface.

As the potential was stepped from -1 V to -0.5 V, a detailed characterisation of the Cu(111) surface was carried out by crystal truncation rod (CTR) measurements made at 0.1 V increments. Following these measurements, the potential was stepped negative back to -0.8 V to check the reproducibility of results and stability of the surface. A study of the stability of the surface is presented in Figure 5.3, in which the potential history of the electrode over the course of the experiment is shown, with the peak widths (Figure 5.3a) and integrated intensities (Figure 5.3b) given for rocking scans carried out at the $(0,1,0.5)$ position. Examples of such rocking scans are shown in Figure 5.3c, in which a scan at -0.9 V (blue points) and a scan at -0.6 V (red points) are shown, with the Lorentzian curves fitted to the data shown in grey. The rocking scans show how the intensity changes significantly with the change in electrode potential. From Figure 5.3b it is clear that the peak width remained consistent throughout the experiment, indicating that the domain size (which is inversely proportional to the rocking scan peak width) did not change and that the sample remained stable. The intensity was found to reversibly change with applied potential, as expected from the XRV results (Figure 5.2), by comparing the results at -0.8 V before and after the step to more positive potentials. The rocking scans at -0.8 V were found to be consistent. Figure 5.3b shows that low intensities ($\sim$0.5-2 arbitrary units in the figure) were measured at -0.8 V after the potential was stepped back to -0.8 V from -0.5 V, however this intensity increased with time as the potential was held at -0.8 V, rising back up to $\sim$5.5 arbitrary units. This hysteresis is indicative of significant mass transport occurring at the electrode surface.

The CTR data measured for the Cu(111) surface in buffered phosphate electrolyte is presented in Figure 5.4. The $(0,\ 1,\ l)$, $(1,\ 0,\ l)$ and $(1,\ 1,\ l)$ CTRs were measured, and a model of the surface was determined from the data by a least-squares fit calculation. A

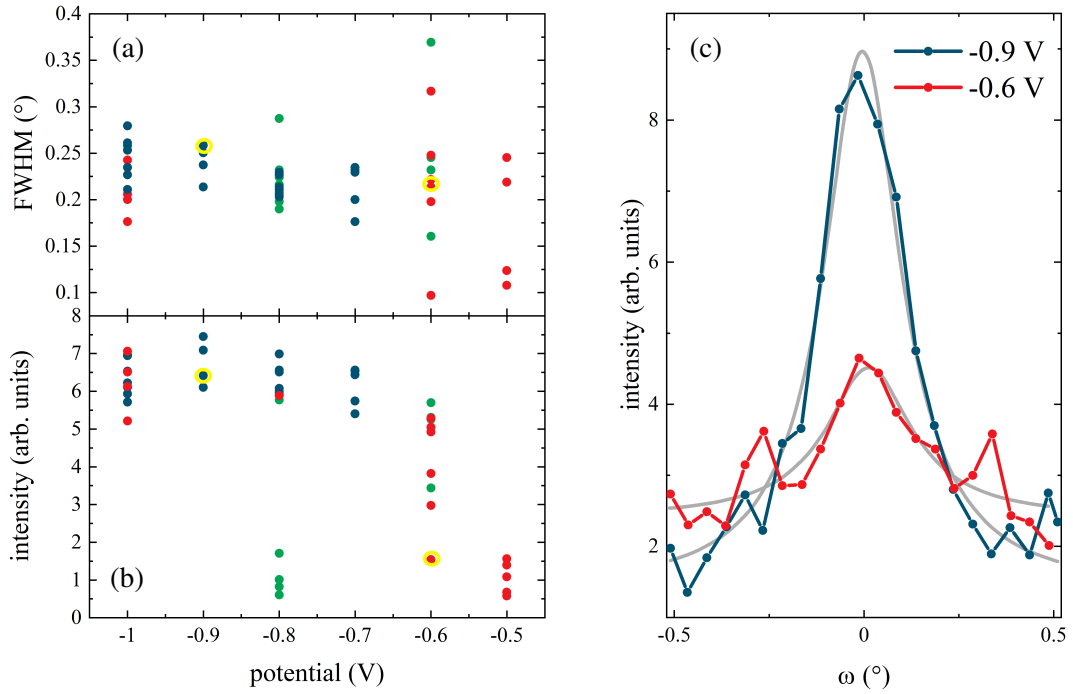

Fig. 5.3 The (a) full width half maximum (FWHM) and (b) integrated intensity of x-ray rocking scans measured at the $(0, 1, 0.5)$ non-specular CTR position over the course of the experiment with respect to the applied electrode potential. Blue points were measured when stepping potential from -1 V to -0.7 V, red points from -1 V to -0.5 V and green points from -0.8 V to -0.6 V. (c) Peak profiles of two example rocking scans, measured at -0.9 V and -0.6 V (blue points and red points respectively) are shown along with Lorentzian line shapes fitted to the data (grey curves). These scans are highlighted by yellow circles in (a) and (c).

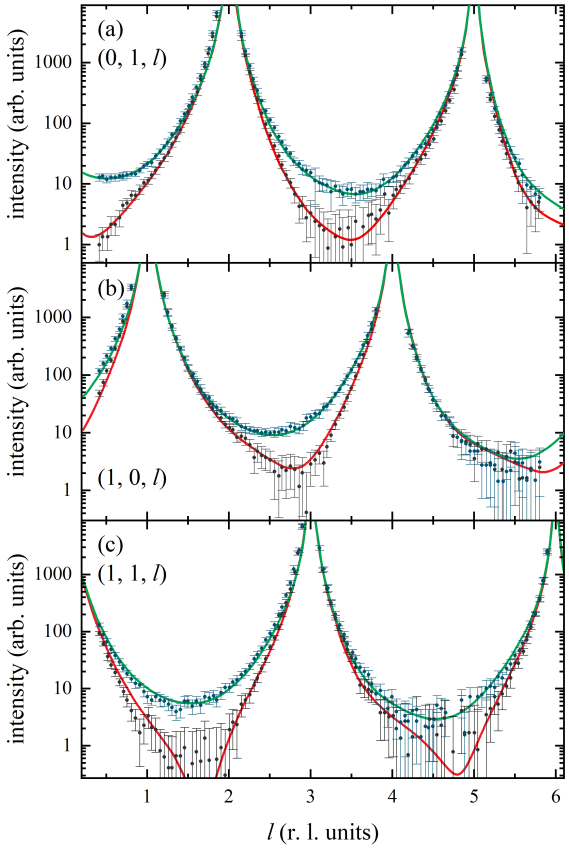

Fig. 5.4 CTR data measured at -0.8 V (blue symbols) and -0.5 V (black symbols) presented with calculated fits to the data (green and red curves respectively) for the Cu(111) surface in 0.1 M phosphate buffer solution at pH = 8.

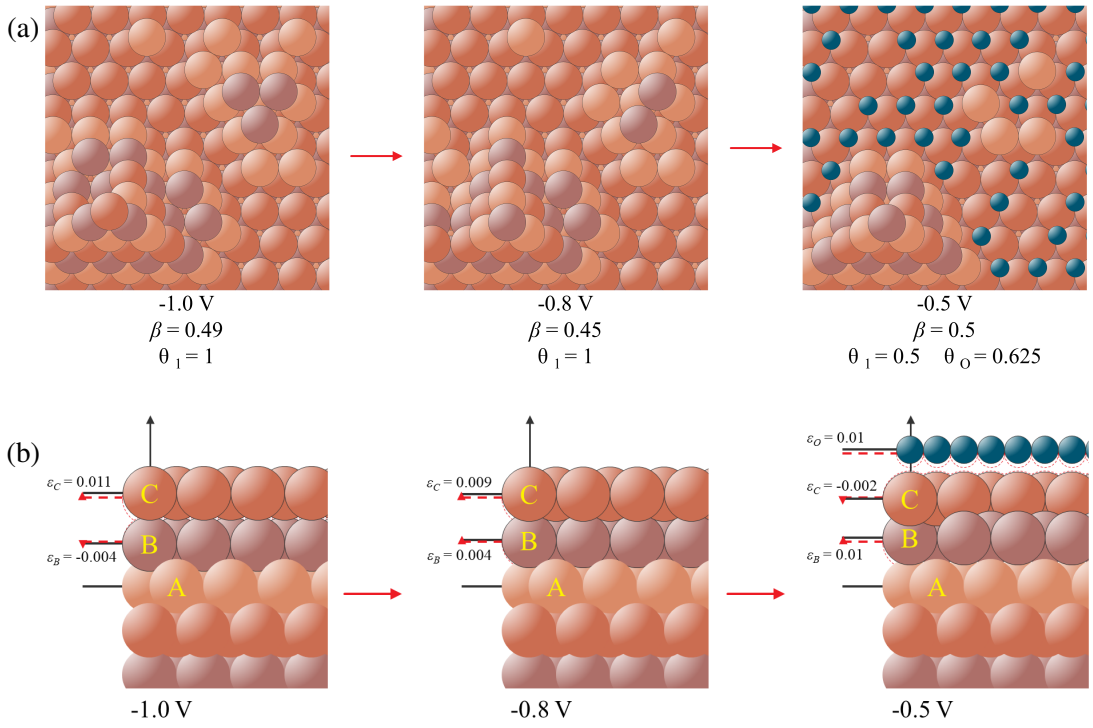

Fig. 5.5 Schematic diagram showing the structure changes observed at the Cu(111) surface as the potential was stepped from -1.0 V to -0.8 V to -0.5 V. The surface roughness as modelled by a β-model is shown for each electrode potential (β), along with the coverages of the first Cu layer (θ_1) and O adlayer (θ_O). The out-of-plane expansion is shown for the first (ε_C) and second (ε_B) Cu layers and the O adlayer (ε_O). (a) shows the observed change in roughness in the surface plane of the top Cu layers and the adsorption of oxygen atoms (represented by blue spheres) (b) illustrates the changes in out-of-plane position of the Cu and O atomic layers, showing the expansion and relaxation of the top two Cu layers as well as the O adlayer.

comparison is made between the data measured at -0.8 V, which is represented in Figure 5.4 by blue points and the data measured at -0.5 V, represented by black points plotted for each CTR. The calculated model fitted to the data at -0.8 V is plotted as a green curve, with a red curve showing the fit to the data at -0.5 V. It can be seen that the intensity at anti-Bragg positions is lower when the potential is held more positive, than the intensity at more negative potential. This is indicative of an atomically rough surface at the positive potential. It is also clear from inspection of Figure 5.4 that the CTRs at -0.5 V are more asymmetric around the Bragg peaks, which is due to a change in the relaxation of the atomic layers.

The CTR data was fitted using a structural model by varying the coverage of the topmost copper layer, the relaxation of the top two copper layers and the roughness of the surface

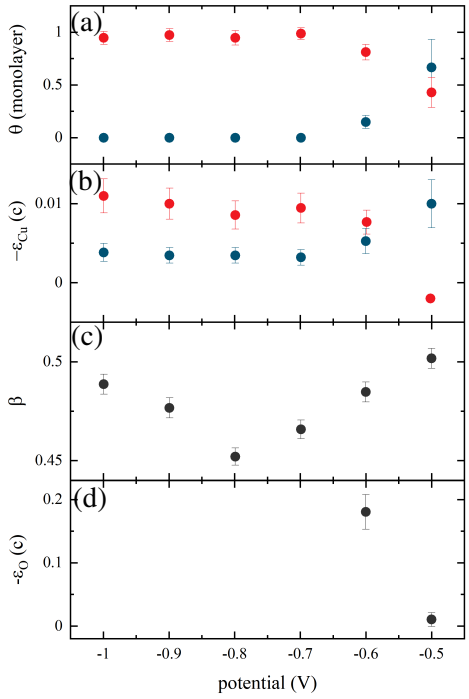

Fig. 5.6 Model parameters used to fit the CTR data in Figure 5.4 are shown as a function of potential. (a) The coverage (θ) of the surface Cu layer (red points) and adsorbed O layer (blue points). (b) The relaxation, $-\varepsilon_{Cu}$ of the 1st Cu layer (red points) and the 2nd Cu layer (blue points). (c) The roughness of the surface as modelled through a β roughness factor. (d) The relaxation, $-\varepsilon_O$ of the adsorbed O layer.

(via a β-factor model [111]). To fit the data at positive potentials an oxygen layer was also included in the modelling, with oxygen atoms sitting in *fcc/hcp* three-fold hollow sites in the Cu(111) surface. The data CTR modelling therefore reveals that at positive potentials in buffered phosphate electrolyte, the Cu(111) surface exhibits a roughened surface with adsorbed oxygenated species and a relaxation of the top two Cu layers. This change in structure has been shown to be reversible by stepping the electrode potential back to a negative value, and a schematic representation of the structure is given in Figure 5.5.

The parameters varied when calculating structural model are shown in Figure 5.6 for the potential range from -1 V and -0.5 V, with Figure 5.6a showing the coverage of the topmost Cu layer (red points) and the adsorbed oxygen layer (blue points) in the Cu(111) surface model. A stable, full monolayer of Cu was observed between -1 V and -0.7 V, whereas the coverage of Cu in the top layer of the single crystal surface decreased at potentials positive of that point. With decreasing Cu coverage in the top copper layer, the adsorbed oxygen coverage in the layer above increased, where there had been adsorbed oxygen at potentials

negative of -0.7 V in the model of the surface fitted to the CTRs. Including oxygen in the model resulted in a decrease in the reduced χ^2 from 3.3 to 1.8 for the least squares fit to the data at -0.5 V, indicating a good fit. Also shown are parameters relating to the relaxation of the top two Cu layers, the relaxation of the oxygen layer and the roughness of the surface (a higher β-factor corresponding to atomically less well-ordered surface layers). The schematic diagram representing these surface structure changes, shown in Figure 5.5, illustrates the relaxation and expansion of the surface layers in a side-on view (Figure 5.5b). It can be seen that the top Cu layer starts off outwardly expanded from the position in an ideal Cu(111) unit cell (represented by a red dashed line) at 1.0 V, with the layer slightly relaxing between 1.0 V and -0.8 V, and relaxing further between -0.8 V and -0.5 V as the oxygen adsorption occurs. The second Cu layer is slightly relaxed at 1.0 V and undergoes expansion between 1.0 V and -0.8 V and further expansion as the potential is stepped to -0.5 V. The top-down view of the surface given in Figure 5.5a shows how the surface roughness slightly decreases between 1.0 V and -0.8 V, and oxygen adsorption occurs at -0.5 V.

To check for any additional superstructure peaks, in-plane scans were carried out at $(h,\ 0,\ 0.4)$, $(0,\ k,\ 0.4)$ and $(h,\ k,\ 0.4)$ positions at each potential. No superstructure peaks were observed, indicating that there is no ordering of the surface in the presence of phosphate or any oxygenated species. Such ordering would give rise to additional x-ray scattering along the high symmetry directions in reciprocal space. Previous studies of the oxidation of the Cu(111) surface at the solid-gas interface as well as computational studies have suggested that hexagonal or quasi-hexagonal structures form with the adsorption of oxygen [112]. These proposed structures form the initial layer of a Cu_2O(111) film. Platzman *et al.* suggest the oxidation of the Cu(111) surface occurs via three steps: the formation of the Cu_2O layer, the formation of a metastable overlayer of $Cu(OH)_2$ and finally the transformation of the metastable overlayer phase into a CuO layer. The results of this investigation however did not reveal signs of any of these structures within the potential range from -1 V and -0.5 V.

The data presented above was obtained with a Cu(111) single crystal sample that had been electropolished and transferred quickly to the electrochemical cell, where it was immediately contacted at -0.8 V. The morphology of the surface was found to be strongly dependent on the method of preparation of the single crystal surface and the transfer into the electrochemical environment, with this method devised to minimise the exposure to oxygen. When samples were prepared without taking these measures, a different surface morphology was observed, evident by the appearance of additional scattering features in the observed CTR data (Figure 5.7).

Gas phase studies have shown that the oxidation of Cu(111) occurs by epitaxial growth of copper oxide islands [113, 114]. The growth of copper oxide has been shown to depend on

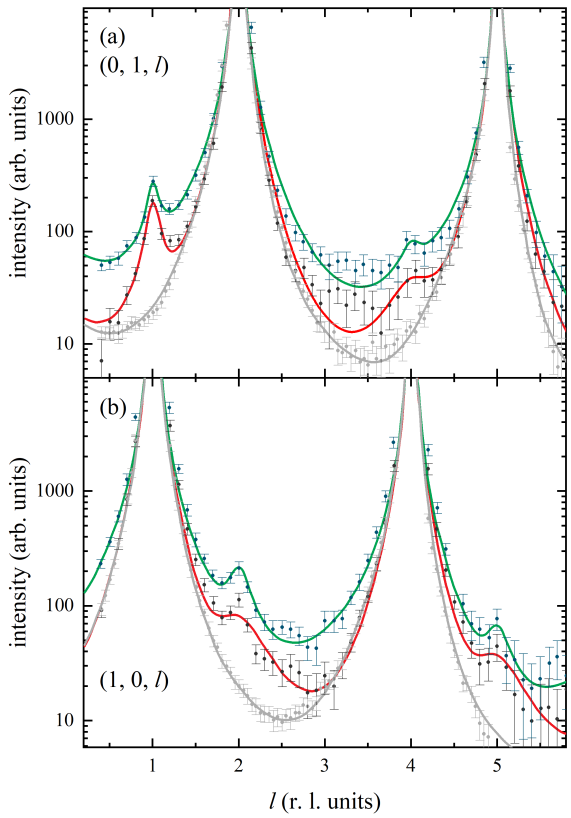

Fig. 5.7 Non-specular CTR data measured at -0.8 V (blue symbols) and -0.5 V (black symbols) presented with calculated fits to the data (green and red curves respectively) for a different Cu(111) sample preparation in 0.1 M phosphate buffer solution at pH = 8. Data in grey is the -800 mV CTR data from Figure 5.4, presented for comparison with the twinned data, in which additional peaks arise due to the presence of Cu nano-islands.

the oxygen pressure and the temperature, following three processes: growth from step edges, in-terrace growth from vacancy islands and growth of on-terrace oxide. The CTR data shown in Figure 5.7 exhibited additional scattering peaks at $(0,1,1)$ and $(0,1,4)$ on the $(0,\ 1,\ l)$ CTR, at the anti-Bragg positions, as well as at the $(1,0,2)$ and $(1,0,5)$ anti-Bragg positions on the $(1,\ 0,\ l)$ CTR. These features arise due to stacking faults induced by the nucleation of copper atoms into *hcp* sites on the surface. This leads to regions of the surface in which the stacking occurs in the reverse direction. A surface which exhibits regions with stacking in both directions is known as being twinned. The data was modelled by superimposing intensity at the anti-Bragg positions with a Lorentzian line-shape in addition to CTR intensity due to the Cu(111) surface. The intensity and peak widths of the Lorentzian peaks were varied to obtain a good fit to the data from the twinned surface, as opposed to modelling the data as a smooth surface with stacking faults. This indicates that the peaks arise due to nano-crystalline copper islands present at the Cu(111) surface. A simple model of the surface was found to be sufficient for fitting the data, with surface roughness and relaxation of the Cu surface, with no oxygen layer included in the calculation. Adjusting the surface roughness parameter in the model affects the intensity across the l range, and the Cu layer relaxation affects the intensity close to the Bragg peaks. The additional peaks due to surface twinning dominated the intensity between Bragg peaks, meaning that the effects of adjusting the coverage of atomic layers or including oxygen in the model were not discernable.

Parameters used to fit a model to the CTR data from the twinned Cu(111) surface at electrode potentials between -0.8 V and -0.5 V are presented in Figure 5.8. The potential dependence of the surface roughness, represented by the β factor is shown in Figure 5.8a and the relaxation of the first and second atomic layers of Cu is shown in Figure 5.8b (blue and green points respectively). During the positive potential sweep (blue/green points), a similar trend was indicated by these results as for the non-twinned sample, with roughness increasing as potential was stepped positive from -0.8 V to -0.5 V. A schematic diagram representing the surface structure changes is shown in Figure 5.9 (for a region of the surface without nano-islands). Interestingly, the β roughness factor at -0.8 V for the twinned surface was found to be lower than that for the surface without copper nano-islands on the surface. This could be explained by the copper nano-islands acting as nucleation sites for copper ad-atoms, decreasing the long-range surface roughness by virtue of regions of the surface with no nano-islands having lower roughness. The short-range roughness would be much higher though due to the nucleation of Cu into these nano-islands. When the applied potential was stepped back negatively (red points) the roughness was higher at -0.7 V and -0.8 V than prior to the application of more positive potentials. This indicates an irreversible change in surface roughness on this sample surface. This change was accompanied by a decrease in

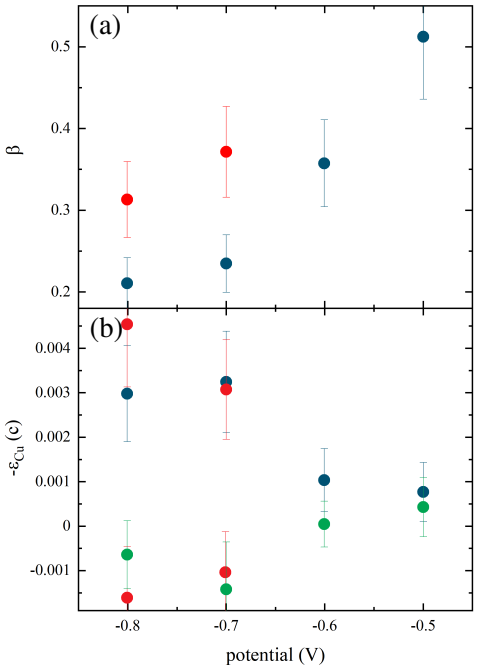

Fig. 5.8 Model parameters used to fit the CTR data in Figure 5.7 are shown as a function of potential. (a) The roughness of the surface as modelled through a β roughness factor. (b) The relaxation, $-\varepsilon_{Cu}$ of the 1st Cu layer (blue points) and the 2nd Cu layer (green points). Red points in (a) and (b) represent the data measured after the potential had been stepped to the positive limit.

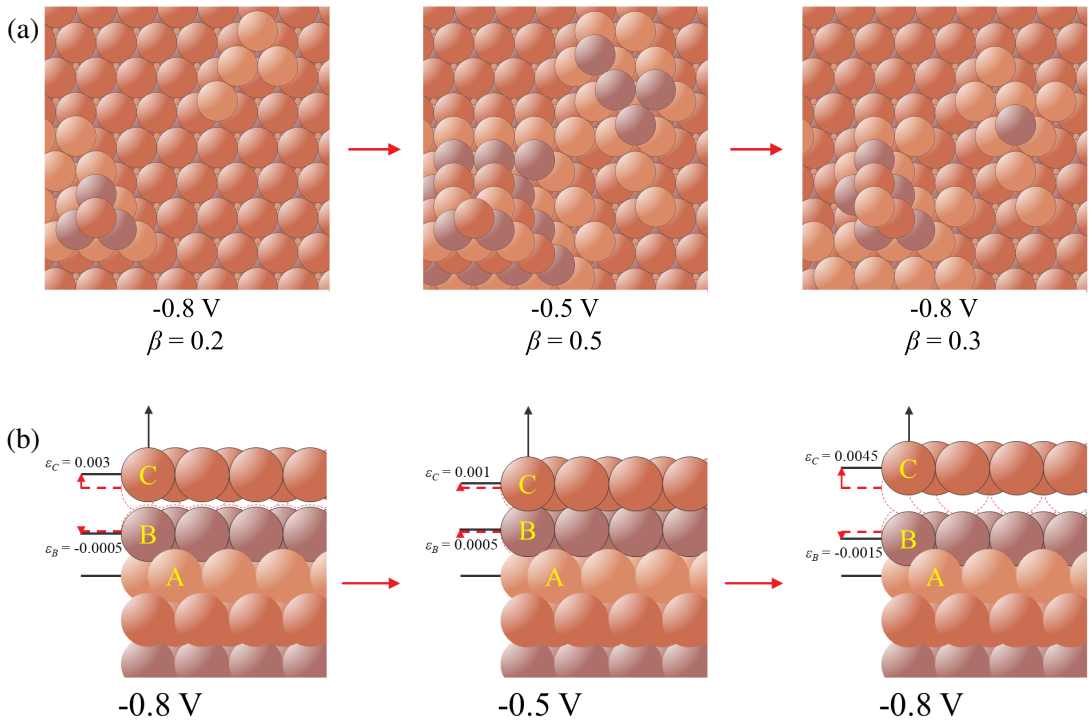

Fig. 5.9 Schematic diagram showing the structure changes observed at a region of the twinned Cu(111) surface as the potential was stepped from -0.8 V to -0.5 V and back again. The surface roughness as modelled by a β-model is shown for each electrode potential (β), along with the out-of-plane expansion is shown for the first (ε_C) and second (ε_B) Cu layers. (a) shows the observed change in roughness in the surface plane of the top Cu layer (b) illustrates the changes in out-of-plane position of the Cu atomic layers, showing the expansion and relaxation of the top two Cu layers.

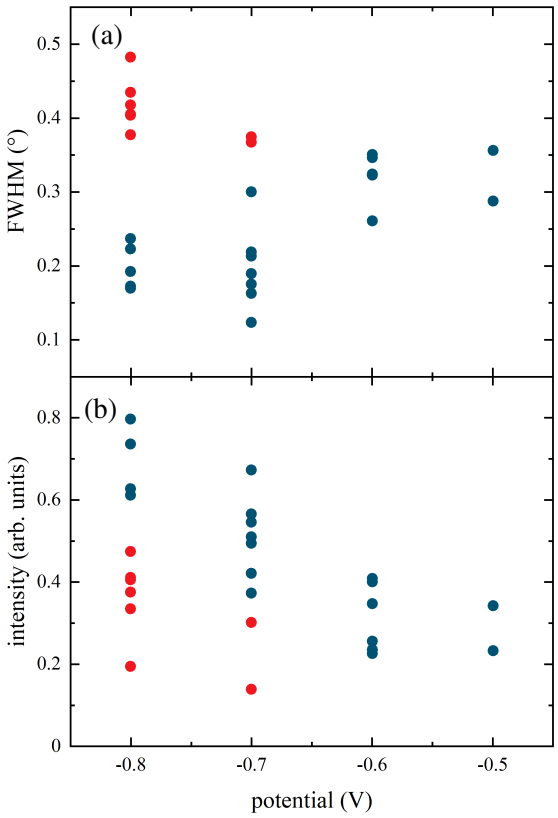

Fig. 5.10 The (a) full width half maximum (FWHM) and (b) integrated intensity of x-ray rocking scans measured at the $(0,1,0.5)$ non-specular CTR position with respect to applied electrode potential for the Cu(111) sample which exhibited additional peaks in the CTR data (Figure 5.7) over the course of the experiment. Blue points were measured while stepping the potential from -0.8 V to -0.5 V and red points from -0.8 V to -0.7 V.

surface domain size, and an increase in the size of the nano-crystalline copper domains on the Cu(111) surface, as evidenced by the widths of rocking scans at the $(1,0,5)$ anti-Bragg position and the widths of the Lorentzian line-shapes in the CTR measurements respectively.

The full width half maxima (FWHM) of rocking scans measured at the $(1,0,5)$ anti-Bragg position throughout the experiment on the twinned Cu(111) sample surface are shown in Figure 5.10a, with respect to the electrode potential. The intensities of the rocking scans are shown in Figure 5.10b, where it can be seen that the intensity decreases as the potential is stepped positive from -0.8 V to -0.5 V. This is similar to the behaviour exhibited by the non-twinned sample, shown in Figure 5.3, however, the intensity in Figure 5.3 increased when the potential was stepped back to -1 V, indicating a reversible process. This was not the case for the twinned sample: the intensity remained at the same level despite holding

the electrode potential at negative potentials (red points). The decrease in intensity for the twinned sample (Figure 5.10a) is accompanied by an increase in FWHM, from 0.2 ° to 0.4 ° which is also unaffected by stepping the potential back to -0.8 V and -0.7 V. This change in rocking scan width corresponds to a change in the domain size of the surface of ∼100 nm to ∼50 nm. The widths of the Lorentzian line-shapes due to stacking faults at anti-Bragg positions in the CTR data (Figure 5.7) are related to the height D of Cu nano-clusters by:

$$D = \frac{2\pi}{\Delta Q_z} \tag{5.1}$$

D was found to increase over the course of the experiment from 20 nm to 40 nm. The irreversibility of the process and the decrease in domain size accompanied by growth of Cu islands indicates that the Cu(111) sample surface when prepared by this method was unstable during potential cycling.

5.3.3 Discussion

It is clear from the results obtained by preparing the Cu(111) sample by the two different methods detailed above, that differing surface behaviours of the Cu(111) surface in phosphate electrolyte solution may be observed. These contrasting behaviours are dependent on the initial surface morphology and defect density, due to the method of sample preparation (specifically the electropolishing of the Cu(111) surface and the swift transfer thereafter into electrochemical conditions in the x-ray cell). In both the cases, a structural transition was observed at -0.6 V, which coincides with a peak in the anodic potential scan (Figure 5.1b). At potentials negative of this transition, the coverage and relaxation of atomic copper layers at the surface remained stable and constant with changing potential, with the roughness of the surface decreasing along with increasingly positive electrode potential. At potentials positive of -0.7 V the structural transition involved an increasing surface roughness and adsorption of oxygenated species, with a mixed layer of copper-oxygen forming at more positive potentials (-0.5 V). Along with this structural change, an inward relaxation of the top atomic Cu layer and an outward relaxation (expansion) of the second Cu layer was also observed, as shown in Figure 5.5b and 5.9b.

The structural transition evidenced by the surface x-ray diffraction investigation was identified in the cyclic voltammetry results as an anodic peak with a shoulder, indicating that the oxygen adsorption process occurs via two steps. Evaluating the charge under the anodic and cathodic peaks in the CV finds that 0.2 electrons were transferred per surface atom during the process. The surface coverage of the oxygen adlayer at the positive potential (-0.5 V) was determined by modelling the CTRs to be θ_O = 0.6 (60 % of a monolayer).

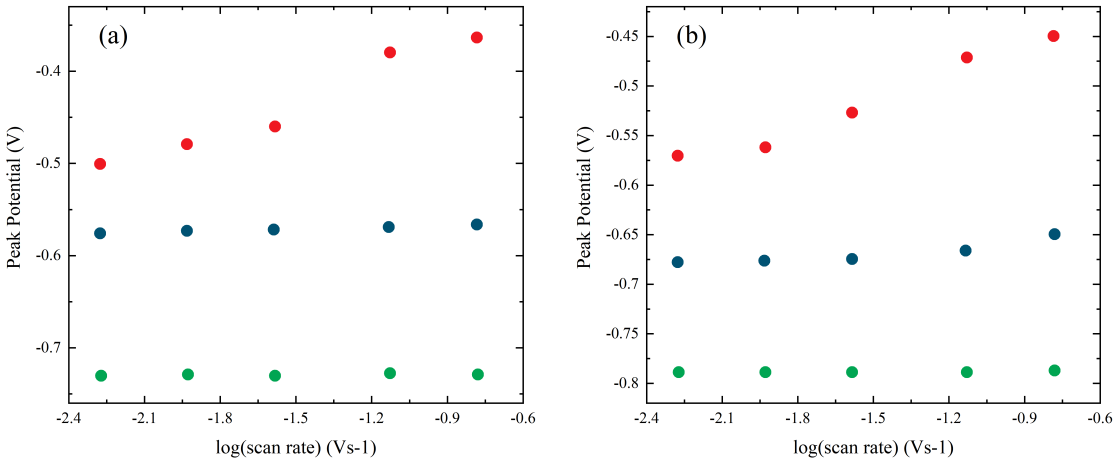

Fig. 5.11 Peak potentials from cyclic voltammograms as a function of the log of the scan rate for Cu(111) in phosphate buffer solution with (a) pH = 6 and (b) pH = 8. Blue and red points correspond to the 1st and 2nd anodic peaks (a_1 and a_2 in Figure 5.1) respectively and the green points correspond to the cathodic peak (c_1 in Figure 5.1).

The P-O bond lengths within phosphate species are known to be $d_{P-O} \sim$ 1.5-1.6 Å, with oxygen atoms separated by a distance of $d_{O-O} \sim$ 2.44-2.62 Å[115–117]. This distance is comparable with the distance between copper atoms at the Cu(111) surface, 2.556 Å, meaning that the adsorption of phosphate or hydrogen phosphate is likely to occur with 3 oxygen atoms occupying the surface hollow sites. Therefore, the adsorbed species at -0.5 V may be either phosphate, hydrogen phosphate but dihydrogen phosphate is ruled out, as dihydrogen phosphate ions have a different O-O distance. The exact nature of the phosphate species and adsorption process is not fully understood, however according to analysis of the CTR data at -0.6 V, there is a change in both oxygen coverage, θ_O and relaxation of the adsorbed oxygen layer, as well as changes in the relaxation of the top two copper layers between -0.6 V and -0.5 V (Figure 5.6). These differences indicate that an intermediate structure is formed at -0.6 V, which the XRV data in Figure 5.2 also suggests.

Further cyclic voltammetry measurements were carried out on the Cu(111) surface in 0.1 M phosphate solution at pH = 6 and pH = 8 at various scan rates. The positions along the potential scale of the 3 peaks (a_1, a_2 and c_1 in Figure 5.1) are shown as a function of the logarithm of the scan rate in Figure 5.11. In both pH = 6 and pH = 8, the peak positions of the cathodic peak (green points) and the first anodic peak (black points) were not found to be dependent on the scan rate, which indicates a fast adsorption process. The second anodic peak (red points) was observed to be dependent on the scan rate, with a gradient of $\sim$ 0.12 V / log(scan rate) (where scan rate was in units of V s^{-1}) in both pH = 6 and pH = 8

electrolyte solutions, suggesting that the peak corresponds to a slow process. As the cathodic peak and the first anodic peak are fast processes, but the second anodic peak is a slow process, the process associated with the second anodic peak will determine the overall rate of the adsorption process. The structural characterisation of the surface revealed that a significant rearrangement of the atomic structure accompanied this process, with the x-ray voltammetry data showing a clear hysteresis, which is indicative of a slow mass transfer occurring. The CTR data indicated that phosphate/oxygen is incorporated into the surface structure, forming a mixed copper-oxide, with the process accompanied by an increase in surface roughness at positive potentials. Studies in alkaline electrolyte solutions have shown other structural rearrangements of the Cu surface layer with slow kinetics, in which case a single Cu(I) oxide layer was formed and the Cu atomic density decreased by 30 % [118–120].

The relative proportions of hydrogen phosphate $[HPO_4]^{2-}$ and dihydrogen phosphate $[H_2PO_4]^-$ ions in the solution may be determined using the acid dissociation constant, $pKa([H_2PO_4]^-/[HPO_4]^{2-}) = 7.2$, with the proportions being 94 % and 6 % respectively in pH = 8 phosphate solution and 13 % and 87 % respectively in pH = 6. Studies of gold and platinum electrode surfaces have shown the adsorbed phosphate species to be dependent on pH and potential [121, 122], however on copper surfaces, phosphate dihydrogen has been found to adsorb for acidic electrolyte solutions ($pH < 5$) but not in alkaline solution ($pH > 9$) [123]. The adsorption of dihydrogen cannot be totally ruled out on this basis during the first anodic process, but the fact that the two adsorption steps were observed in the CV data for both pH = 6 and pH = 8 electrolyte solution, with no difference evident in the kinetics of the processes, suggests that the adsorption process occurred through a similar mechanism. The bonding between oxygen in the phosphate ion and copper was found to be more covalent that the bonding for silver and gold surfaces [123] which could lead to the atomic rearrangement and slow mass transport observed by the x-ray techniques.

The results from the both the structural characterisation and the electrochemical characterisation of the Cu(111) surface in phosphate electrolyte solution suggest that the adsorption mechanism involves two steps: the first anodic peak observed in the cyclic voltammograms is associated with an adsorption of hydrogen phosphate at the surface, either directly or by deprotonation of dihydrogen phosphate (depending on the pH). This is supported by the structural data which found a small amount of oxygen undergoing specific adsorption into the three-fold hollow sites on the Cu(111) surface. The second anodic peak corresponds to the deprotonation of the hydrogen phosphate and adsorption of phosphate anions which form a strong bond with the Cu surface, leading to an atomic rearrangement in which three oxygen atoms from the phosphate are adsorbed into the surface Cu layer. This process is entirely

reversible, which is confirmed by the electrochemical characterisation which found equal charge under the peaks in the anodic and cathodic cyclic voltammetry curves.

With this information on the adsorption processes at the Cu(111) surface, the differences in surface stability exhibited by samples prepared by different methods may be further explained. The surface morphology can be described by three properties discernible by surface x-ray diffraction: the domain size of atomic terraces at the surface, the presence of copper nano-islands and the surface roughness. The overall atomic roughness is quantified by the β-model and also known as the surface rugosity. The data in Figures 5.3 and 5.6 showed that even though the domain size (related to the FWHM) remained unchanged, the rugosity changed with potential. The surface that exhibited a reversible adsorption process in which phosphates and oxygen were incorporated into the surface structure had a greater rugosity over the potential scale than another surface, which had lower rugosity and showed evidence of copper nano-islands at the surface. The surface with initially lower rugosity was found to degrade with the potential driven phosphate adsorption/desorption process. Room temperature studies of the oxygen induced reconstruction of the Cu(111) surface have shown the formation of a disordered overlayer with O and Cu atoms sitting at different heights in the surface [124]. It has been proposed that the formation of this disordered overlayer favours the oxygen diffusion on Cu(111), leading to fast nucleation of many oxide islands. It is proposed that a similar process occurs in electrochemical conditions through the oxygen atoms in the adsorbed phosphates.

In the cases of both surface morphologies, the rugosity increases with the adsorption of phosphates. The differences in stability between the surfaces are attributed to the surface defects, which may act as nucleation sites for Cu ad-atoms which are created during the incorporation of phosphate ions into the Cu surface layer. In the case of copper nano-islands already being present on the surface, this could lead to growth of the islands, with further ad-atoms being incorporated into the nano-crystals at the surface. This would lead to roughening and a further decrease in the domain size of the surface, characteristics of the unstable Cu surface. In contrast, for the higher-rugosity surface which exhibited reversibility of the adsorption process and more stability, no preferred nucleation sites exist for the Cu ad-atoms, meaning that copper nano-crystals do not form.

5.4 Conclusions

In this investigation, electrochemical and surface x-ray diffraction data was obtained for the adsorption of phosphate onto Cu(111) single crystal electrode surfaces. The underlying mechanism of the phosphate adsorption and deprotonation of the dihydrogen phosphate was

accompanied by a roughening of the Cu surface. Roughening of the Cu surface through formation of a mixed copper-oxygen layer was reported, with oxygen atoms from the adsorbed phosphate species being incorporated into the surface Cu layer. The importance of the Cu surface preparation method and history of the electrode was found to be significant for the stability of the surface and the potential dependence of the surface rugosity. The presence of Cu nano-islands at the Cu surface was found to lead to 3D nucleation and growth of the nano-crystals under potential cycling which lead to irreversible changes in the surface morphology. The results demonstrate the importance of the sample surface preparation method for copper catalysts, as this will significantly affect the stability of the catalyst under operation conditions for the electrochemical CO_2 reduction reaction. It is important to avoid the twinned surface that exhibited Cu nano-islands, as this was found to be unstable and not a representative example of a Cu(111) surface. Researchers aiming to obtain a Cu(111) surface sample for catalysis should take care to follow the preparation method outlined here, where the working electrode was immediately contacted at negative potential (-0.8 V) upon transfer into solution in the electrochemical cell in order to achieve the desired surface morphology. The incorporation of oxygen into the Cu surface from the adsorbate anion is also a process that could be relevant for the study of oxo-anions, such as sulphate, and their role in the stability of electrocatalysts during oxidation processes.

Chapter 6

Halide Ions and Lead at the Cu(001) Surface

6.1 Introduction

In this chapter, a novel experimental technique, resonant surface x-ray diffraction (RSXRD) is employed in the study of halide ion adsorption on the Cu(001) surface. The aim is to build upon previous studies of chlorine and bromine adsorption on Cu(001) by determining the adlayer structure formed by iodine on the same surface to further the understanding of halide ion adsorption processes on metal electrodes. Cl and Br superstructures on Cu(001) have proven to be model systems for investigation by RSXRD, with surface diffraction spectra obtained from these systems providing essential example data for the development of analysis methods for the technique [125–127]. Iodine adsorption on Cu(001) is proposed as another candidate for an ideal system to study and produce results for the development of programs to analyse RSXRD data. Iodine belongs to the same series (group 17, halogens) as Cl and Br, however its larger size means that it cannot as easily form the same $c(2 \times 2)$ adlayer superstructure that its fellow halogens exhibit on Cu(001). Hence, it is necessary to identify the iodine adlayer superstructure that forms at the Cu(001) surface, if the resonant diffraction data from the structure is to be modelled.

Underpotential deposition of lead on the Cu(001) surface in the presence of Cl ions is also investigated by RSXRD. Lead and copper have been shown to form an alloy in perchlorate-containing electrolyte with halide ions, which exhibits interesting electrocatalytic properties [128]. Pb adatoms on Cu are reported to significantly influence the catalytic activity for the CO_2 reduction reaction and suppress competing reaction channel. The presence of halide ions has been shown to improve the reversibility of the Pb UPD process, which also exhibits faster kinetics with Cl ions present [129]. The goal was to determine the surface structure changes that occur during the dissolution of the Pb UPD layer using surface x-ray diffraction.

Then, resonant SXRD measurements could be made in order to gain insight into changes in the charge distribution at the surface associated with the changing structure.

6.1.1 Resonant Surface X-Ray Diffraction

For a complete understanding of electrochemical processes at the solid-liquid interface, including the nature of bonding between adsorbates and the electrode surface, the charge distribution and transfer of electrical charge across the interface must be considered. Information such as the rate of charge transfer and the charge distribution at interfaces can provide insight into the reactivity of a specific electrode, which has significance for the employment of electrochemical systems in catalysis, electroplating and various energy technologies [127, 130]. The presence of adsorbates at the surface has a significant influence on the charge distribution in terms of the partial transfer of charge and electro-adsorption valencies [131–134]. Adsorbates may also be adsorbed non-specifically, with a full solvation shell, which affects the potential distribution at the interface. Many examples of the double-layer structure and composition influencing catalytic reactions have been previously reported [135, 83, 136–139], however directly probing the effects on the charge distribution at an electrode-electrolyte interface is challenging.

Most common techniques for probing the charge distribution of a material use electrons, such as x-ray photoelectron spectroscopy (XPS), and are primarily vacuum techniques. This is because XPS requires analysis of emitted photoelectrons that have not lost kinetic energy. Electrons lose energy easily when travelling through ambient or liquid media, making ambient XPS a difficult technique to employ for electrochemical samples [140–142]. Molecular dynamics or quantum mechanical calculations may be used to obtain an indication of the electron density and potential drop modification at the electrode surface in the presence of adsorbed species, and x-ray reflectivity and surface x-ray scattering can provide detail on the near range ordering of ions in solution [3, 143, 144]. X-rays avoid the challenges related to probing through liquid that are faced by electron techniques. Probing with x-ray absorption spectroscopy (XAS) allows measurement of the adsorption edge energy of atoms at the solid-liquid interface [145, 146]. The position of the adsorption edge along the energy spectrum for a specific element may be shifted, with the shift linked to the electronic configuration of the atom being probed [147, 148]. It is possible to combine x-ray spectroscopy and surface x-ray diffraction to select specific atoms with the diffraction conditions and scan the x-ray energy to obtain atom-specific spectroscopic information. This technique is known as resonant surface x-ray diffraction (RSXRD) and has been used to study Pt(111) electrodes with the aim of determining the chemical states of electrochemically formed anodic oxide monolayers and to probe the adsorption of carbon monoxide onto the Pt surface [149–152].

RSXRD is a relatively new technique, with the studies by Menzel *et al.* (in 2006) involving carrying out first principles calculations of the RSXRD signal from the specular CTR. Only the specular CTR was considered, with this method only allowing for qualitative comparison with the data. Menzel *et al.* provided a computational workflow for carrying out more quantitative analysis, which subsequently (in 2018) has been implemented in the FDMNES program [153, 154]. This program allows first principles simulations of RSXRD data [155].

Resonant surface x-ray diffraction can be used to probe charge transfer directly by selecting specific atoms with the diffraction condition. Different reciprocal space positions have specific diffraction contributions from the bulk and surface atoms. Spectroscopic information may be obtained by scanning the x-ray beam energy through specific adsorption edges and monitoring the diffraction signal. The signal is dependent on the electron density of the contributing atoms, so any changes in charge transfer may be detected by changes in the scattered intensity close to the adsorption edge of an atom [156]. The x-ray scattering intensity at a specific reciprocal space position depends on the spectroscopic response of the atoms that contribute at that position, and depends on the modification of the atomic form factor due to the change in electron arrangement at the interface.

The experiments detailed in this chapter were motivated by the desire to understand the charge transfer between the metal electrode and adsorbing species and the nature of the bonding. The effects of applied potential and screening by the electrolyte is another question which RSXRD studies may be able to answer. In order to carry out a RSXRD experiment, it is important to determine the atomic structure first. This provides detail on the different atomic contributions at specific reciprocal lattice positions, so that the diffraction conditions may be used to select specific atoms to investigate spectroscopically. The atomic structure is also one of the inputs to the FDMNES program, and necessary for calculating the RSXRD model as part of full analysis of the data. RSXRD is strongly dependent on the polarisation of the x-ray photons, therefore controlling the polarisation during an experiment allows this dependence to be investigated, as the polarisation couples to the charge distribution in different directions.

The aim of this experiment was to use resonant surface x-ray diffraction to obtain details about the Cu(001) surface in the presence of halide ion adsorbates. Previous studies of Cu(001) with adsorbed Cl and Br ions in $c(2\times2)$ superstructures revealed a significant modification of the charge distribution of both the surface and sub-surface atomic metal adlayers when ionic bonds were formed at the surface [127]. In this chapter, surface x-ray diffraction is used to determine the structure of iodine on Cu(001) and preliminary RSXRD results are presented.

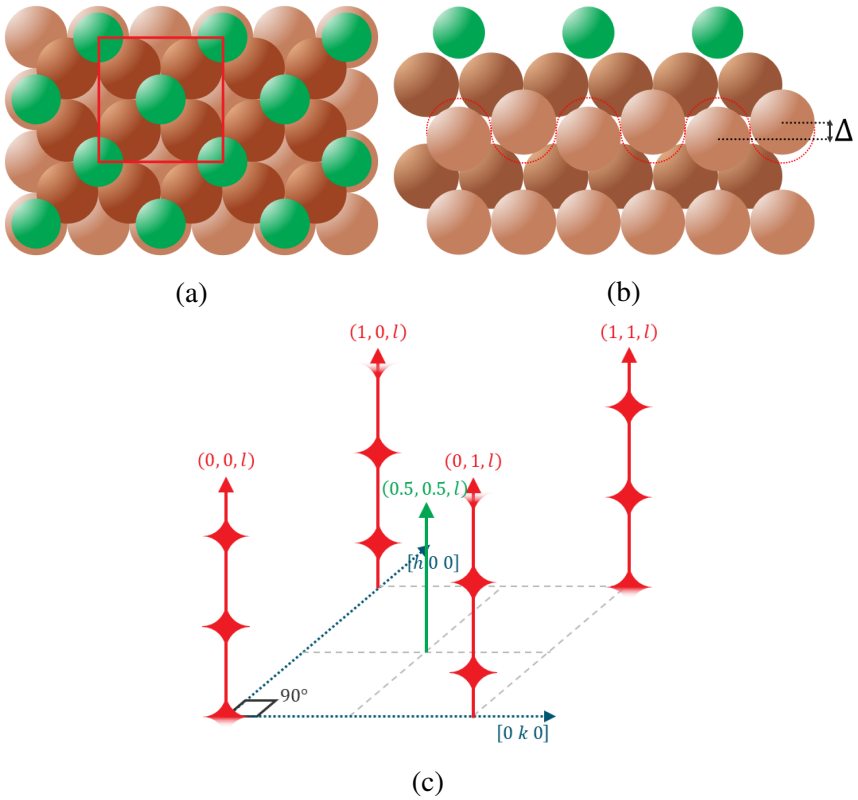

Fig. 6.1 The c(2×2)-Cl adlayer superstructure formed at the Cu(001) surface [126], with Cl ions shown in green atop the Cu substrate in (a) a top-down schematic, and (b) a side-on schematic. Subsurface buckling of the second Cu layer is highlighted by δ and red dotted lines show the positions of un-buckled Cu. (c) shows a reciprocal space map shown for the superstructure. A fractional order rod is shown in green at the $(0.5, 0.5, l)$ position. CTRs are shown in red.

6.1.2 Halide Adsorption on Cu(001)

Specifically adsorbed anions can affect the electrochemical reactivity of a metal electrode, which has implications for processes such as galvanic deposition, etching, corrosion and electrocatalysis. Metal UPD in the presence of halide ions, a reversible process for structure formation, has been widely studied, showing that the halide ions are useful for stabilising UPD monolayers [157–159]. Anion adsorption on UPD Cu monolayers has been studied by surface x-ray diffraction, showing that the bonding mechanisms differ in ultra-high vacuum (UHV) and the electrochemical environment for the same halide adsorption process and structure [29]. These studies showed that the bonding of the halide adlayer is determined by the chemical nature and reactivity of the first atomic layer of the metal substrate (the amount of UPD Cu that was present on the Au electrode). RSXRD is a viable technique

for investigating the charge distribution and hence determining the chemical driving force behind the changes in halide layer structure [160].

The use of RSXRD is still in the early stages, and therefore model systems are sought to establish the application of the technique and provide data for the development of the FDMNES program [155]. Halide adsorption on Cu(001) is an example of such a model system, with Cl and Br adsorption on Cu(001) surfaces having been studied in detail. Surface x-ray diffraction studies have shown that Cl and Br both form c(2×2) superstructures on Cu(001) [125, 126], and the Cl adlayer structure is illustrated in Figure 6.1. This adlayer superstructure gives rise to scattering features in the reciprocal space map that are described as fractional order rods. The fractional order rods due to the c(2×2) superstructure appear at $(0.5, 0.5, l)$ and other symmetric positions, and are shown in a reciprocal space map for the surface in Figure 6.1c. Previous studies have indicated that the presence of solvent molecules and the strong electric field play a significant role in the charge transfer process [29, 161, 126]. The c(2×2) halide superstructures are ideal electrochemical samples for investigation with RSXRD because the diffraction condition can be used to select different Cu atoms in the structure. This is due to the way that subsurface Cu atoms in the buckled 2nd layer contribute to the scattering at fractional reciprocal space positions where there is no diffraction signal due to the other Cu atoms in the surface or the bulk. Preliminary RSXRD measurements of the Cu UPD process on Au(001) in Br-containing perchloric acid have also been recently made.

In this experiment, the Cu(001) electrode surface is investigated in perchloric acid in the presence of I ions. The aim is to extend RSXRD measurements to directly probe the dependence on the applied electrode potential. The results will subsequently be analysed with FDMNES to obtain a detailed model of charge distribution in the presence of adsorbates with different electronegativities and at a range of potentials that are relevant to electroplating and energy technologies.

6.1.3 Underpotential Deposition of Lead on Cu(001)

The electrochemical deposition of Pb onto the Cu(001) surface is an example electrochemical system where alloy formation, stability and rearrangement of the atomic structure may be studied. Using RSXRD, the electronic structure changes associated with such processes may be probed. Individual atoms may be selected by the diffraction conditions to compare the charge distribution local to different atoms in the structure [155, 127].

UPD Pb layers on Cu have been shown to be useful electrochemical systems in catalysis, with Pb adatoms on Cu supports having been shown to suppress competing reaction channels during CO_2 electroreduction [128]. Elucidating the role of individual elements in the

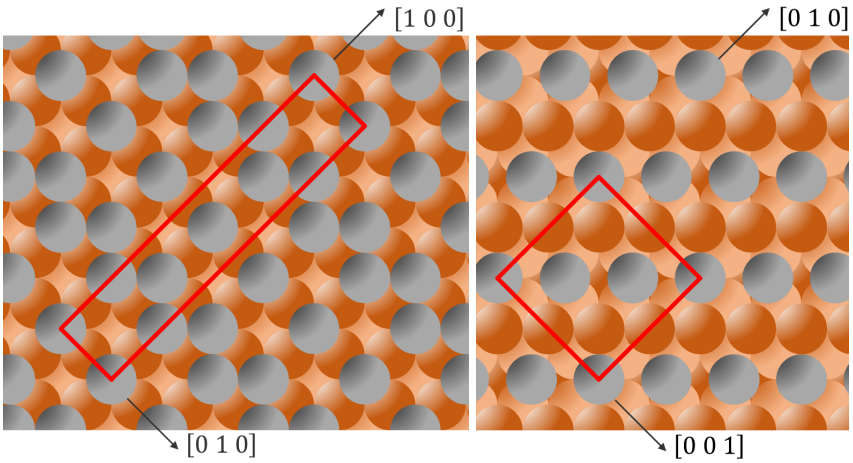

Fig. 6.2 Top-down schematics showing the (a) $c(5\sqrt{2} \times \sqrt{2})R45°$ and (b) $c(4 \times 4)$ UPD Pb structures on Cu(001) reported in the literature [164, 165]. The grey spheres represent Pb atoms and the other spheres represent Cu atoms.

processes that accompany Pb UPD on Cu(001) and the resulting electron density distribution is a key step in the rational design of functional catalytic materials.

The activity of a catalyst in an electrochemical reaction is linked to the bond strengths of the intermediate species of the reaction, according to the Sabatier principle [162]. The strength of the bonding is determined by the electronic structure of the electrode surface, related to the d-band centre [163]. The catalytic activity can be predicted by theoretical modelling of the electrochemical interface using density functional theory (DFT) and molecular dynamics. However, these methods require variables such as ion solvation of species in solution and adsorbates, and ordering of water dipoles and ions at the interface, which affect the interfacial potential distribution and therefore the electronic structure. Resonant surface x-ray diffraction is an alternative to these methods which can be used to understand alloy formation, catalytic activity and structural rearrangement in terms of the atom-specific structure.

RSXRD can be applied to the deposition of Pb on Cu(001) surfaces to investigate the reversible and widely studied Pb UPD process. Studies of lead UPD by Brisard *et al.* have shown that it is a kinetically slow process, as voltammograms show a separation between the adsorption and desorption peaks [129]. The peaks would appear at closer potentials if the process occurred quickly. However, the study showed that in the presence of Cl ions, the process occurred with faster kinetics and exhibited improved reversibility. In acid perchlorate electrolyte solution, an alloying/dealloying process has been observed at negative potentials as the UPD Pb coverage increases [166, 167]. This process is followed by the formation of a

c (2×2) phase with coverage of 0.5, and subsequently the insertion of antiphase boundaries to form a $c(5\sqrt{2} \times \sqrt{2})R45°$ overlayer with a coverage of 0.6. A schematic diagram of this atomic structure is shown in Figure 6.2a, with grey spheres representing Pb atoms and all other spheres representing Cu. This is the maximum coverage structure that may form on Cu(001), before bulk deposition of 3D islands begins.

The maximum coverage for a UPD monolayer of Pb on Cu is limited by the size of the atoms, which are much larger than Cu atoms. The Cu atomic radius is 128 pm whereas the Pb atomic radius is 175 pm. Therefore, not every Cu surface site can be occupied by an adsorbed Pb atom. For the (111) surface, the maximum UPD Pb coverage is 0.56 [129] and the coverage of the UPD monolayer on Cu(001) is 0.6 [167].

The Pb monolayer is stripped from the surface as the potential is scanned from negative to positive, during which process an alloyed Cu-Pb structure forms and is subsequently displaced by a Cl adlayer in a c (2×2) structure (Figure 6.1c) at positive potentials. These surface alloys have been studied in UHV [167, 164, 165, 168, 169] and in solution.

Alloy formation during the UPD process for Pb on Cu(001) has been studied electrochemically and with STM experiments to determine the alloy structures [170]. The Cu_4Pb_3 alloy begins to form at Cu step edges and, as the UPD process progresses, a novel transient (3×4) phase of Pb adatoms forms. This is followed by a $c(4 \times 4)$ structure with coverage of 0.375. A representation of this UPD structure is shown in Figure 6.2b. These phases consist of close packed rows of Pb embedded into the rows of the Cu(001) surface, and the phases have been found to fluctuate, changing orientation and lateral position on a 100 ms timescale.

During the dealloying process, as the electrode potential increases, the $c(4 \times 4)$ structure is modified due to dissolution of some Pb atoms, before ribbon like structures appear in the STM images [170]. These mobile structures form networks with defined distances and have been shown to be domain boundaries in the c (2×2) Cl adlayer decorated with Pb atoms. As further stripping of the Pb occurs, isolated Pb atoms are diffused across the surface, attaching and detaching from the ribbons. This exhibited high mobility is an important factor in the use of Pb as a surfactant for Cu deposition.

This experiment aims to build upon the RSXRD study of halide adsorption on Cu(001) by investigating the Pb UPD process on Cu(001) in the presence of halide ions. By determining the surface structures formed at different points during the UPD process by CTR measurements, a resonant surface x-ray diffraction experiment can be planned. RSXRD measurements can be made at reciprocal space positions and electrode potentials where the atomic contributions to the scattering signal are known. The goal is to obtain RSXRD data

for these model processes that can be analysed with the FDMNES program in an attempt to directly link the electronic structure to electrocatalytic activity of the surface.

6.2 Experimental Methods

The Cu(001) single crystal working electrode surface (miscut < 0.1 °) was prepared by electropolishing for 10 s in 70 % orthophosphoric acid at 2 V against a high surface area copper mesh. The crystal was then rinsed in ultrapure water before being submerged in electrolyte solution and transferred swiftly to the x-ray electrochemical cell (described in more detail in Chapter 3.4), where a potential was immediately applied against the Ag/AgCl reference electrode. All potentials are quoted relative to this electrode, and the counter electrode in the three-electrode cell was made of either gold or copper wire, depending on the dataset. Experiments were carried out in 0.1 M $HClO_4$ + 10 mM KI electrolyte solution to characterise the iodine adlayer structure formed at the Cu(001) surface, and in 0.1 M $HClO_4$ + 0.01 M NaCl + 0.01 M $Pb(ClO_4)_2$ electrolyte solution to investigate the formation of the lead UPD adlayer at the Cu(001) surface. Solutions were prepared using 99.5 % KI, $Cu(HClO_4)_2$ and 98 % $PbCl_2$ solid reagents from Sigma Aldrich (now Merck KGaA, Darmstadt, Germany). Electrolyte solutions were purged with N_2 throughout the experiment to maintain a minimal level of O_2 in the system.

Structural characterisation of the Cu(001) surface in perchloric acid electrolyte solution in the presence of iodide ions was carried out by surface x-ray diffraction (SXRD). Potential dependent SXRD measurements were made to investigate the adlayer structure formed by adsorbed I^- ions at the Cu(001) surface. The experimental procedure followed for the structural characterisation was similar to that detailed in Chapter 4 and established by Lucas, Marković and co-workers [48, 49]. In addition, resonant surface x-ray diffraction (RSXRD) was employed to obtain spectroscopic data while utilising the ability to select specific surface atoms by the diffraction conditions. The RSXRD procedure was similar to that followed in previous work by Gründer and Lucas [127] and involved measuring surface diffraction data from specific points in reciprocal space as the incident x-ray energy was scanned through an adsorption edge (e.g. the Cu K-edge at 8.9789 keV [171]).

Experiments were conducted at the I16 beamline at Diamond Light Source, Oxfordshire, UK [41], where the Cu(001) surface was investigated in two electrolyte solutions: 0.1 M $HClO_4$ + 10 mM KI and 0.1 M $HClO_4$ + 0.01 M NaCl + 0.01 M $Pb(ClO_4)_2$. Both a structural characterisation by SXRD and spectroscopic investigation by RSXRD were carried out on the two electrochemical systems using the I16 beamline. Additional data was obtained for the Cu(001) surface in 0.1 M $HClO_4$ + 10 mM KI electrolyte solution at BM28, the

XMaS beamline at the ESRF, Grenoble, France [43], with resonant measurements as well as structural characterisation of the surface recorded.

Resonant surface x-ray diffraction measurements involve scanning the incident x-ray energy while keeping the vector **q** constant. Measurements are made for x-rays polarised in two orientations: parallel to the surface normal and perpendicular to the surface normal. For some experiments at I16, a diamond phase plate was employed to flip the polarity of incident x-rays, so that the diffractometer geometry could be kept the same throughout the experiment. For other experiments at I16 and the experiment conducted at BM28, two different geometries were employed: horizontal and vertical. The horizontal geometry is defined as that in which the **q**-vector is parallel to the polarisation of the x-ray beam where for in-plane positions (at low l) the polarisation of the beam being perpendicular to the surface normal. When the diffractometer is set up in vertical geometry, the **q**-vector is perpendicular to the polarisation of the x-ray beam and for in-plane positions (at low l) the polarisation of the beam is parallel to the surface normal. As well as the resonant diffraction signal from the working electrode surface, the x-ray fluorescence signal was recorded in parallel, which allowed the exact position of the Cu-K edge to be identified in the energy spectrum.

The Cu(001) crystal surface, as described in Section 2.4.2, has a square structure, and was indexed to a surface tetragonal unit cell (the relation of which to the conventional cubic unit cell is also provided in 2.4.2). The $[0\ 0\ l]$ direction is defined along the surface normal and the units of h, k and l are given by

$$\mathbf{b}_1 = \mathbf{b}_2 = \frac{2\pi}{a_{NN}} \quad \text{and} \quad \mathbf{b}_3 = \frac{4\pi}{\sqrt{2}a_{NN}} \tag{2.41}$$

where the nearest neighbour distance for copper is $a_{NN} = 2.556$ Å.

6.3 Results and Discussion

6.3.1 Structural Characterisation of Iodine Adsorption on Cu(001)

Following on from previous studies of the c(2×2) Cl and Br adlayer structures that form on the Cu(001) electrode surface under electrochemical conditions, an experiment was carried out to investigate the formation of an I adlayer on the Cu(001) surface and the structure that may form. A Cu(001) single crystal surface was submerged in 0.1 M $HClO_4$ + 10 mM KI electrolyte solution and the potential was held at -0.6 V to form the halide adlayer structure that was hypothesised. As both Cl and Br have been shown to exhibit similar behaviours, with

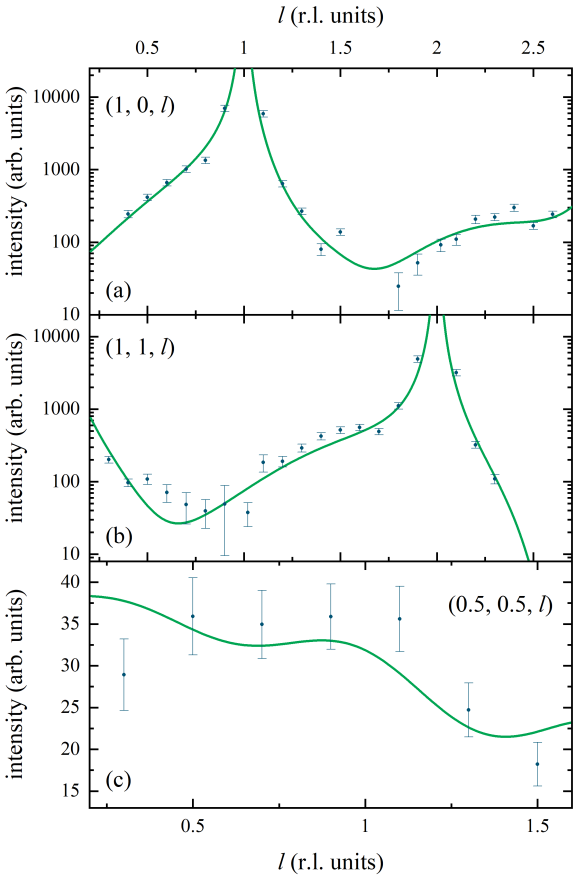

Fig. 6.3 Fitted CTR data measured for the Cu(001) surface in iodine electrolyte. The (a) $(1,0,l)$ and (b) $(1,1,l)$ CTRs and (c) $(0.5,0.5,l)$ fractional order rod are shown. Blue points with error bars show x-ray intensities at -0.6 V, with the calculated fit to the data also shown (green curve) from a modelled Cu(001) surface with adsorbed iodine in a c(2×2) superstructure. Data measured at I16 beamline, Diamond Light Source

halide superstructure adlayers forming on Cu(001) surfaces at negative electrode potentials, it is thought likely that a similar effect may occur with iodine at such potentials. SXRD measurements were made at surface-sensitive reciprocal space positions on CTRs, as well as a fractional order rod that is sensitive to a c(2×2) superstructure, in order to determine the structure formed by I ions at the Cu(001) surface. The aim is to determine whether I will also form a c(2×2) superstructure, as formed by Cl and Br, on Cu(001). Monitoring the SXRD signal from the surface while scanning the x-ray energy through the Cu-K adsorption edge energy (at 8.9789 keV [171]) probes copper bonding and changes in the charge distribution. In a c(2×2) halide structure on Cu(001), the diffraction condition can be utilised to select the surface layer atoms, or the atoms in the buckled second Cu layer. However, the first step was to determine the surface structure formed by the Cu(001) surface with adsorbed iodine.

To determine the structure of the surface, SXRD experiments were carried out on the I16 beamline at Diamond Light Source and the XMaS beamline at the ESRF. At I16, the x-ray signal along the $(1,0,l)$ and $(1,1,l)$ crystal truncation rods (cubic units) and $(0.5,0.5,l)$ fractional order rod (shown in Figure 6.1c) was measured by performing rocking scans at intervals in l while holding the electrode potential at -0.6 V. Fitting the rocking scans (scanned through the sample rotation angle ϕ) with a Lorentzian line-shape and taking the area of each rocking scan peak allows the integrated intensity profile of the diffraction rod along the CTR direction to be determined. Modelling the structure and fitting the SXRD data allows the surface structure to be deduced. Figure 6.3 shows the CTR data (red points) with the fitted model (dark blue curve) for the Cu(001) surface in perchloric electrolyte with iodine ions at -0.6 V. Non-specular $(1,0,l)$ and $\left(1,\bar{1},l\right)$ CTRs and the $(0.5,0.5,l)$ fractional order rod are shown. A c(2×2) I superstructure model was fitted to the SXRD data, where the iodine is sitting in hollow sites on top of the surface Cu layer. The coverage of iodine in the c(2×2) I adlayer was determined to be $\theta = 0.29$ ($\pm$ 0.05) by fitting the SXRD data, indicating that 15 ($\pm$ 5) % of the surface sites on the Cu(001) surface are occupied by I.

The heights of atoms in the unit cell were varied in order to fit the data, finding that the vertical separation between the I adlayer and the topmost layer of Cu was 2.28 ($\pm$ 0.08) Å. The iodine adlayer was modelled with an associated rms displacement of 0.14 ($\pm$ 0.14) Å. From the result for the vertical separation between layers, the bond length between Cu and I in the structural model could be determined, giving a result of 3.1 ($\pm$ 0.1) Å. This result is greater than the value for the Cu-I bond length reported in the literature for Cu(I) iodide (2.338 Å) by around a third [172].

The topmost Cu layer underwent expansion by 0.16 ($\pm$ 0.03) Å away from its equilibrium out-of-plane position in a Cu(001) unit cell. The rms displacement of this Cu layer was found to be 0.25 ($\pm$ 0.05) Å, which is not unusual for a surface metallic layer. The second metal layer was modelled with a buckling of the Cu atoms, where Cu atoms directly below I atoms sit at a different out-of-plane position to those Cu atoms directly below unoccupied surface sites. To determine the amount of buckling, the CTR and fractional order rod data was fitted, with the results giving an expansion for the atoms sitting below iodine atoms of 0.01 ($\pm$ 0.05) Å towards the iodine atoms, and an expansion result for atoms sitting below unoccupied sites of 0.00 ($\pm$ 0.05) Å. The amplitude of this buckling was found to be 0.01 ($\pm$ 0.03) Å, which is comparable with the amplitude of buckling reported in previous studies for the c(2×2) structures of Cl and Br on Cu(001) (0.004 to 0.006 ($\pm$ 0.004) Å for Cl and 0.004-0.008 Å for Br depending on the electrode potential) [126, 125]. The results for the buckling are within a factor of two of the buckling reported for the Cu(001) in the

presence of adsorbed Cl or Br, which is reasonable and confirms a similar structure forms for I adsorption as that observed for Br and Cl adlayers on Cu(001).

The results were found to be consistent across the data obtained at the two synchrotron beamlines (I16 at Diamond Light Source and XMaS at the ESRF). Comparing the superstructure formed by iodine on with those formed by Cl and Br ions on Cu(001) surfaces, the amplitude of the buckling is around a factor of 2 more than that observed for Cl adsorption, and around a factor of 1.5 more than that reported for the Br c(2×2) structure. Comparing the atomic radii of Cl, Br and I, the amount of buckling appears to increase with increasing atomic radius of the adsorbed species, which is a notable trend. The SXRD data obtained for the Cu(001) surface in 0.1 M $HClO_4$ + 10 mM KI electrolyte solution supports the theory that halide ions (Cl, Br and I) all form similar adsorbate superstructures on Cu(001) surfaces, with c(2×2) periodicity.

6.3.2 Resonant SXRD Study of Iodine Adsorption on Cu(001)

Resonant SXRD experiments on Cu(001) in 0.1 M $HClO_4$ + 10 mM KI electrolyte solution were carried out at Diamond Light Source and the ESRF by monitoring SXRD signals as the x-ray energy was scanned through the Cu-K edge at negative electrode potentials, where the iodine superstructure is formed. RSXRD data was obtained for a wide range of reciprocal lattice positions on 4 CTRs.

For energy scans that were measured at the XMaS beamline, a point detector with a multichannel analyser was employed. Separate background measurements to obtain the fluorescence signal were obtained by moving one of the sample diffractometer motors by a small angle so that the surface diffraction signal did not illuminate the detector. The fluorescence could then be subtracted to attain the RSXRD data for reciprocal space positions on the CTRs and the $(0.5,0.5,l)$ fractional order rod. Data was gathered while holding the electrode potential at -0.5 V so that the iodine superstructure was present and four energy scans are presented in Figure 6.4. The energy scans shown in Figure 6.4 were measured at (a) $(0.5,0.5,0.2)$, (b) $(1,0,0.2)$, (c) $(0,0,0.8)$ and (d) $(0,0,1.8)$, with the experiments carried out in both vertical and horizontal scattering geometries. Blue points show RSXRD data measured with π-polarised x-rays, and the red points show the energy dependent surface x-ray diffraction signal when σ-polarised x-rays were employed. π-polarised x-rays are polarised almost perpendicular to the sample surface (at 90 - α °, where α is the angle the incident x-ray beam makes with the sample surface plane). σ-polarised x-rays are polarised parallel to the sample surface. Smoothed curves through the data are shown in red and blue and the Cu-K edge energy (8.9789 keV) is shown by the grey dotted line. Energy scale calibration has been carried out based on the known value for the Cu-K edge energy. A green

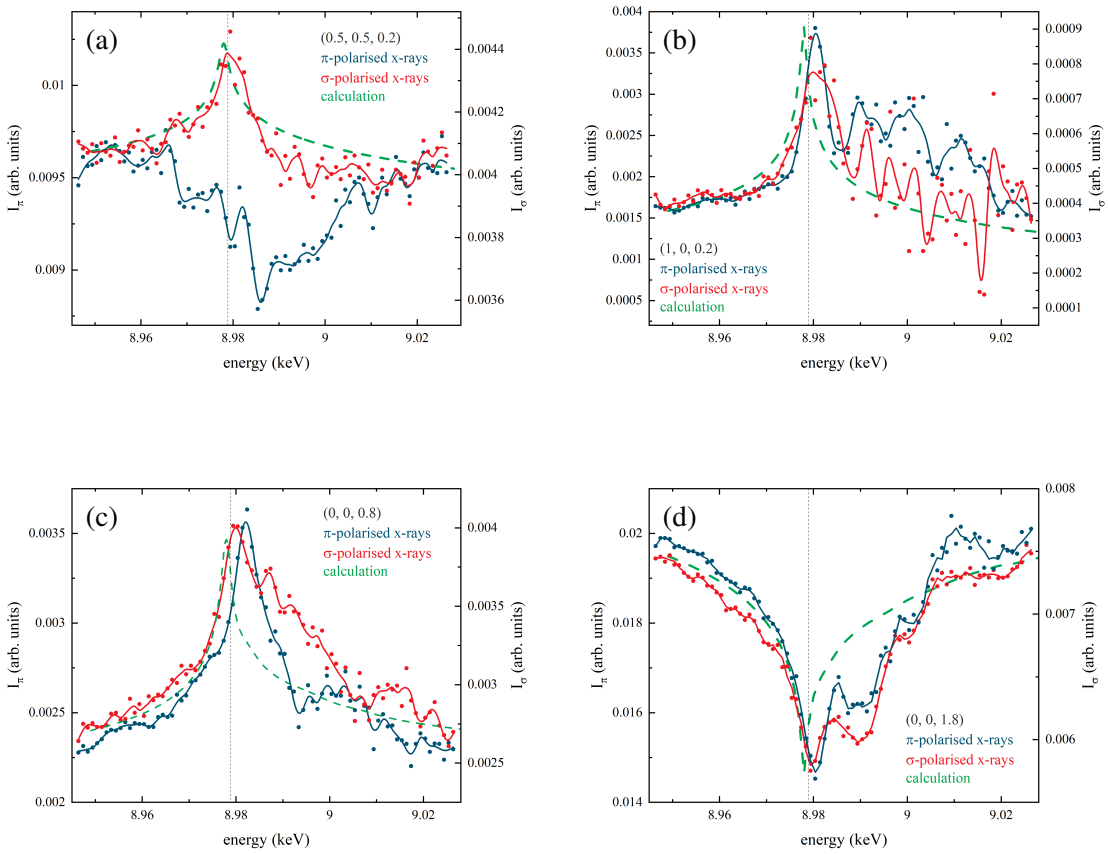

Fig. 6.4 Energy scans through the Cu-K edge measured for the RSXRD signal from Cu(001) in 0.1 M $HClO_4$ + 10 mM KI electrolyte solution at -0.5 V electrode potential. Energy scans are measured at the reciprocal lattice positions (a) $(0.5, 0.5, 0.2)$, (b) $(1, 0, 0.2)$, (c) $(0, 0, 0.8)$ and (d) $(0, 0, 1.8)$. Red points show the RSXRD signal, I_σ measured with σ-polarised incident x-rays. Blue points show the signal for π-polarised x-rays, I_π. Smoothed curves through the data are shown in red and blue. A calculation of the energy dependent intensity from a simple model of the surface is shown in green. The dotted dark grey line shows the position of the Cu-K edge (8.9789 keV).

dashed line shows a calculation of the energy dependence, from the model of the surface obtained by fit to the data in Figure 6.3, for comparison.

The diffraction signal from the $(0.5, 0.5, 0.2)$ fractional order rod position, sensitive to the c(2×2) superstructure, is shown in Figure 6.4a. The only Cu atoms contributing to this signal are those in the second Cu layer: the atom sitting below the iodine atom or the atom sitting below the empty hollow site on the Cu surface. These 2 Cu atoms sit at different heights due to the buckling in this layer of the Cu-I unit cell structure. It is clear from inspection of the graph that the peak in the π-polarised data (I_π) is significantly shifted with respect to the Cu-K edge energy and is negative in amplitude (a trough). The data measured in the horizontal geometry (σ-polarised x-rays) shows a peak that is not shifted from the Cu-K edge energy.

The π- and σ-polarised x-rays couple with the p_z or p_{xy} orbitals of the atoms respectively, when measuring non-specular diffraction in the vertical and horizontal experimental geometries. The σ-polarised data exhibits no peak shift in the signal with respect to the calculation of the energy dependence of the x-ray signal (green dashed line), indicating that there is no modification of charge distribution for the p_{xy} orbitals of Cu atoms in the buckled subsurface layer.

In contrast, the π-polarised data shows a trough in the x-ray signal that is also shifted to energies positive of the Cu-K edge. For π-polarised x-rays, the measurement couples with the out-of-plane charge distribution and the shift in Figure 6.4a arises due to a modification in the out-of-plane charge distribution (p_z orbitals of the Cu atoms in the buckled layer). This differs to the behaviour seen in the case of a Cl c(2×2) superstructure on Cu(001) [127], where a shifted peak was detected that was positive in amplitude. The charge distribution in the direction normal to the surface for Cu atoms in the buckled subsurface layer is clearly undergoing a modification in the presence of adsorbed iodine, and the effect is different to that previously reported in the presence of adsorbed chlorine, due to the opposite amplitudes of the Cu-K edge peaks that are observed for the two electrochemical systems.

Figure 6.4b shows the energy scan data measured from the $(1, 0, 0.2)$ CTR position. It can be seen that at this reciprocal space position, the data measured with both π- and σ-polarised x-rays exhibits a peak that coincides with the Cu-K edge energy at 8.9789 keV. The x-ray signal from this reciprocal space position (close to the anti-Bragg position at $(1, 0, 0)$) is sensitive to the Cu(001) surface, and Cu atoms in the top-most Cu layer contribute to the scattering. There is no buckling of the atoms in the top-most Cu layer, and the atoms in this layer experience no modification in the accumulation of charge in the p_z or p_{xy} orbitals.

Energy scans were also carried out at specular CTR positions and the data from the $(0, 0, 0.8)$ position is shown in Figure 6.4c. Due to the geometry of the experiment, for

measurements of reciprocal space positions on the specular CTR, the data obtained in horizontal geometry mode was sensitive to the charge distribution in the direction normal to the surface and in the p_z orbitals of surface Cu atoms. For specular measurements in vertical geometry, the x-rays were polarised parallel to the surface and therefore probe the charge distribution in the surface plane. This data is measured at a position on the CTR the same distance (in reciprocal lattice units) from an anti-Bragg position as that in Figure 6.4b.

The specular data measured in horizontal geometry (π-polarised) exhibits a shift of the peak in energy away from the Cu-K edge position, which is consistent with the shift observed at the $(0.5, 0.5, 0.2)$ superstructure-sensitive position, however the peak at $(0, 0, 0.8)$ was positive in amplitude. The σ-polarised data was not shifted with respect to the Cu-K edge energy. This data is sensitive to the atoms in the top-most Cu layer as well as the subsurface layers of Cu. The specular $(0, 0, 0.8)$ data appears to be in agreement with the findings of the $(0.5, 0.5, 0.2)$ data, that the charge distribution is modified in the direction normal to the sample surface in the presence of adsorbed iodine.

This could be due to differing charge distribution in the different atomic layers, which may occur in the presence of an electric dipole across the surface layers. The observation of such phenomena was recently reported for the Pt(111) surface in acidic electrolyte solution [173]. To fully understand and quantify the changes in charge distribution indicated by this data requires first principles calculations, which could be carried out with the recently developed FDMNES program [153–155].

By contrast, the data in Figure 6.4d was measured at a reciprocal space position close to a Bragg peak on the specular CTR, $(0, 0, 1.8)$. There is no clear difference in the data for the two x-ray polarisations at this position, or any shift indicating a modification in the charge distribution. This is to be expected, as at reciprocal lattice positions close to a Bragg peak, there is significant contribution to the diffraction signal from the bulk crystal. Therefore, this signal will be dominated by bulk Cu atoms, so little effect due to changes in the charge distribution close to the surface are discernable.

6.3.3 Structural Characterisation of Pb UPD on Cu(001)

In addition to studying iodine adsorption on Cu(001), an experiment was also carried out to investigate Pb underpotential deposition on Cu(001) in the presence of Cl ions with RSXRD. This electrochemical system was identified as a candidate for investigation by RSXRD as a continuation of RSXRD studies of halide superstructures on Cu(001). If the diffraction condition can be used to select atoms within the surface structure, then spectroscopic information may be obtained for Pb, Cu and Cl atoms in this system, depending on the surface structure formed.

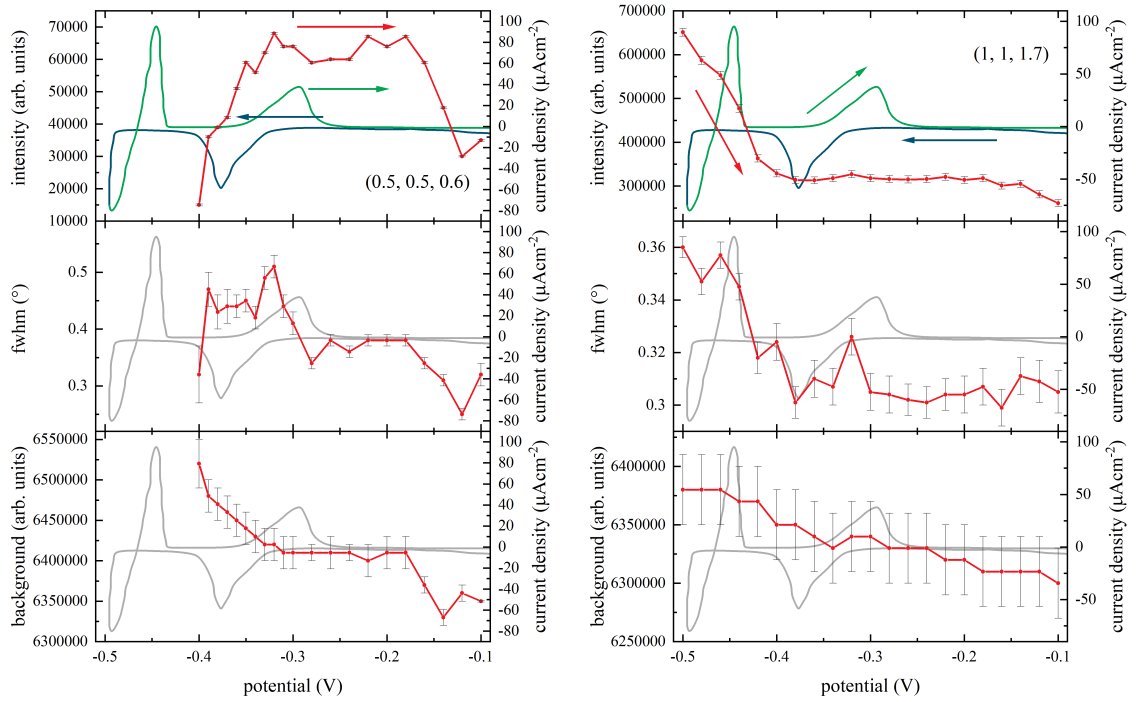

(a) (b)

Fig. 6.5 Stationary x-ray rocking scans carried out on the Cu(001) surface during dissolution of the UPD-Pb layer at the (a) $(0.5, 0.5, 0.6)$ and (b) $(1, 1, 1.7)$ reciprocal lattice positions as the applied potential was stepped from -0.4 V to -0.1 V. The red lines show the peak area (intensity), width (FWHM) and background intensity of the fitted x-ray rocking scans. The blue and green curves show CV measurements of the Pb UPD process on a different Cu(001) sample reproduced from a 1998 study by Moffat [166].

To study the structure changes during dissolution of the Pb UPD layer and the Cu-Pb alloying processes, a SXRD experiment was carried out on the Cu(001) surface in 0.01 M $HClO_4$ + 0.01 M NaCl + 0.01 M $Pb(ClO_4)_2$ electrolyte solution. In the presence of halide ions, Pb atoms and the Cu(001) surface have been shown to form a Pb_3Cu_4 surface alloy [170] and the surface structures and changes in structure during the alloying and dealloying process were investigated by SXRD. A detailed investigation of the potential dependence of the diffraction signal from two reciprocal lattice positions, on the superstructure rod and the CTR respectively, was carried out by performing rocking scans through these positions while holding the potential at steps through a potential window. The potential was stepped from -0.5 V to -0.1 V while monitoring intensity from the $(1, 1, 1.7)$ CTR position and stepped from -0.4 V to -0.1 V at the $(0.5, 0.5, 0.6)$ superstructure position. The peaks measured by rocking scans were fitted with a Lorentzian line shape using Py16, a data viewer and automated analysis program designed for I16 beamline users [174]. The integrated intensities of the rocking scans are plotted as a function of potential along with the peak width and background intensity in Figure 6.5 (red lines), with cyclic voltammetry curves [166] also presented (blue and green lines). The CV shown in Figure 6.5 is obtained from a different sample, reproduced from Moffat's 1998 study published in The Journal of Physical Chemistry B. The latter study investigated the Cu(001) surface in 0.01 M $HClO_4$ + 0.001 M NaCl + 0.001 M $Pb(ClO_4)_2$ electrolyte solution. The direction in which the potential was being stepped is indicated by an arrow in Figure 6.5.

The potential dependent rocking scans presented in Figure 6.5 show a change in diffracted x-ray signal from the $(0.5, 0.5, 0.6)$ and $(1, 1, 1.7)$ reciprocal lattice positions. Figure 6.5a shows that as the electrode potential is swept in the positive direction from -0.4 V to -0.3 V, the x-ray signal sensitive to the superstructure increases to a stable level from zero, as between -0.5 V and -0.4 V, no signal was discerned from the background noise. The plot indicates a peak in integrated intensity at around -0.32 V and another around -0.2 V, which could be due to structural changes during the dealloying process expected to occur over this potential range. At potentials more positive of -0.18 V, the diffracted signal from the surface superstructure drops slightly indicating a further structural change. Figure 6.5b shows the potential dependence of the integrated intensity measured from the $(1, 1, 1.7)$ CTR position, where the plot indicates a change in surface structure between -0.5 V and -0.4 V as the diffracted signal falls to a stable level, remaining at this level over the potential range from -0.4 V to -0.1 V. As the negative side of this potential window is that at which the Pb UPD layer is expected, this change in diffracted signal may be tracking the dissolution of the UPD layer and the structural changes that occur during that process.

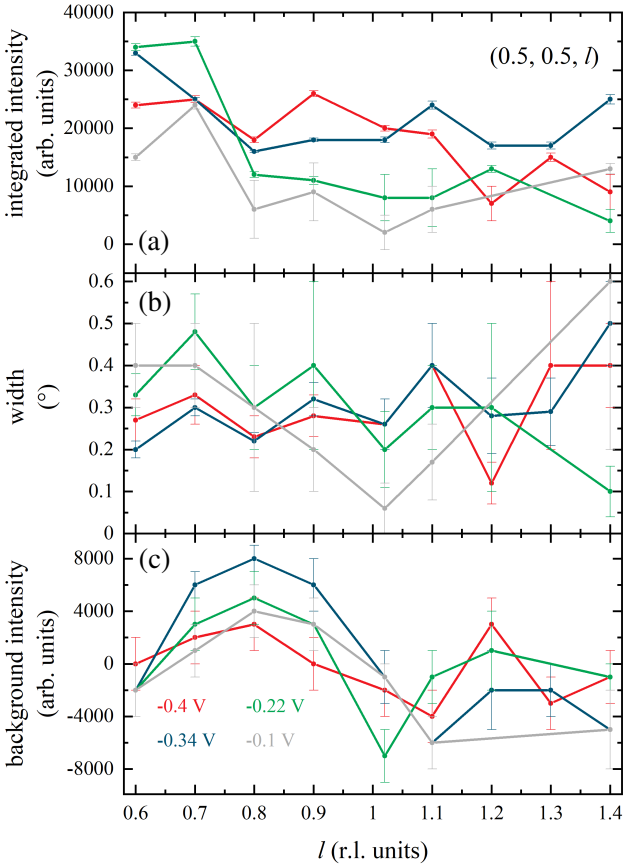

Fig. 6.6 Fit results from rocking scans carried out on the Cu(001) surface during dissolution of the UPD-Pb layer at reciprocal lattice positions along the $(0.5\ 0.5\ l)$ fractional order rod. (a) The integrated intensity of the fitted rocking scan peaks is shown for scans along the rod measured while holding the potential at -0.4 V (red), -0.34 V (blue), -0.22 V (green) and -0.1 V (grey). Also shown are (b) the peak width and (c) the background intensity level of fitted rocking scan peaks

The surface structure during the dissolution of the Pb UPD layer was investigated by performing rocking scans at reciprocal lattice positions along the $(0.5, 0.5, l)$ superstructure rod at different potentials. The diffracted intensity along $(0.5, 0.5, l)$ arises due to the superstructure formed on the surface (Figure 6.1c), as the bulk Cu(001) crystal and surface atomic layers do not give rise to CTRs at this in-plane position. The Cl ions in the electrolyte are known to form a c(2×2) superstructure on Cu(001), and this superstructure gives rise to intensity along the $(0.5, 0.5, l)$ fractional order rod. Also contributing to the signal are Cu atoms in the buckled second surface layer, which sit at different heights in the surface normal direction, depending on whether the atom sits below an adsorbed Cl ion or an empty surface site. The dissolution of the Pb UPD layer and its displacement at positive potentials by the Cl c(2×2) superstructure is expected over the potential window from -0.4 V to -0.1 V, as indicated by the structure changes at $(0.5, 0.5, 0.6)$ observed and presented in Figure 6.5, and monitoring the intensity profile along the $(0.5, 0.5, l)$ fractional order rod through this potential window is expected to provide detail of the process. Figure 6.6 shows the integrated intensity of rocking scans carried out at positions along the fractional order rod measured while holding the electrode potential at -0.4 V, -0.34 V, -0.22 V and -0.1 V. The shape of the profile appears similar at potentials -0.4 V and -0.34 V, whereas the profile changes between -0.34 V and -0.22 V. This indicates a change in structure between -0.34 V and -0.22 V, which is in agreement with the changing intensity at $(0.5, 0.5, 0.6)$ observed in Figure 6.5. Another change in the intensity profile between potentials -0.22 V and -0.1 V is observed, indicating another structure change. This is consistent with the drop in intensity observed at $(0.5, 0.5, 0.6)$ over this potential range (specifically -1.8 V to -1.2 V) in the stationary rocking scans (Figure 6.5). The changes observed indicate that as the Pb UPD layer is lifted from the Cu(001) surface and as Cl is adsorbed, intermediate structures are formed, agreeing with previous studies on the alloying processes proposed at these potentials [170].

With the potential dependent rocking scan analysis carried out and presented in Figure 6.5 and 6.6, electrode potentials have been identified at which intermediate surface structures are formed on the Cu(001) surface during the dissolution of the Pb UPD layer. The aim is to obtain more detail on these structures via SXRD and compare the findings with previous STM [170, 168, 166] and LEED [164, 165, 167, 129] reports.

To further investigate the surface structure exhibited at different electrode potentials during dissolution of the Pb UPD layer on the Cu(001) surface, SXRD measurements were made along the $(1, 0, l)$, $(1, 1, l)$ CTRs and the $(0.5, 0.5, l)$ fractional order rod. The electrode potential was swept from -0.1 V to -0.5 V, to form the UPD layer, before holding the potential at -0.48 V to perform the first set of CTR scans. CTRs were measured by carrying out rocking scans at intervals along the l reciprocal lattice direction. The areas of the fitted

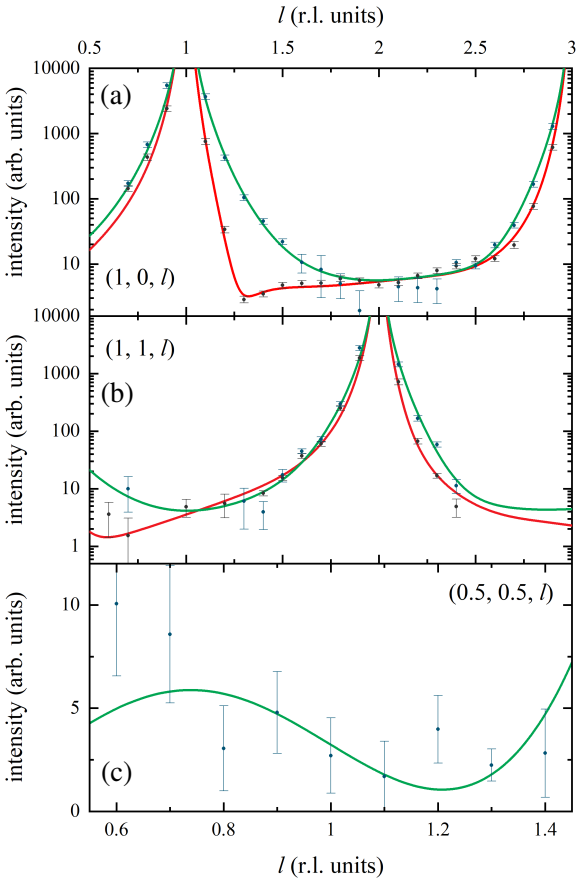

Fig. 6.7 Fitted CTR data of the Cu(001) surface during dissolution of the Pb UPD layer. Rocking scans along the (a) $(1,0,l)$, (b) $(1,1,l)$ CTRs and (c) $(0.5,0.5,l)$ fractional order rod were fitted, with both the data and the calculation shown for the data taken while holding the electrode potential at -0.48 V (black points, red curve) and -0.1 V (blue points, green curve)

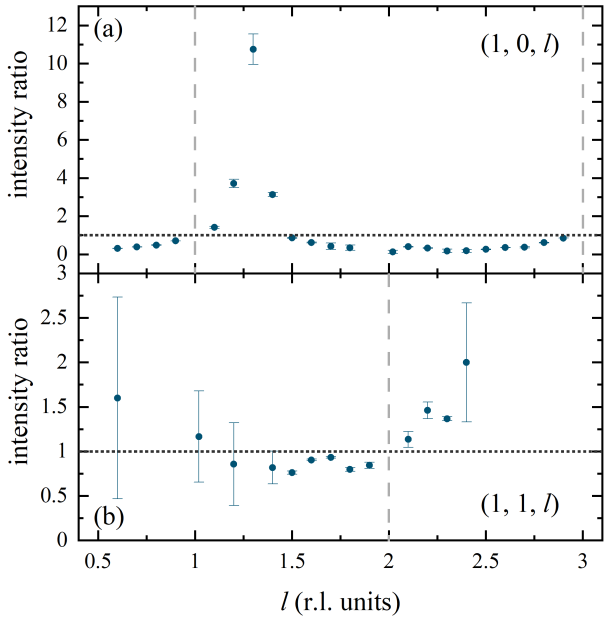

Fig. 6.8 Ratio of CTR intensity profiles measured at -0.4 V to those measured at -0.48 V for the Cu(001) surface during dissolution of the Pb UPD layer. Rocking scans along the (a) $(1,0,l)$ and (b) $(1,1,l)$ CTRs were fitted, with the ratio of the integrated intensities (blue points) plotted against l

rocking scans give the integrated x-ray intensities and are plotted against l in Figure 6.7 for electrode potentials of -0.48 V (black points) and -0.1 V (blue points). These CTR profiles are sensitive to the surface structure and therefore a comparison of the plots measured at different electrode potentials was investigated for insight into structural changes at the Cu(001) surface during the dissolution of the Pb UPD layer.

The CTR data at -0.48 V was fitted by modelling the surface with two Cu surface layers and a layer of Pb atoms sitting above the topmost Cu layer. The calculated intensity from this model is shown by the red curve in Figure 6.7 and the goodness of fit was represented by a reduced χ^2 of 3.257. Due to the larger atomic radius of Pb atoms (1.75 Å) in comparison with the Cu radius (1.28 Å), the maximum percentage of Cu(001) surface sites that may be occupied by UPD Pb is 60 %. Of those possible occupied sites, 81 ($\pm$ 7) % were occupied in the model, corresponding to a Pb coverage of $\theta = 0.43$ ($\pm$ 0.04).

The Pb UPD layer was modelled with a vertical separation from the topmost Cu layer of 2.12 ($\pm$ 0.02) Å, sitting in the four-fold hollow sites of the Cu(001) surface. Using this result, the bond length between Pb atoms of Cu atoms in the structural model is calculated to be 2.97 ($\pm$ 0.03) Å. This is consistent with the bond lengths reported in previous studies by Gauthier *et al.*: 2.9 Å[165].

The fit to the CTR data was achieved by including a β roughness factor of 0.79 ($\pm$ 0.05) and a rms displacement of 0.26($\pm$ 0.05) Å are applied to the UPD Pb layer in the model, indicating that the Pb atoms in the sample form an atomically rough surface structure. A rms displacement of 0.09($\pm$ 0.03) Å is also applied to the second Cu layer (sitting below the topmost layer of Cu) in order to obtain the best fit to the data. A systematic error of 10 % was also applied to all the least-squares fitting of CTR data, to account for the experimental error in the measurement.

Fitting the data at -0.1 V (green curve in Figure 6.7) was carried out by modelling the surface as the top Cu layers with a c (2×2) Cl adlayer sitting above. In the c (2×2) structure, 50 % of surface hollow sites are filled, and the results of fitting the data with this model found that the Cl coverage was θ =0.6 ($\pm$ 0.2), indicating that just over half of the c (2×2) sites are likely to be occupied by adsorbed chlorine. This corresponds to 28 ($\pm$ 0.11) % of the Cu(001) surface sites containing Cl ions.

The vertical separation between the Cl adlayer and the topmost Cu layer in the structural model was 1.56 ($\pm$ 0.05) Å, which corresponds to a bond length between Cu and Cl atoms in the structure of 2.60 ($\pm$ 0.08) Å. This result is greater than the Cu-Cl bond length reported for copper(I) chloride (2.051 Å) by around 27 %.

The Cu(001) surface experiences subsurface buckling of the second Cu layer, in which Cu atoms sit directly underneath Cl atoms in the adlayer, as has been previously reported for

halide adsorption on Cu(001) [127, 29, 161, 126]. The amount of buckling was determined by fitting the data, finding an inward relaxation of 0.14 ($\pm$ 0.02) Å for the atoms sitting directly underneath Cl atoms, and an outward expansion of +0.15 ($\pm$ 0.03) Å for the atoms sitting below unoccupied surface sites. A β roughness factor of 0.57 ($\pm$ 0.04) was applied to achieve the best fit to the data, giving a reduced χ^2 of 2.811.

It is clear that the green curve calculated from the model fits well for the $(1,0,l)$, $(1,1,l)$ CTRs (Figure 6.7a, b), passing through the errors bars of the data points, however for plot (c), the $(0.5,0.5,l)$ fractional order rod, it does not pass through all the error bars. This curve shape has been chosen as the best fit to the data when considering all three rods simultaneously, taking into account the size of the error bars and the data distribution in (c).

CTR analysis revealed that the structures formed at both -0.48 V and -0.1 V were significantly rough surfaces, meaning that determining any precise atomic structural ordering is difficult. Therefore, verifying the proposed structures formed by the UPD Pb and the intermediate structures that may be present during dissolution of the Pb adlayer proves to be challenging.

For a qualitative analysis of the intermediate structure changes that occur over the potential range from -0.48 V to -0.1 V, a comparison can be made between the CTR profiles by calculating the ratio of intensities measured at two electrode potentials. The ratio of the CTR intensity at -0.4 V to that at -0.48 V is plotted against l in Figure 6.8, indicating that a significant change in the $(1,0,l)$ CTR profile occurs between these electrode potentials at the l = 1.3 position. This is an indication of the structural rearrangement occurring as the electrode potential is stepped from -0.48 V to -0.4 V during the dissolution of the UPD Pb adlayer. The ratios between CTR profiles at -0.4 V, -0.34 V, -0.22 V and -0.1 V were also calculated, however there were no significant changes evident such as those observed between -0.48 V and -0.4 V. This does not mean that no structural rearrangement is occurring between these potentials, simply that any structural rearrangements that do occur are not as impactful on the overall CTR profile as that occurring between -0.48 V and -0.4 V. As Pb has a larger number of electrons than Cu, Pb atoms are stronger scatterers and therefore the UPD Pb monolayer in place at -0.48 V has a strong influence on the CTR shape. The CTR intensity ratios may suggest that the majority of Pb is removed from the surface at potentials negative of -0.4 V, and that there are lower coverages of Pb between -0.4 V and -0.1 V. The less Pb coverage there is at the surface, the less impact the structural rearrangement of that Pb will have on the scattering signal and hence the CTR intensity profiles.

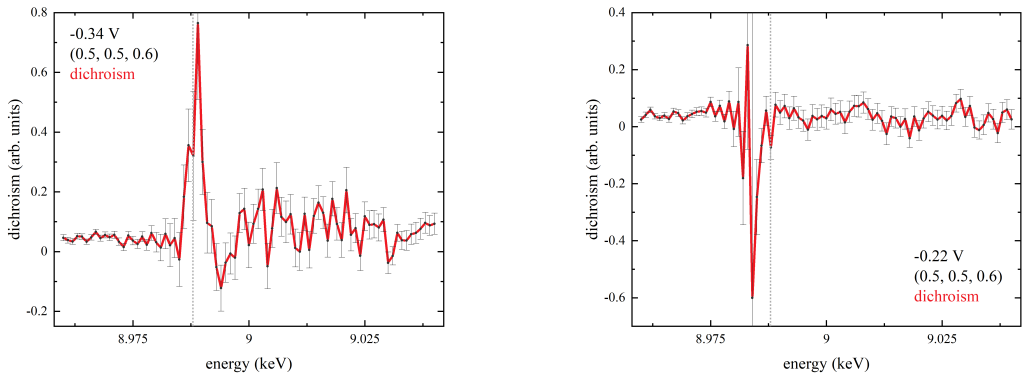

(a) (b)

Fig. 6.9 Resonant surface x-ray diffraction measurements of the Cu(001) surface as the Pb UPD layer is removed. Scans through the Cu K-edge are made at the $(0.5, 0.5, 0.6)$ superstructure position while potential is held at (a) -0.34 V and (b) -0.22 V. (a) and (b) show the dichroism signal calculated from the diffracted signals from the $(0.5, 0.5, 0.6)$ superstructure position as the energy is scanned through the Cu K-edge, measured with both σ- and π-polarised x-rays. The dotted grey vertical line indicates the position of the Cu K-edge energy at 8.9789 keV.

6.3.4 Resonant SXRD Study of Pb UPD on Cu(001)

The dissolution of the Pb UPD adlayer from the Cu(001) surface was also investigated by resonant surface x-ray diffraction, performing energy scans through the Cu K-edge energy (8.9789 keV) at surface-sensitive reciprocal space positions with both σ-polarised and π-polarised x-rays. Figure 6.9 shows the results of energy scans of diffraction intensity from the $(0.5, 0.5, 0.6)$ superstructure-sensitive position, measured while holding the potential at -0.34 V and -0.22 V as the potential was stepped positive from -0.48 V to remove the Pb UPD layer. The diffracted intensity from the $(0.5, 0.5, 0.6)$ position was monitored as the incident x-ray energy was scanned from 8.96 keV to 9.04 keV. The x-ray polarisation was flipped from σ to π polarisation and the measurement was repeated. The dichroism signal, calculated from the x-ray diffraction signals obtained with both σ- and π-polarised x-rays, is plotted in Figure 6.9a and 6.9b, where the red line is a smoothed curve passing through data points. The Cu K-edge is indicated in the plots by the dotted vertical line.

The dichroism quantifies the difference between the σ- and π-polarised RSXRD signals, and is given by

$$I_D = \frac{I_\sigma - I_\pi}{I_\sigma + I_\pi} \tag{6.1}$$

where I_σ is the σ-polarised x-ray signal and I_π is the π-polarised x-ray signal. It is clear from the dichroism signal at the two potentials that there is a change in the structure, as the peak in the data is inverted between the two plots. This indicates a modification in the charge distribution is occurring, driven by the change in electrode potential from -0.34 V to -0.22 V.

As mentioned in Section 6.3.2 for an equivalent fractional order rod position, at the $(0.5, 0.5, 0.6)$ reciprocal space position, only the superstructure contributes to the SXRD signal, with minimal contribution from the Cu(001) surface or bulk Cu at positions far from the Bragg peak. This means that the modification in charge distribution observed in the dichroism signal is occurring in the electron orbitals of Cu atoms that are forming the superstructure at -0.34 V and -0.22 V. For a full quantitative analysis of this data, first principles calculations are necessary, which may be possible in the future with the use of FDMNES, developed for the calculation of resonant x-ray diffraction data from surfaces [153–155].

6.4 Conclusions

Resonant surface x-ray diffraction measurements were made for both the iodine adlayer on the Cu(001) surface and surface structures formed during the dissolution of a UPD-Pb layer on Cu(001) in the presence of Cl ions. The investigation included structural characterisations of the electrode surfaces carried out by analysis of CTR data.

The iodine superstructure formed at negative electrode potentials on Cu(001) was found to be similar to adlayer superstructures formed by both Cl and Br on Cu(001), exhibiting a c(2×2) periodicity and subsurface buckling of the second layer of Cu atoms. The amplitude of the buckling was found to be comparable with similar buckling reported in previous studies of the phenomena for halide adsorbate structures on Cu(001).

Resonant SXRD studies of the Cu(001)-c(2×2) I electrode surface were undertaken by monitoring the surface diffraction signal while scanning the incident x-ray energy through the Cu-K edge energy, finding a modification of the charge distribution in the direction normal to the sample surface. This effect was detected in the p_z orbitals of the atoms in the buckled subsurface Cu layer.

Crystal truncation rod analysis of the Cu(001) surface was also carried out at electrode potentials during the dissolution of a UPD Pb layer. The results of fitting SXRD data

were not able to verify the surface structures that have been previously observed by STM [170, 168, 166] studies, however did determine the positions of atoms in the UPD Pb layer in the surface normal direction. The Pb atoms are found to sit as close to the topmost Cu layer as possible, in surface sites with minimal expansion. The structure formed by the UPD Pb layer was also found to have a coverage of θ = 0.43 ($\pm$ 0.04), which is 81 ($\pm$ 7) % of the maximum possible Pb coverage on Cu(001). At more positive potentials, where significant dissolution of the UPD Pb has occurred, the CTR analysis found evidence for a similar c(2×2) halide superstructure formed by the Cl ions, with subsurface buckling of the second Cu layer.

Energy scans were carried out to obtain RSXRD data at electrode potentials during the dissolution of the UPD Pb layer on Cu(001). Results indicated that a significant modification of the charge distribution occurred for Cu atoms in the superstructure contributing to diffraction from the $(0.5, 0.5, 0.6)$ reciprocal space position between potentials of -0.34 V and -0.22 V. Along with the investigation of the iodine superstructure on Cu(001), the RSXRD results, although qualitative, show that the technique is a powerful tool for *in situ* probing of the charge distribution of specific atoms at these solid liquid interfaces.

To quantify the changes in charge distribution that were revealed in these experiments, a comparison with first principles calculations of the RSXRD from these structures would be the next step. This may be achievable with the recently reported FDMNES program, which has been used for other electrochemical systems, including the Cu(001)-c(2×2) Br adlayer structure [153–155, 175].

Chapter 7

Conclusions and Future Work

The previous pages have detailed investigations of structure changes at model electrode surfaces during electrochemical reactions. These fundamental electrochemistry studies aim to develop our understanding of these systems and the underlying reasons behind certain electrochemical processes and phenomena. It is hoped that the knowledge gleaned from these experiments may offer insight into the influence that atomic structure at the electrochemical solid-liquid interface has on some key catalytic processes.

In Chapter 4, it was shown that the hexagonal reconstructions that occur on the Au(001) and Au(111) model electrode surfaces in alkaline electrolyte solution exhibit a potential dependent compressibility. The compressibility of the reconstructed surface structure is considered to be due to a build up of charge at the surface at negative electrode potentials. In electrolyte solution saturated with carbon monoxide (CO), the potential dependence of the compressibility is suppressed, with both the Au(001) and Au(111) surfaces being locked into highly compressed phases. This is concluded to be due to the CO molecules adsorbed at the surface acting to accommodate the excess surface charge induced by changing electrode potentials. This leads to enhanced catalytic activity for gold surfaces with adsorbed CO, with reconstructed surfaces exhibiting stability over a wider potential range. It was also found that, in the absence of CO, the number of H_2O molecules in the solvation shell of cations in the electrolyte solution has an influence on the degree of potential dependence that the Au(111) surface compressibility experienced. For cations with fewer H_2O molecules in their solvation shell, the compressibility of the reconstructed surface structure was more sensitive to changes in the applied electrode potential. Therefore, the changes in compression during the reconstruction process were observed over shorter potential ranges for cations such as Li^+, than for cations with more H_2O molecules in their solvation shell such as Cs^+. A natural continuation of this work would be to investigate whether a similar cation effect is observable for the Au(001) reconstruction as well.

Studies of phosphate species adsorption on the Cu(111) surface, presented in Chapter 5, found that the underlying mechanisms of phosphate adsorption were accompanied by a roughening of the copper surface. A mixed copper-oxygen layer forms at the surface, with oxygen from the phosphate species being incorporated into the Cu layer as part of the roughening. These experiments showed how important the preparation of copper electrode sample surfaces and the electrode history is for the surface stability and potential dependence of surface roughness. Preparation methods that resulted in the presence of Cu nano-islands at the surface lead to 3D nucleation and the growth of nano-crystals. This resulted in irreversible changes in the morphology of the Cu(001) surface. These findings have significant impact for the stability of catalysts under operational conditions for the carbon dioxide (CO_2) reduction reaction. The implications of these findings could be significant, as it could be that many researchers or engineers in industry are preparing Cu surfaces without full knowledge of the surface morphology present in their samples. Additionally, the observed incorporation of oxygen into the Cu surface is a process that is relevant to the study of oxo-anions, such as sulphate, and their role in the stability of electrocatalysts during oxidation processes. As a continuation of this work, further studies have begun into phosphate adsorption on the Cu(001) surface, and it is hoped that that surface structure formed can be compared with the results discussed in Chapter 5. It will be interesting to see whether the Cu(001) surface morphology exhibits a similar sensitivity to the method of sample preparation as the Cu(111) surface did.

It was shown, in Chapter 6, that iodine forms a similar adlayer superstructure on the Cu(001) surface to that formed by bromine and chlorine. This includes a subsurface buckling of Cu atoms in the second Cu layer. The subsurface buckled Cu atoms were found to exhibit a modification in the charge density of their p_z orbitals, in the direction normal to the sample surface. Halide ions are useful for stabilising underpotential deposited layers, and the UPD Pb layer on Cu(001) in the presence of chlorine was shown in this chapter to sit as close as possible to the topmost Cu layer with minimal expansion. Following dissolution of UPD Pb monolayer, Cl forms an adlayer superstructure similar to that previously reported on Cu(001) in the absence of Pb. During the dissolution of the Pb UPD layer, a significant change in the charge distribution was detected between -0.34 V and -0.22 V in Cu atoms at the surface. Results for I on Cu(001) and Pb UPD on Cu(001) in the presence of Cl both showed significant modification in charge distribution at the surface when probed by resonant surface x-ray diffraction (RSXRD) at the Cu-K edge energy. It is hoped that future work by comparing these results to first principles calculations using FDMNES can help to quantify these changes in charge distribution and uncover the nature of the bonding between different atoms in these electrochemical systems.

This work consists of surface x-ray diffraction investigations into a range of electrochemical systems with implications for catalysis and other areas of application. SXRD is a well-established and powerful tool, but is still developing, as evidenced by the surface diffraction coupled with spectroscopic measurements presented in Chapter 6. By reconciling RSXRD results with first principles calculations, researchers hope to uncover rich detail on the nature of charge distribution, which could change the way the solid-liquid interface and electrochemical double layer is modelled. Novel electrochemical cell designs under development may accommodate new sample environments and make measurements of more electrochemical systems with SXRD accessible for the first time. Other novel SXRD techniques such as high energy SXRD, where entire reciprocal space maps can be imaged using 2D detectors in minutes, show huge promise for the future of determining the atomic structure of material surfaces.

References

[1] I. K. Robinson and D. J. Tweet. Surface X-Ray Diffraction. *Reports on Progress in Physics*, 55(5):599–651, (1992).

[2] Y. Gründer and C. A. Lucas. Surface X-Ray Diffraction Studies of Single Crystal Electrocatalysts. *Nano Energy*, 29:378 – 393, (2016).

[3] P. Fenter and N. C. Sturchio. Mineral–Water Interfacial Structures Revealed by Synchrotron X-Ray Scattering. *Progress in Surface Science*, 77(5):171–258, (2004).

[4] M. Faraday. VI. Experimental Researches in Electricity.-Seventh Series. *Philosophical Transactions of the Royal Society of London*, 124:77–122, (1834).

[5] C. Kittel. *Introduction to Solid State Physics.* J. Wiley, Danvers, (2005).

[6] S. Trasatti. The Absolute Electrode Potential: An Explanatory Note (Recommendations 1986). *Pure and Applied Chemistry*, 58(7):955 – 966, (1986).

[7] H. Helmholtz. Ueber Einige Gesetze der Vertheilung Elektrischer Ströme in Körperlichen Leitern mit Anwendung auf die Thierisch-Elektrischen Versuche. *Annalen der Physik*, 165(6):211–233, (1853).

[8] H. Helmholtz. Studien über electrische Grenzschichten. *Annalen der Physik*, 243(7):337–382, (1879).

[9] D. C. Grahame and B. A. Soderberg. Technical Report No. 14 to the Office of Naval Research. *Amherst College, Amherst, Mass., Feb*, 21, (1954).

[10] M. Gouy. Sur la Constitution de la Charge Électrique à la Surface d'un Électrolyte. *Journal de Physique Théorique et Appliquée*, 9(1):457–468, (1910).

[11] D. L. Chapman. LI. A Contribution to the Theory of Electrocapillarity. *The London, Edinburgh, and Dublin Philosophical Magazine and Journal of Science*, 25(148):475–481, (1913).

[12] E. Gileadi. *Physical Electrochemistry: Fundamentals, Techniques and Applications.* Wiley-VCH, Weinheim, (2011).

[13] O. Stern. The Theory of the Electrolytic Double-Layer. *Z. Elektrochem*, 30(508):1014–1020, (1924).

[14] D. C. Grahame. The Electrical Double Layer and the Theory of Electrocapillarity. *Chemical Reviews*, 41(3):441–501, (1947).

[15] N. Elgrishi, K. J. Rountree, B. D. McCarthy, et al. A Practical Beginner's Guide to Cyclic Voltammetry. *Journal of Chemical Education*, 95(2):197–206, (2018).

[16] B.E. Warren. *X-Ray Diffraction*. Addison-Wesley series in metallurgy and materials engineering. Dover Publications, New York, (1990).

[17] J. D. Jackson. *Classical Electrodynamics*. John Wiley & sons, New York, (1975).

[18] W. H. Bragg and W. L. Bragg. The Reflection of X-Rays by Crystals. *Proceedings of the Royal Society of London. Series A, Containing Papers of a Mathematical and Physical Character*, 88(605):428–438, (1913).

[19] P. H. Fuoss and S. Brennan. Surface Sensitive X-Ray Scattering. *Annual Review of Materials Science; (United States)*, 20(1), (1990).

[20] R. Feidenhans'l. Surface Structure Determination by X-Ray Diffraction. *Surface Science Reports*, 10(3):105 – 188, (1989).

[21] B. E. Warren. *X-Ray Diffraction, Courier Corporation*. Addison-Wesley Publishing Company, Reading, (1969).

[22] B. W. Batterman and H. Cole. Dynamical Diffraction of X Rays by Perfect Crystals. *Rev. Mod. Phys.*, 36:681–717, Jul (1964).

[23] E. Price, editor. *International Tables for Crystallography Volume C: Mathematical, Physical and Chemical Tables*, volume C, chapter 6.1, pages 554–596. Kluwer, Dordrecht, third edition, (2004).

[24] K. Krug, J. Stettner, and O. M. Magnussen. In Situ Surface X-Ray Diffraction Studies of Homoepitaxial Electrochemical Growth on Au(100). *Phys. Rev. Lett.*, 96:246101, (2006).

[25] F. Golks, Y. Gründer, A. Drünkler, et al. In Situ Surface X-Ray Diffraction Studies of the Influence of the PEG-Cl-Complex on Homoepitaxial Electrodeposition on Cu(001). *Journal of The Electrochemical Society*, 160(12):D3165–D3170, (2013).

[26] F. Golks, Y. Gründer, J. Stettner, et al. In Situ Surface X-Ray Diffraction Studies of Homoepitaxial Growth on Cu(001) from Aqueous Acidic Electrolyte. *Surface Science*, 631:112–122, (2015).

[27] F. Golks, J. Stettner, Y. Gründer, et al. Anomalous Potential Dependence in Homoepitaxial Cu(001) Electrodeposition: An In Situ Surface X-Ray Diffraction Study. *Phys. Rev. Lett.*, 108:256101, (2012).

[28] J. M. Hermann, Y. Mattausch, A. Weiß, et al. Enhanced Electrocatalytic Oxidation of Formic Acid on Au(111) in the Presence of Pyridine. *Journal of The Electrochemical Society*, 165(15):J3192–J3198, (2018).

[29] Y. Gründer, P. Thompson, A. Brownrigg, et al. Probing the Halide–Metal Interaction by Monolayer Metal Deposition at the Electrochemical Interface. *The Journal of Physical Chemistry C*, 116(10):6283–6288, (2012).

[30] C. A. Lucas and N. M. Marković. *Structure Relationships in Electrochemical Reactions*, pages 295–360. John Wiley & Sons, Ltd, (2007).

[31] E. A. Wood. Vocabulary of Surface Crystallography. *Journal of Applied Physics*, 35(4):1306–1312, (1964).

[32] U. Landman, R. N. Hill, and M. Mostoller. Lattice Relaxation at Metal Surfaces: An Electrostatic Model. *Phys. Rev. B*, 21:448–457, (1980).

[33] K. Kádas, Z. Nabi, S.K. Kwon, et al. Surface Relaxation and Surface Stress of 4d Transition Metals. *Surface Science*, 600(2):395–402, (2006).

[34] R. Behrisch and K. Wittmaack. *Sputtering by Particle Bombardment*, volume 1. Springer-Verlag New York, (1981).

[35] A. Hickling. Studies in Electrode Polarisation. Part IV.—The Automatic Control of the Potential of a Working Electrode. *Trans. Faraday Soc.*, 38:27–33, (1942).

[36] F. R. Elder, A. M. Gurewitsch, R. V. Langmuir, and H. C. Pollock. Radiation from Electrons in a Synchrotron. *Phys. Rev.*, 71:829–830, (1947).

[37] H. C. Pollock. The Discovery of Synchrotron Radiation. *American Journal of Physics*, 51(3):278–280, (1983).

[38] C. Nicklin, T. Arnold, J. Rawle, and A. Warne. Diamond Beamline I07: A Beamline for Surface and Interface Diffraction. *Journal of Synchrotron Radiation*, 23(5):1245–1253, (2016).

[39] Ch. Brönnimann, S. Florin, M. Lindner, et al. Synchrotron Beam Test with a Photon-Counting Pixel Detector. *Journal of Synchrotron Radiation*, 7(5):301–306, (2000).

[40] E. Vlieg. A (2+3)-Type Surface Diffractometer: Mergence of the z-Axis and (2+2)-Type Geometries. *Journal of Applied Crystallography*, 31(2):198–203, (1998).

[41] S. P. Collins, A. Bombardi, A. R. Marshall, et al. Diamond Beamline I16 (Materials & Magnetism). In *AIP Conference Proceedings*, volume 1234, pages 303–306, (2010).

[42] C. Giles, C. Malgrange, J. Goulon, et al. Energy-Dispersive Phase Plate for Magnetic Circular Dichroism Experiments in the X-Ray Range. *Journal of Applied Crystallography*, 27(3):232–240, (1994).

[43] S. D. Brown, L. Bouchenoire, D. Bowyer, et al. The XMaS Beamline at ESRF: Instrumental Developments and High-Resolution Diffraction Studies. *Journal of Synchrotron Radiation*, 8(6):1172–1181, (2001).

[44] W. R. Busing and H. A. Levy. Angle Calculations for 3- and 4-Circle X-Ray and Neutron Diffractometers. *Acta Crystallographica*, 22(4):457–464, Apr (1967).

[45] MATLAB. version 9.10.0 (R2021a), (2021).

[46] C. M. Schlepütz, R. Herger, P. R. Willmott, et al. Improved Data Acquisition in Grazing-Incidence X-Ray Scattering Experiments using a Pixel Detector. *Acta Crystallographica Section A*, 61(4):418–425, (2005).

[47] C. M. Schlepütz, S. O. Mariager, S. A. Pauli, et al. Angle Calculations for a (2+3)-Type Diffractometer: Focus on Area Detectors. *Journal of Applied Crystallography*, 44(1):73–83, (2011).

[48] C. A. Lucas and N. M. Marković. *In-Situ X-Ray Diffraction Studies of the Electrode/Solution Interface*, chapter 1, pages 1–45. John Wiley & Sons, Ltd, (2006).

[49] C. A. Lucas, P. Thompson, M. Cormack, et al. Temperature-Induced Ordering of Metal/Adsorbate Structures at Electrochemical Interfaces. *Journal of the American Chemical Society*, 131(22):7654–7661, (2009).

[50] E. Vlieg. Integrated Intensities Using a Six-Circle Surface X-ray Diffractometer. *Journal of Applied Crystallography*, 30(5 Part 1):532–543, (1997).

[51] MATLAB. version 9.7.5.184 (2020b), (2020).

[52] A. Beniya and S. Higashi. Towards Dense Single-Atom Catalysts for Future Automotive Applications. *Nature Catalysis*, 2(7):590–602, (2019).

[53] M. Haruta. Gold Rush. *Nature*, 437(7062):1098–1099, (2005).

[54] M. Haruta, T. Kobayashi, H. Sano, and N. Yamada. Novel Gold Catalysts for the Oxidation of Carbon Monoxide at a Temperature far Below 0 °C. *Chemistry Letters*, 16(2):405–408, (1987).

[55] W. C. Ketchie, Y.-L. Fang, M. S. Wong, et al. Influence of Gold Particle Size on the Aqueous-Phase Oxidation of Carbon Monoxide and Glycerol. *Journal of Catalysis*, 250(1):94 – 101, (2007).

[56] J. L. Roberts and . T. Sawyer. Voltammetric Determination of Carbon Monoxide at Gold Electrodes. *Journal of Electroanalytical Chemistry (1959)*, 7(4):315 – 319, (1964).

[57] J. L. Roberts and D. T. Sawyer. Electrochemical Oxidation of Carbon Monoxide at Gold Electrodes. *Electrochimica Acta*, 10(10):989 – 1000, (1965).

[58] H. Kita, H. Nakajima, and K. Hayashi. Electrochemical Oxidation of CO on Au in Alkaline Solution. *Journal of Electroanalytical Chemistry and Interfacial Electrochemistry*, 190(1):141 – 156, (1985).

[59] H. Nakajima, H. Kita, K. Kunimatsu, and A. Aramata. Infrared Spectra of Carbon Monoxide Adsorbed on a Smooth Gold Electrode Part I. EMIRS Spectra in Acid and Alkaline Solutions. *Journal of Electroanalytical Chemistry and Interfacial Electrochemistry*, 201(1):175 – 186, (1986).

[60] K. Kunimatsu, A. Aramata, N. Nakajima, and H. Kita. Infrared Spectra of Carbon Monoxide Adsorbed on a Smooth Gold Electrode: Part II. Emirs and Polarization-Modulated Irras Study of the Adsorbed CO layer in Acidic and Alkaline Solutions. *Journal of Electroanalytical Chemistry and Interfacial Electrochemistry*, 207(1):293 – 307, (1986).

[61] P. Rodriguez, J. M. Feliu, and M. T. M. Koper. Unusual Adsorption State of Carbon Monoxide on Single-Crystalline Gold Electrodes in Alkaline Media. *Electrochemistry Communications*, 11(6):1105 – 1108, (2009).

[62] P. Rodriguez, Y. Kwon, and M. T. M. Koper. The Promoting Effect of Adsorbed Carbon Monoxide on the Oxidation of Alcohols on a Gold Catalyst. *Nature chemistry*, 4(3):177–182, (2012).

[63] P. Rodriguez, N. Garcia-Araez, and M. T. M. Koper. Self-Promotion Mechanism for CO Electrooxidation on Gold. *Phys. Chem. Chem. Phys.*, 12:9373–9380, (2010).

[64] P. Rodriguez, N. Garcia-Araez, A. Koverga, et al. CO Electroxidation on Gold in Alkaline Media: A Combined Electrochemical, Spectroscopic, and DFT Study. *Langmuir*, 26(14):12425–12432, (2010).

[65] P. Rodríguez, A. A. Koverga, and M. T. M. Koper. Carbon Monoxide as a Promoter for its own Oxidation on a Gold Electrode. *Angewandte Chemie International Edition*, 49(7):1241–1243, (2010).

[66] M. A. Van Hove, R. J. Koestner, P. C. Stair, et al. The Surface Reconstructions of the (100) Crystal Faces of Iridium, Platinum and Gold: I. Experimental Observations and Possible Structural Models. *Surface Science*, 103(1):189 – 217, (1981).

[67] I. M. Tidswell, N. M. Marković, and P. N. Ross. Potential Dependent Structure of Single Crystal Gold Interfaces in Alkaline Electrolyte: An In-Situ X-Ray Scattering Study. *Surface Science*, 317(1):241 – 252, (1994).

[68] B. M. Ocko, G. Helgesen, B. Schardt, et al. Charge Induced (1×3) Reconstruction of the Au(110) Surface: An X-Ray Scattering Study. *Phys. Rev. Lett.*, 69:3350–3353, (1992).

[69] J. Wang, A. J. Davenport, H. S. Isaacs, and B. M. Ocko. Surface Charge-Induced Ordering of the Au(111) Surface. *Science*, 255(5050):1416–1418, (1992).

[70] I. M. Tidswell, N. M. Marković, C. A. Lucas, and P. N. Ross. In Situ X-Ray-Scattering Study of the Au(001) Reconstruction in Alkaline and Acidic Electrolytes. *Phys. Rev. B*, 47:16542–16553, (1993).

[71] B. M. Ocko, J. Wang, A. Davenport, and H. Isaacs. In Situ X-Ray Reflectivity and Diffraction Studies of the Au(001) Reconstruction in an Electrochemical Cell. *Phys. Rev. Lett.*, 65:1466–1469, (1990).

[72] P. A. Thiel and P. J. Estrup. *The Handbook of Surface Imaging and Visualization*, pages 407–420. CRC Press, Boca Raton, FL, (1995).

[73] F. Hanke and J. Björk. Structure and Local Reactivity of the Au(111) Surface Reconstruction. *Phys. Rev. B*, 87:235422, (2013).

[74] A. P. Seitsonen. Electronic Structure of Reconstructed Au(111) Studied with Density Functional Theory. *Surface Science*, 643:150 – 155, (2016).

[75] J. V. Barth, H. Brune, G. Ertl, and R. J. Behm. Scanning Tunneling Microscopy Observations on the Reconstructed Au(111) Surface: Atomic Structure, Long-Range Superstructure, Rotational Domains, and Surface Defects. *Phys. Rev. B*, 42:9307–9318, (1990).

[76] J. Wang, B. M. Ocko, A. J. Davenport, and H. S. Isaacs. In Situ X-Ray Diffraction and Reflectivity Studies of the Au(111)/Electrolyte Interface: Reconstruction and Anion Adsorption. *Phys. Rev. B*, 46:10321–10338, (1992).

[77] A. R. Sandy, S. G. J. Mochrie, D. M. Zehner, et al. Structure and Phases of the Au(111) Surface: X-Ray Scattering Measurements. *Phys. Rev. B*, 43:4667–4687, (1991).

[78] D. L. Abernathy, D. Gibbs, G. Grübel, et al. Reconstruction of the (111) and (001) Surfaces of Au and Pt: Thermal Behavior. *Surface Science*, 283(1):260–276, (1993).

[79] D. Gibbs, B. M. Ocko, D. M. Zehner, and S. G. J. Mochrie. Structure and Phases of the Au(001) Surface: In-Plane Structure. *Phys. Rev. B*, 42:7330–7344, (1990).

[80] B. B. Blizanac, C. A Lucas, M. E. Gallagher, et al. Anion Adsorption, CO Oxidation, and Oxygen Reduction Reaction on a Au(100) Surface: The pH Effect. *The Journal of Physical Chemistry B*, 108(2):625–634, (2004).

[81] B. B. Blizanac, C. A. Lucas, M. E. Gallagher, et al. Surface Structures and Phase Transitions at the Au(100)-Br Interface: pH and CO Effects. *The Journal of Physical Chemistry B*, 108(17):5304–5313, (2004).

[82] M. E. Gallagher, B. B. Blizanac, C. A. Lucas, et al. Structure Sensitivity of CO Oxidation on Gold Single Crystal Surfaces in Alkaline Solution: Surface X-Ray Scattering and Rotating Disk Measurements. *Surface Science*, 582(1):215–226, (2005).

[83] D. Strmcnik, K. Kodama, D. van der Vliet, et al. The Role of Non-Covalent Interactions in Electrocatalytic Fuel-Cell Reactions on Platinum. *Nature chemistry*, 1(6):466–472, (2009).

[84] D. Strmcnik, M. Escudero-Escribano, K. Kodama, et al. Enhanced Electrocatalysis of the Oxygen Reduction Reaction based on Patterning of Platinum Surfaces with Cyanide. *Nature Chemistry*, 2(10):880–885, (2010).

[85] M. Wojdyr. Fityk: a General-Purpose Peak Fitting Program. *Journal of Applied Crystallography*, 43(5-1):1126–1128, (2010).

[86] A. Chen and J. Lipkowski. Electrochemical and Spectroscopic Studies of Hydroxide Adsorption at the Au(111) Electrode. *Journal of Physical Chemistry B*, 103(4):682–691, (1999).

[87] S. B. Aoun, Z. Dursun, T. Koga, et al. Effect of Metal Ad-Layers on Au(111) Electrodes on Electrocatalytic Oxidation of Glucose in an Alkaline Solution. *Journal of Electroanalytical Chemistry*, 567(2):175–183, (2004).

[88] J. G. Dash. 7 - Solid Phases and Melting Phenomena. In J. G. Dash, editor, *Films on Solid Surfaces*, pages 145–186. Academic Press, (1975).

[89] N. W. Ashcroft, N. D. Mermin, et al. *Solid State Physics*, volume 2005. Holt, Rinehart and Winston, New York London, (1976).

[90] O. R. Melroy, M. F. Toney, G. L. Borges, et al. An In-Situ Grazing Incidence X-Ray Scattering Study of the Initial Stages of Electrochemical Growth of Lead on Silver (111). *Journal of Electroanalytical Chemistry and Interfacial Electrochemistry*, 258(2):403–414, (1989).

[91] M. F. Toney, J. G. Gordon, M. G. Samant, et al. Underpotentially Deposited Thallium on Silver (111) by In Situ Surface X-Ray Scattering. *Phys. Rev. B*, 45:9362–9374, (1992).

[92] O. R. Melroy, M. F. Toney, G. L. Borges, et al. Two-Dimensional Compressibility of Electrochemically Adsorbed Lead on Silver (111). *Phys. Rev. B*, 38:10962–10965, (1988).

[93] C. Vaz-Domínguez, A. Aranzábal, and A. Cuesta. In Situ STM Observation of Stable Dislocation Networks during the Initial Stages of the Lifting of the Reconstruction on Au(111) Electrodes. *The Journal of Physical Chemistry Letters*, 1(14):2059–2062, (2010).

[94] Y. Marcus. Thermodynamics of Solvation of Ions. Part 5.—Gibbs Free Energy of Hydration at 298.15 K. *J. Chem. Soc., Faraday Trans.*, 87:2995–2999, (1991).

[95] S. S. Lee, P. Fenter, K. L. Nagy, and N. C. Sturchio. Real-Time Observation of Cation Exchange Kinetics and Dynamics at the Muscovite-Water Interface. *Nature communications*, 8(1):15826–15834, (2017).

[96] Y. Hori, I. Takahashi, O. Koga, and N. Hoshi. Selective Formation of C2 Compounds from Electrochemical Reduction of CO2 at a Series of Copper Single Crystal Electrodes. *The Journal of Physical Chemistry B*, 106(1):15–17, (2002).

[97] J. H. Montoya, A. A. Peterson, and J. K. Nørskov. Insights into C-C Coupling in CO2 Electroreduction on Copper Electrodes. *ChemCatChem*, 5(3):737–742, (2013).

[98] R. Kas, R. Kortlever, A. Milbrat, et al. Electrochemical CO2 Reduction on Cu2O-Derived Copper Nanoparticles: Controlling the Catalytic Selectivity of Hydrocarbons. *Phys. Chem. Chem. Phys.*, 16:12194–12201, (2014).

[99] G. O. Larrazábal, A. J. Martín, and J. Pérez-Ramírez. Building Blocks for High Performance in Electrocatalytic CO2 Reduction: Materials, Optimization Strategies, and Device Engineering. *The Journal of Physical Chemistry Letters*, 8(16):3933–3944, (2017).

[100] R. M. Arán-Ais, D. Gao, and B. Roldan Cuenya. Structure- and Electrolyte-Sensitivity in CO2 Electroreduction. *Accounts of Chemical Research*, 51(11):2906–2917, (2018).

[101] A. K. Engstfeld, T. Maagaard, S. Horch, et al. Polycrystalline and Single-Crystal Cu Electrodes: Influence of Experimental Conditions on the Electrochemical Properties in Alkaline Media. *Chemistry – A European Journal*, 24(67):17743–17755, (2018).

[102] P. Grosse, D. Gao, F. Scholten, et al. Dynamic Changes in the Structure, Chemical State and Catalytic Selectivity of Cu Nanocubes during CO2 Electroreduction: Size and Support Effects. *Angewandte Chemie International Edition*, 57(21):6192–6197, (2018).

[103] H. Mistry, A. S. Varela, C. S Bonifacio, et al. Highly Selective Plasma-Activated Copper Catalysts for Carbon Dioxide Reduction to Ethylene. *Nature communications*, 7(1):1–9, (2016).

[104] J. Resasco, L. D. Chen, E. Clark, et al. Promoter Effects of Alkali Metal Cations on the Electrochemical Reduction of Carbon Dioxide. *Journal of the American Chemical Society*, 139(32):11277–11287, (2017).

[105] C. S. Le Duff, M. J. Lawrence, and P. Rodriguez. Role of the Adsorbed Oxygen Species in the Selective Electrochemical Reduction of CO2 to Alcohols and Carbonyls on Copper Electrodes. *Angewandte Chemie International Edition*, 56(42):12919–12924, (2017).

[106] L. Mandal, K. R. Yang, M. R. Motapothula, et al. Investigating the Role of Copper Oxide in Electrochemical CO2 Reduction in Real Time. *ACS Applied Materials & Interfaces*, 10(10):8574–8584, (2018).

[107] A. Verdaguer-Casadevall, C. W. Li, T. P. Johansson, et al. Probing the Active Surface Sites for CO Reduction on Oxide-Derived Copper Electrocatalysts. *Journal of the American Chemical Society*, 137(31):9808–9811, (2015).

[108] S. Lee, D. Kim, and J. Lee. Electrocatalytic Production of C3-C4 Compounds by Conversion of CO2 on a Chloride-Induced Bi-Phasic Cu2O-Cu Catalyst. *Angewandte Chemie International Edition*, 54(49):14701–14705, (2015).

[109] A. Eilert, F. Cavalca, F. S. Roberts, et al. Subsurface Oxygen in Oxide-Derived Copper Electrocatalysts for Carbon Dioxide Reduction. *The Journal of Physical Chemistry Letters*, 8(1):285–290, (2017).

[110] D. Friebel, P. Broekmann, and K. Wandelt. Electrochemical In Situ STM Study of a Cu(111) Electrode in Neutral Sulfate Containing Electrolyte. *physica status solidi (a)*, 201(5):861–869, (2004).

[111] I. K. Robinson. Crystal Truncation Rods and Surface Roughness. *Phys. Rev. B*, 33:3830–3836, (1986).

[112] I. Platzman, R. Brener, H. Haick, and R. Tannenbaum. Oxidation of Polycrystalline Copper Thin Films at Ambient Conditions. *The Journal of Physical Chemistry C*, 112(4):1101–1108, (2008).

[113] C. Pérez León, C. Sürgers, and H. v. Löhneysen. Formation of Copper Oxide Surface Structures via Pulse Injection of Air onto Cu(111) Surfaces. *Phys. Rev. B*, 85:035434, (2012).

[114] T. Matsumoto, R.A. Bennett, P. Stone, et al. Scanning Tunneling Microscopy Studies of Oxygen Adsorption on Cu(111). *Surface Science*, 471(1):225–245, (2001).

[115] B. Gamoke, D. Neff, and J. Simons. Nature of PO Bonds in Phosphates. *The Journal of Physical Chemistry A*, 113(19):5677–5684, (2009).

[116] C. C. Pye and W. W. Rudolph. An ab Initio, Infrared, and Raman Investigation of Phosphate Ion Hydration. *The Journal of Physical Chemistry A*, 107(41):8746–8755, (2003).

[117] J. Rose, A.-M. Flank, A. Masion, et al. Nucleation and Growth Mechanisms of Fe Oxyhydroxide in the Presence of PO4 Ions. 2. P K-Edge EXAFS Study. *Langmuir*, 13(6):1827–1834, (1997).

[118] V. Maurice, H.-H. Strehblow, and P. Marcus. In Situ STM Study of the Initial Stages of Oxidation of Cu(111) in Aqueous Solution. *Surface Science*, 458(1):185–194, (2000).

[119] J. Kunze, V. Maurice, L. H. Klein, et al. In Situ Scanning Tunneling Microscopy Study of the Anodic Oxidation of Cu(111) in 0.1 M NaOH. *The Journal of Physical Chemistry B*, 105(19):4263–4269, (2001).

[120] J. Kunze, V. Maurice, L. H. Klein, et al. In Situ STM Study of the Anodic Oxidation of Cu(001) in 0.1 M NaOH. *Journal of Electroanalytical Chemistry*, 554-555:113–125, (2003).

[121] M. Yaguchi, T. Uchida, K. Motobayashi, and M. Osawa. Speciation of Adsorbed Phosphate at Gold Electrodes: A Combined Surface-Enhanced Infrared Absorption Spectroscopy and DFT Study. *The Journal of Physical Chemistry Letters*, 7(16):3097–3102, (2016).

[122] R. Gisbert, G. García, and M. T. M. Koper. Adsorption of Phosphate Species on Poly-Oriented Pt and Pt(111) Electrodes over a Wide Range of pH. *Electrochimica Acta*, 55(27):7961–7968, (2010).

[123] G. Niaura, A. K. Gaigalas, and V. L. Vilker. Surface-Enhanced Raman Spectroscopy of Phosphate Anions: Adsorption on Silver, Gold, and Copper Electrodes. *The Journal of Physical Chemistry B*, 101(45):9250–9262, (1997).

[124] F. Jensen, F. Besenbacher, E. Lægsgaard, and I. Stensgaard. Oxidation of Cu(111): Two New Oxygen Induced Reconstructions. *Surface Science*, 259(3):L774–L780, (1991).

[125] M. Saracino, P. Broekmann, K. Gentz, et al. Surface Relaxation Phenomena at Electrified Interfaces: Revealing Adsorbate, Potential, and Solvent Effects by Combined X-Ray Diffraction, STM and DFT Studies. *Phys. Rev. B*, 79:115448, (2009).

[126] Y. Gründer, D. Kaminski, F. Golks, et al. Reversal of Chloride-Induced Cu(001) Subsurface Buckling in the Electrochemical Environment: An In Situ Surface X-Ray Diffraction and Density Functional Theory Study. *Phys. Rev. B*, 81:174114, (2010).

[127] Y. Gründer and C. A. Lucas. Probing the Charge Distribution at the Electrochemical Interface. *Phys. Chem. Chem. Phys.*, 19:8416–8422, (2017).

[128] C. Kim, T. Möller, J. Schmidt, et al. Suppression of Competing Reaction Channels by Pb Adatom Decoration of Catalytically Active Cu Surfaces During CO2 Electroreduction. *ACS Catalysis*, 9(2):1482–1488, (2019).

[129] G. M. Brisard, E. Zenati, H. A. Gasteiger, et al. Underpotential Deposition of Lead on Cu(100) in the Presence of Chloride: Ex-Situ Low-Energy Electron Diffraction, Auger Electron Spectroscopy, and Electrochemical Studies. *Langmuir*, 13(8):2390–2397, (1997).

[130] V. Briega-Martos, E. Herrero, and J. M. Feliu. Pt(hkl) Surface Charge and Reactivity. *Current Opinion in Electrochemistry*, 17:97–105, (2019).

[131] J. W. Schultze and F. D. Koppitz. Bond Formation in Electrosorbates—I Correlation Between the Electrosorption Valency and Pauling's Electronegativity for Aqueous Solutions. *Electrochimica Acta*, 21(5):327–336, (1976).

[132] J. O'M. Bockris, B. E. Conway, E. Yeager, and R. E. White. *Comprehensive Treatise of Electrochemistry*, volume 1. Springer, (1980).

[133] W. Schmickler and R. Guidelli. The Partial Charge Transfer. *Electrochimica Acta*, 127:489–505, (2014).

[134] J. W. Schultze and D. Rolle. The Partial Discharge of Electrosorbates and its Influence in Electrocatalysis. *Canadian Journal of Chemistry*, 75(11):1750–1758, (1997).

[135] C. Stoffelsma, P. Rodriguez, G. Garcia, et al. Promotion of the Oxidation of Carbon Monoxide at Stepped Platinum Single-Crystal Electrodes in Alkaline Media by Lithium and Beryllium Cations. *Journal of the American Chemical Society*, 132(45):16127–16133, (2010).

[136] V. Colic, M. D. Pohl, D. Scieszka, and A. S. Bandarenka. Influence of the Electrolyte Composition on the Activity and Selectivity of Electrocatalytic Centers. *Catalysis Today*, 262:24–35, (2016).

[137] A. N. Frumkin. Influence of Cation Adsorption on the Kinetics of Electrode Processes. *Trans. Faraday Soc.*, 55:156–167, (1959).

[138] A. Frumkin. Wasserstoffüberspannung und Struktur der Doppelschicht. *Zeitschrift für Physikalische Chemie*, 164A(1):121–133, (1933).

[139] M. M. Waegele, C. M. Gunathunge, J. Li, and X. Li. How Cations Affect the Electric Double Layer and the Rates and Selectivity of Electrocatalytic Processes. *The Journal of Chemical Physics*, 151(16):160902, (2019).

[140] Y.-C. Lu, E. J. Crumlin, G. M. Veith, et al. In Situ Ambient Pressure X-Ray Photoelectron Spectroscopy Studies of Lithium-Oxygen Redox Reactions. *Scientific reports*, 2(1):1–6, (2012).

[141] S. Axnanda, E. J. Crumlin, B. Mao, et al. Using "Tender" X-Ray Ambient Pressure X-Ray Photoelectron Spectroscopy as a Direct Probe of Solid-Liquid Interface. *Scientific reports*, 5(1):1–12, (2015).

[142] V. A. Saveleva and E. R. Savinova. Insights into Electrocatalysis from Ambient Pressure Photoelectron Spectroscopy. *Current Opinion in Electrochemistry*, 17:79–89, (2019).

[143] C. A. Lucas, P. Thompson, Y. Gründer, and N. M. Marković. The Structure of the Electrochemical Double Layer: Ag(111) in Alkaline Electrolyte. *Electrochemistry Communications*, 13(11):1205–1208, (2011).

[144] I. C. Bourg, S. S. Lee, P. Fenter, and C. Tournassat. Stern Layer Structure and Energetics at Mica–Water Interfaces. *The Journal of Physical Chemistry C*, 121(17):9402–9412, (2017).

[145] E. Herrero, L. J. Buller, and H. D. Abruña. Underpotential Deposition at Single Crystal Surfaces of Au, Pt, Ag and Other Materials. *Chemical Reviews*, 101(7):1897–1930, (2001).

[146] A. E. Russell and A. Rose. X-ray Absorption Spectroscopy of Low Temperature Fuel Cell Catalysts. *Chemical Reviews*, 104(10):4613–4636, (2004).

[147] O. Endo, H. Kondoh, Y. Yonamoto, et al. The Effect of a Water Overlayer on the Chlorine-Chemisorbed Ag(100) Surface Studied by Cl K-Edge X-Ray Absorption Fine Structure. *Surface Science*, 463(2):135–144, (2000).

[148] O. Endo, D. Matsumura, K. Kohdate, et al. In-Situ XAFS Studies of Br Adsorption on the Silver(111) Electrode. *Journal of Electroanalytical Chemistry*, 494(2):121–126, (2000).

[149] Y. S. Chu, H. You, J. A. Tanzer, et al. Surface Resonance X-Ray Scattering Observation of Core-Electron Binding-Energy Shifts of Pt(111)-Surface Atoms during Electrochemical Oxidation. *Phys. Rev. Lett.*, 83:552–555, (1999).

[150] A. Menzel, K.-C. Chang, V. Komanicky, et al. Resonance Anomalous Surface X-Ray Scattering. In *Proceedings of the 20th International Conference on X-ray and Inner-Shell Processes*, volume 75, pages 1651–1660, (2006).

[151] A. Menzel, Y. V. Tolmachev, K.-C. Chang, et al. Polarization-Dependent Resonant Anomalous Surface X-Ray Scattering of CO/Pt(111). *Europhysics Letters (EPL)*, 74(6):1032–1038, (2006).

[152] T. Kondo, M. Shibata, N. Hayashi, et al. Resonance Surface X-Ray Scattering Technique to Determine the Structure of Electrodeposited Pt Ultrathin Layers on Au(111) Surface. *Electrochimica Acta*, 55(27):8302–8306, (2010).

[153] J. D. Bourke, C. T. Chantler, and Y. Joly. *FDMX*: Extended X-Ray Absorption Fine Structure Calculations using the Finite Difference Method. *Journal of Synchrotron Radiation*, 23(2):551–559, (2016).

[154] O. Bunău and Y. Joly. Self-Consistent Aspects of X-Ray Absorption Calculations. *Journal of Physics: Condensed Matter*, 21(34):345501, (2009).

[155] Y. Joly, A. Abisset, A. Bailly, et al. Simulation of Surface Resonant X-ray Diffraction. *Journal of Chemical Theory and Computation*, 14(2):973–980, (2018).

[156] Y. Joly, S. D. Matteo, and O. Bunău. Resonant X-Ray Diffraction: Basic Theoretical Principles. *The European Physical Journal Special Topics*, 208:21–38, (2012).

[157] C. G. Sanchez, E. P. M. Leiva, and J. Kohanoff. Relevance of Heterometallic Binding Energy for Metal Underpotential Deposition. *Langmuir*, 17(7):2219–2227, (2001).

[158] C. Sánchez and E. P. M. Leiva. Cu Underpotential Deposition on Au(111) and Au(100). Can this be Explained in Terms of the Energetics of the Cu/Au System? *Electrochimica Acta*, 45(4):691–697, (1999).

[159] M. C. Giménez, A. J. Ramirez-Pastor, and E. P. M. Leiva. A Model for Underpotential Deposition in the Presence of Anions. *The Journal of Chemical Physics*, 132(18):184703, (2010).

[160] V. A. Marichev. Partial Charge Transfer During Anion Adsorption: Methodological Aspects. *Surface Science Reports*, 56(8):277–324, (2005).

[161] H. C. N. Tolentino, M. De Santis, Y. Gauthier, and V. Langlais. Chlorine Chemisorption on Cu(001) by Surface X-Ray Diffraction: Geometry and Substrate Relaxation. *Surface Science*, 601(14):2962–2966, (2007).

[162] P. Sabatier. *La Catalyse en Chimie Organique, Encyclopédie de Science Chimique Appliquée.* Ch. Béranger, Paris, (1913).

[163] H. Xin, A. Vojvodic, J. Voss, et al. Effects of *d*-Band Shape on the Surface Reactivity of Transition-Metal Alloys. *Phys. Rev. B*, 89:115114, (2014).

[164] W. Hösler and W. Moritz. LEED Studies of Lead on Copper (100). *Surface Science*, 117(1):196 – 203, (1982).

[165] Y. Gauthier, W. Moritz, and W. Hösler. Surface Alloy in the c(4 × 4) Phase of Pb on Cu(100). *Surface Science*, 345(1):53 – 63, (1996).

[166] T. P. Moffat. Oxidative Chloride Adsorption and Lead Upd on Cu(100): Investigations into Surfactant-Assisted Epitaxial Growth. *The Journal of Physical Chemistry B*, 102(49):10020–10026, (1998).

[167] G. L. Kellogg and R. Plass. The Relationship Between the Growth Shape of Three-Dimensional Pb Islands on Cu(100) and the Domain Orientation of the Underlying c(52×2)R45 Structure. *Surface Science*, 465(3):L777 – L782, (2000).

[168] C. Nagl, E. Platzgummer, O. Haller, et al. Surface Alloying and Superstructures of Pb on Cu(100). *Surface Science*, 331-333:831 – 837, (1995).

[169] R. Plass and G. L. Kellogg. Surface Morphology Changes During Pb Deposition on Cu(100): Evidence for Surface Alloyed Cu(100)–c(2×2) Pb. *Surface Science*, 470(1):106 – 120, (2000).

[170] A. Taranovskyy, S. Guézo, H. Matsushima, et al. Studies of Electrochemical Surface Alloying and Dealloying by In Situ High-Speed STM. *Phys. Chem. Chem. Phys.*, 14:10579–10588, (2012).

[171] J. A. Bearden and A. F. Burr. Reevaluation of X-Ray Atomic Energy Levels. *Rev. Mod. Phys.*, 39:125–142, (1967).

[172] A. F. Wells. *Structural Inorganic Chemistry*, chapter 9. Oxford University Press, Oxford, fifth edition, (1984).

[173] Y. Soldo-Olivier, E. Sibert, M. De Santis, et al. Unraveling the Charge Distribution at the Metal-Electrolyte Interface Coupling in Situ Surface Resonant X-Ray Diffraction with Ab Initio Calculations. *ACS Catalysis*, 12(4):2375–2380, (2022).

[174] D. Porter. DanPorter/Py16, (2020). https://doi.org/10.5281/zenodo.3859719.

[175] Y. Gründer, C. A. Lucas, P. B. J. Thompson, et al. Charge Reorganization at the Adsorbate Covered Electrode Surface Probed through in Situ Resonant X-ray Diffraction Combined with Ab Initio Modeling. *The Journal of Physical Chemistry C*, 126(9):4612–4619, (2022).

Appendix A

Publications

Chapter 4 is based on, and a continuation of, the work published in following article, and the contributions of my fellow authors are gratefully acknowledged:

- Y. Gründer, G. S. Harlow, E. Cocklin, J. J. Fogg, J. W. Beane, C. A. Lucas. Potential-Dependent Surface Compression of Gold and its Link to Electrocatalytic Reactivity. *Surface Science*, 680:113-118, (2018). https://doi.org/10.1016/j.susc.2018.10.020

Chapter 5 is based on the following article, and the contributions of my fellow authors are gratefully acknowledged:

- Y. Gründer, J. W. Beane, A. Kolodziej, C. A. Lucas, P. Rodriguez. Potential Dependent Structure and Stability of Cu(111) in Neutral Phosphate Electrolyte. *Surfaces*, 2(1):145-158, (2019). https://doi.org/10.3390/surfaces2010012